Polyelectrolyte Multilayers Incorporating Photocrosslinking Polymers for Controlling 2- and 3-Dimensional Structure

by

Solar Candido Ademola Olugebefola

S.B. Materials Science and Engineering
Massachusetts Institute of Technology, 1999

Submitted to the Department of Materials Science and Engineering In Partial Fulfillment of the Requirements for the Degree of

Doctor of Philosophy in Materials Science and Engineering
at the
Massachusetts Institute of Technology

June 2007

Signature of Author: _____
Department of Materials Science and Engineering
May 24, 2007

Certified by: _____
Anne M. Mayes
Toyota Professor of Materials Science and Engineering
Thesis Supervisor

Certified by: _____
Michael F. Rubner
TDK Professor of Polymer Materials Science and Engineering
Thesis Supervisor

Accepted by: _____
Samuel M. Allen
POSCO Professor of Physical Metallurgy
Chair, Departmental Committee on Graduate Students

Polyelectrolyte Multilayers Incorporating Photocrosslinking Polymers for Controlling 2- and 3-Dimensional Structure

by

Solar Candido Ademola Olugebefola

Submitted to the Department of Materials Science and Engineering on May 24, 2007 in Partial Fulfillment of the Requirement for the Degree of Doctor of Philosophy in Materials Science and Engineering

Abstract

Polyelectrolyte multilayer (PEM) assembly is a technology for building thin films with a number of useful and novel functionalities. PEMs interact favorably with proteins and other biomolecules making them potentially valuable as biomaterials. Many systems of polymers have been studied for use in PEMs, including weak polyelectrolytes such as those containing poly(acrylic acid) (PAA) and poly(allyamine hydrochloride) (PAH), which exhibit pH-dependent behavior.

Properties such as thickness, swellability, mechanical stiffness, porosity (and by extention optical properties), and ability to adsorb small molecules are all controlled by the charge density of these polymers in the film and their resultant binding state. Patterning covalent binding through photo-crosslinking in addition to electrostatic binding, can locally override the native tendency to change structure with changes in pH. To achieve this, poly(acrylic acid) was chemically modified through a halide esterification reaction to incorporate photo-crosslinkable vinylbenzyl side groups, making poly(acrylic acid-ran-vinylbenzyl acrylate) (PAArVBA). The chemical modification was characterized by nuclear magnetic resonance spectroscopy (NMR) and light spectroscopy. NMR revealed that up to 6% of vinylbenzyl groups could be appended to PAA while maintaining the viability of the crosslinking group and the solubility of PAA in aqueous solution. Light spectroscopy indicated the location of the absorbance peak of the vinylbenzyl groups at 254 nm and the generation of crosslinking radicals was achieved with a quantum yield of 0.013. These parameters allow the polymer to be used in PEM films and to be crosslinked with a standard UV lamp, useful for practical applications.

The effects of crosslinking on film thickness, swelling in aqueous solution, and mechanical stiffness were measured with ellipsometry, atomic force microscopy (AFM) and nanoindentation. Crosslinking was observed to limit the degree of film swelling in neutral and basic solutions. The patterning of swelling through UV exposure with masking was achieved with a resolution demonstrated down to 3 μm feature sizes. The

mechanical stiffness of both crosslinked and as-built films was found to be less than that for equivalent films built with PAA, attributed to charge effects from the quarternary ammonium residue generated during the esterification reaction.

The ability of crosslinked PAH/PAArVBA films to locally suppress induced film porosity was confirmed with ellipsometry, AFM and optical microscopy. The suppression effect was used to build two types of films with patterned optical Bragg reflection through alternation of porous and nonporous stacks in the direction normal to the film plane. Maximum reflectivities higher than 70% were generated from 3.5 stack films due to the unusually low refractive index in the porous regions, modeled as 1.09.

Patterned structures, both porous and nonporous, were used to control the location of uptake of fluorescent dyes through increased affinity and surface area, as observed by fluorescence microscopy. Porous channel structures were used to direct dye uptake by controlling solvent transport through capillarity, enabling placement of two separate dyes in close proximity on a film surface without mixing. Finally, bovine serum albumin was used as a model protein to examine the effects of photocrosslinking and porosity on uptake and immobilization of proteins within PEM structures via fluorescence microscopy and radiolabeling. Porous thermally crosslinked films were found to adsorb significantly more protein than most other processing conditions and all films demonstrated retention of 80-95% of the adsorbed protein. Patterning of porosity gave selective control of the location of protein uptake.

Thesis Supervisor: Anne M. Mayes
Title: Toyota Professor of Materials Science and Engineering
Thesis Supervisor: Michael F. Rubner
Title: TDK Professor of Polymer Materials Science and Engineering

Table of Contents

List of Figures

List of Tables

Acknowledgements

I would like to first and foremost thank Professor Anne Mayes for her tireless and relentless dedication to not just scientific research, but research that has and will have a strong, positive effect the state of the environment and the health of our society. Professor Mayes has constantly led by example in her creativity, professionalism, and unwillingness to settle for anything but the truth. She is constantly finding new ways to make really small molecules do really big things. I would also like to thank her for her patience in letting me find my own way towards the completion of this work.

Professor Michael Rubner has been a constant resource for me in this work. I have spent large quantities of time in his lab, interacting with his students and bouncing ideas back and forth (and back). His expertise in the field of polyelectrolyte multilayers has been extremely valuable and necessary to understanding and capturing the potential of the system I work with. I am also grateful for his willingness to act as my advisor for the past half year in the face of unexpected circumstances.

I have worked with a great many people in my time as a graduate student and I am glad to have been in the presence of all of them. Everyone in the Mayes group has had something to teach me. Dr. Pallab Banerjee taught me enough synthesis to keep me out of trouble when I first arrived and more importantly, taught me proper lab conduct, which is vital for getting good results. Dr. Sang-Woog Ryu worked with me to develop the main synthesis scheme used in this work and his attention to detail was an inspiration. Elsa Olivetti, Juan Gonzalez, Ikuo Taniguchi, Ariya Akthakul, Ayse Asetekin, Ozge Halatci, Simon Mui, Pat Trapa and Nathan Lovell have always been around the office or the lab willing to lend a hand or head out to the Muddy. Will Kuhlman has been helpful to the extreme, willing to make radioactive proteins or help me haul a pump between labs (or do an exhaustive chemical inventory). His camaraderie and dedication to the support of his colleagues is admirable. I would also like to thank Jon Hester, Mike Fasolka, Darrell Irvine, Anne-Valerie Ruzette, Phil Soo, Stella Park, Metin Acar, Rafal Mickiewicz, Jane Park, Sebneb Inceoglu, Caitlin Devereaux, and You-Yeon Won.

In the Rubner group, I would especially like to thank Adam Nolte who has helped me with his expertise in optical structure modeling and his juggling skills. I would also like to thank Mike Berg for being always upbeat and willing to demonstrate various techniques, be it multilayer dipping or microcontact printing, and Zek Gemici asking me more questions than any two other people combined.

Professor Krystyn Van Vliet was kind enough to allow me into her lab and to teach me all about cell culture and nanoindentation. The welcome atmosphere of her group and the fruitful conversations we have had, resolving questions of data interpetation and experimental design have been invaluable. M. Todd Thompson has been a constant source of new techniques and interesting findings with regards to mechanical testing of thin films.

I would like to thank my UROP students Christina Laskowski, Tyson McNulty, Chenny Zhu and my RCC student Samson Hailemichael for keeping me on my toes.

Libby Shaw, and Tim McClure in the CMSE Instrumental Facility and Alan Schwartzman in the Nanomechanical Technology Laboratory have been good teachers when it comes to instrumentation. I have them to thank for much of my broad knowledge of characterization techniques.

This work also made use of facilities in the Institute for Soldier Nanotechnologies funded by the Army research Office and the Department of Chemistry Instrumentation Facility. This work was supported by the Dupont MIT Alliance, the Gates Millennium Scholarship Program, the Lemelson Foundation and by the MRSEC Program of the National Science Foundation under Award No. DMR-0213282.

Aside from research, there have been a number of people who have helped me keep my wits about me. Erik Blankenship realizes the important things in this world. Linus Park, Kevin Albert and Aryesh Mukherjee never met a 5.10c they didn't want to climb. Katie

Humphry and I have seen some really bad movies. Carla Heitzman shared my graduate school experience all of the way from Illinois. Jessica Howe is by far the person I know most likely to become famous. And Mathew Wong was my comic strip partner for three years.

Lastly I would like to thank my fiancée Kira for being the sunlight to my shadow, and for wanting a bouncy castle.

Chapter 1. Motivation and Background

1.1 The importance of interfaces in biomaterials

There is an ever present need for materials in the biomedical and bioengineering fields that exhibit useful behaviors when interacting with their environment. Many of the biomedical technologies that we employ today take advantage of the bulk properties of materials, a good example being arterial stents.

The basic operation of a stent is as such: When an artery becomes partially or fully blocked due to arteriosclerosis or other conditions, it is necessary to remove the blockage to prevent the death of surrounding tissue. The common procedure is to slide an uninflated balloon within the metal stent to the blockage site and expand the balloon, opening the artery, while simultaneously expanding the stent. The balloon is retrieved leaving the stent to prevent re-collapse. Functionally, the stent material's properties that are most important for good function are flexibility, both to allow the stent to fit through the artery and to enable its expansion and conformal fit; and strength, to keep the artery open against the pressure exerted by the arterial walls. However, one of the biggest problems with stents after implantation is restenosis or re-blocking of the artery caused by ingrowth of smooth muscle cells onto the device, akin to a scar covering an injury. The basic structural design of stents has not changed radically since its introduction, and the majority of current research is focused on preventing restenosis, mainly through the coating of stents with various drug-eluting films to inhibit cell growth. This coating is an example of the surface modification of a biomedical device in order to simultaneously exploit its bulk properties while mediating interaction with the body.

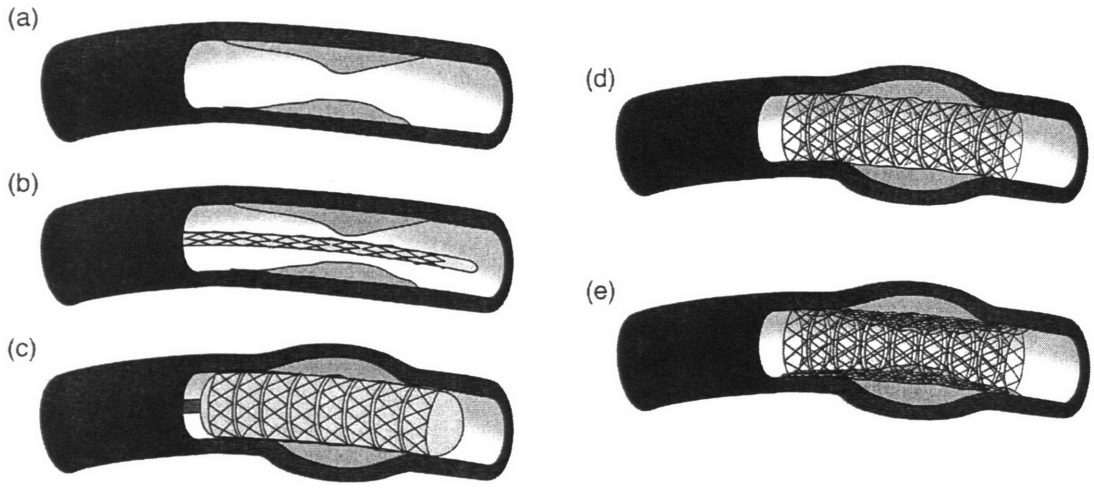

Figure 1.1. Schematic of stent function. (a) Blockage in a blood vessel caused by arthlerosclerosis. (b) Stent is inserted endoscopically around an inflatable balloon. (c) Balloon is inflated, pushing the blockage out of the way and opening the stant. (d) The stent remains in place preventing the vessel from closing. (d) Restenosis; smooth muscle cells migrate over the stent and cause a second blockage.

Surface interactions are a function of many materials properties working in concert. Physical interactions between materials, such as degree of adhesion, are controlled by physical properties such as surface roughness and stiffness, and chemical properties such as hydrophobicity/hydrophilicity and more explicitly the chemical reactivity of the surface. Surface modification for biological applications has been effected in a number of ways. One of the most common design strategies for controlling cell-surface interactions has been to create a bio-inert surface that prevents non-specific binding. Poly(ethylene oxide) brushes are the most employed polymeric material for creating inert surfaces, formed by grafting adsorption or by controlled surface segregation from bulk polymer mixtures [1-4]. Harder et al. linked it's the favorable properties of PEO to its helical structure which allows hydrogen bonding with water [5], and Szleifer and others have shown that with sufficiently high packing densities, PEO will form a

brush layer that resists protein adsorption due to the high energy required to displace the bound water [2, 6]. Other successful methods for preventing cell adhesion take advantage of similar material interactions with water to create "buffer" layers that reduce direct interactions between the material and undesirable biological molecules [7, 8].

Often a biological application for a material surface requires promoting growth of one class of organisms, such as eukaryotic cells, while preventing growth of another class, such as bacterial contaminants. Tissue regeneration also requires the ability to control the location and behavior of different types of cells, and this can be accomplished through the introduction of specific signaling elements, both as soluble chemicals and tethered ligands [9-11]. Polyelectrolyte multilayer assembly is a processing technique with the ability to present a bio-inert surface along with patterned signaling elements onto many substrates, and has thus emerged as a promising candidate for biomaterials engineering.

1.2 Polyelectrolyte multilayer assembly as a biomaterials platform

1.2.1 Assembly process

Polyelectrolyte multilayer (PEM) assembly is one of the most promising recent technologies for making thin surface films. Originated by Decher and coworkers [12-14], the process can create robust films and allows control over thickness and composition down to the molecular level.

The fundamental idea behind the technique is the sequential adsorption of oppositely charged species onto a charged substrate (Figure 1.2). Initially, a charged substrate is held in a solution containing dissolved species of net opposite charge (a1). In

appropriately designed systems, the species adsorbs to the surface to the extent that the newly created film then displays the net surface charge of the deposited species. After removal from solution and rinsing (a2), the sample can be placed into a solution containing the oppositely charged species (a3), whereupon adsorption occurs in the same manner as previously, yielding a new layer and another surface charge reversal. This process can be repeated many times to yield films of the desired thickness (b), quantized by the thickness of an individual layer or bilayer. Due to the method of layer addition, the film can be constructed on any surface topography that can be reached by the polymer molecules. Bruening, Schlenoff, Cohen and others have built onto membranes [15-17], capillary tubes [18], and joint prostheses [19] on the macro scale, and many types of organic and inorganic colloids on smaller length scales [20-29].

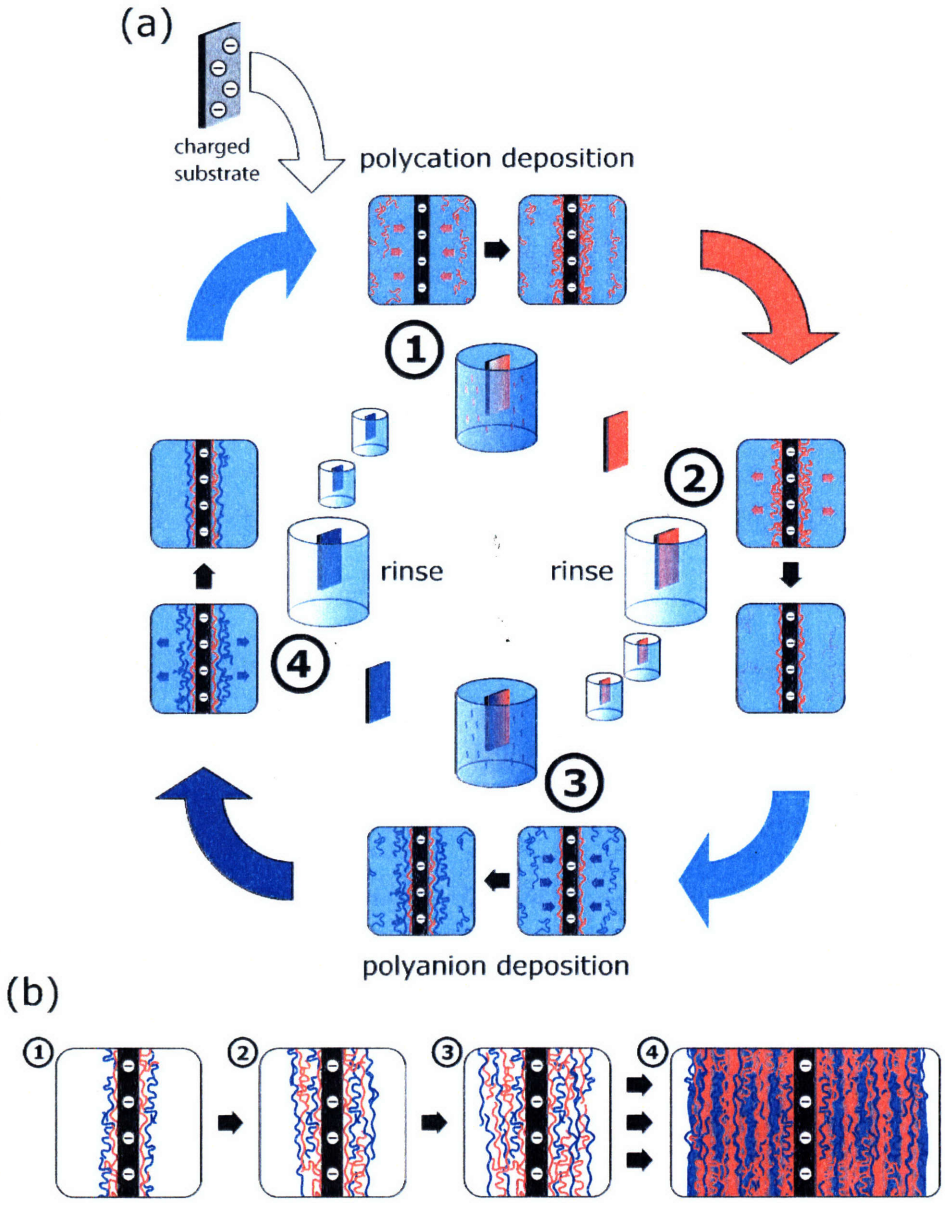

Figure 1.2. The polyelectrolyte assembly process. A negatively charged substrate is placed in a solution of polycation (a1) that adsorbs to the surface. The substrate is rinsed several times in water (a2) to remove loosely bound polymer, leaving only electrostatically bound material. The substrate is placed in a polayanion solution (a3) that causes adsorption similar to the first step. A second rinse removes loosely bound polyanion (a4) allowing the cycle to be continued. The process can be repeated as many times as necessary (b) to build films of the desired thickness.

Initial systems were constructed with of strongly-charged polyanions like poly(4-sodium styrene sulfonate) (SPS) paired either with strong or weak polycations such as

poly(diallyldimethyl ammonium chloride) (PDAC) and poly(allylamine hydrochloride) (PAH). These systems displayed expected linear film thickness growth as a function of number of deposition cycles [30, 31]. Korneev et al. used neutron scattering to reveal a structure that consisted of highly locally interpenetrated layers that nevertheless remained in their strata and did not move throughout the film [32]. This structure is common to many other polyelectrolyte multilayer systems.

Some systems, such as poly(*L*-lysine)/hyaluronic acid(PLL/HA) have demonstrated exponential film thickness growth per deposition cycle. Picart, Voegel and coworkers have used optical waveguide light spectroscopy (OWLS) and quartz crystal microbalance (QCM) measurements [33, 34] to show that the cause of this behavior is the ability of one of the polymers to diffuse through the film during assembly. This permits the polymer to concentrate at the film-solution interface and thereby increase the available surface charge for the next adsorption. Arys et al. discovered that other polymer systems such as those using ionenes demonstrate much more stratified films due to ordering upon adsorption and resistance to full complexation with their corresponding polyanion [35, 36]. Thus the type of polymer and the interactions between the polymer pairs used for assembly have a great deal of influence on the behavior during assembly and the final film structure.

1.2.2 Functional polymers in Polyelectrolyte multilayers

Essentially, the only major restriction for PEM assembly is the need for surface-available charged groups on the components. The broader layer-by-layer assembly process even extends to other types of binding. Rubner, Sukhishvili, Hammond and

others have looked at hydrogen-bonding [37-45] systems. Caruso, Rubner, Cohen and others have examined metal-polymer electrostatic interactions [46-48].

Many polymers with different functionalities have been studied to enable the fabrication of films with different physical and chemical properties. Sukhorukov, Schlenoff and coworkers have used temperature sensitive polymers to control film permeability for drug release [49-51]. Electroluminescent polymers and small molecules have been used for constructing light emitting films [46, 52]. Urban and others have incorporated heparin into films that maintain its anti-coagulant function [53-55] and proteins with enzymatic function have been shown to maintain activity within their respective films [26, 56, 57]. Inorganic materials such as semiconductor nanoparticles have been incorporated to create photoluminescent PEMs [27].

The most basic and important functionality is the charged nature of the polymers for assembly and this can be manipulated to achieve foremost, control over the film structure. This is often accomplished through modification of the charge interactions between the assembly components, both during assembly and in the final state. Controlling the ionic strength of the deposition solutions is one method of accomplishing this. Charge screening caused by the presence of small ions during assembly has been shown to affect film thickness [30, 58-60], and surface roughness [61]. Post-assembly, film exposure to high ionic strength environments has also affected film properties, such as porosity [62] and hydrated film thickness [61, 63]. The stability of the films is also strongly affected by the ionic environment. Several groups have shown that at sufficient salt concentrations, all polyelectrolyte multilayer films will eventually partially or

completely dissolve [60, 64] unless some form of binding mechanism other than electrostatics is used.

Another method for controlling available charge is by using weak polyelectrolyte components that demonstrate pH-dependent charge density. By controlling the pH of the polymer solutions during PEM assembly, the adsorption behavior of the polymer and in turn, the final structure of the film, is modified. Poly(acrylic acid) (PAA) and poly(allylamine hydrochloride) (PAH) are two of the most widely used weak synthetic polyelectrolytes in studies pertaining to this field [46, 48, 65-74], although others have also received attention, such as poly(ethylene imine) (PEI) [75, 76].

1.2.3 Multilayer films containing poly(allylamine hydrochloride) and poly(acrylic acid)

The variable charge density on PAA comes from the phenomenon that at low pH, the carboxylic acid groups on the chain become protonated, creating neutral carboxylate groups. Correspondingly, positively charged amine side groups of PAH become de-protonated at high pH. Detailed studies of thickness of PAA/PAH films as a function of assembly pH for both polymers show in some cases non-intuitive morphology [68]. For example, in pH-symmetric systems (where both polymer deposition solutions are at the same pH) beginning from acidic conditions, the thickness of each of the layers follows expected trends whereby the PAA layers decrease in thickness due to the increasing charge, while the PAH layers do the opposite. This behavior abruptly changes after pH 4.5, where both polymer layer thicknesses increase significantly, and changes again after pH 5.5, where layers shrink to what is essentially the thickness of the flattened polymer chains [68]. This behavior has been ascribed to the tradeoff between the greater entropy

but higher segment-segment repulsions of the extended brush-like chains and the lower entropy but also lower interfacial free energy per chain of the flattened chains bonded electrostatically at many discrete sites along the polymer backbone [69, 70]. Using increasingly basic pH during assembly has similar effects on the morphology of these films, as PAH becomes more weakly charged. Above pH 8, films show an abrupt increase in assembled thickness, mirroring the trend with lower pH, until the solubility limit of PAH is reached at pH above 9 [68].

The pH-influenced nature of PAH/PAA PEMs has led to a number of interesting film properties and corresponding applications. The first is simply the variable degree of swelling in aqueous solution. When assembled at acidic pH, many of the side groups in PAA do not take part in the assembly process due to their protonation and so they remain unpaired with a corresponding amine group. When appropriately immersed in neutral or basic solution, these free carboxylate groups once again become carboxylic acids and give the film a net charge, allowing it to attract small counter ions and water molecules to cause film swelling. This effect is strongly related to, and easily controlled by, the assembly solutions' pH, giving differences in swelling. For example, from slightly greater than 100% to close to 400% for PAH/PAA films assembled at pH 6.5 and 2.0 respectively [77]. One of the major differences in these films besides thickness is their stiffness, which will be discussed later.

In order to codify the notation for pH-sensitive PEMs, films will be referred to by their components in the manner $(PX\ pH1/PY\ pH2)_z$, where *PX* and *PY* denote the polycation and polyanion used, *pH1*, *pH2* denote the pHs of the polymer dipping solutions and z refers to the number of bilayers deposited. For example, (PAH 8.5/PAA

$3.5)_{10.5}$ would refer to a multilayer containing a PAH layer deposited from pH 8.5 solution followed by a PAA layer deposited from pH 3.5 solution. This bilayer process would have been repeated 10 times. The "0.5" in the bilayer number refers to the fact that the film ends with a top surface of PAH deposited at pH 8.5, thus an additional half bilayer.

The similar way in which PAA and PAH behave in PEM assembly as their charge densities decrease suggests that pH-asymmetric films with PAA built at low pH and PAH built at high pH would possess very different structures from those with only one of the polymer pairs partially charged. Studies by Mendelsohn et al. of (PAH 7.5/PAA 3.5) films have shown them to respond very dramatically under the appropriate conditions. When assembled films are subjected to pH $\leq$ 2.5 followed by neutral pH they spontaneously transition from uniform films to microporous ones [67]. This critical pH is where a large percentage of the carboxylic acid groups on the PAA chains abruptly become protonated, breaking enough electrostatic bonds with PAH to allow the film to massively reorganize, resulting in spinodal decomposition of the polymers from the water medium. It is only made possible because of the selected pH conditions during assembly.

Further studies of pH-asymmetric PAH/PAA films have extended the scale of porosity achievable through controlling processing conditions. Along with the micro-porosity of (PAH 7.5/PAA 3.5) films, Hiller and coworkers have observed nano-porosity in (PAH 8.5/PAA 3.5) films when subjected to acidic pH followed by neutral or close to neutral pH [78]. This mechanism of transformation is believed to be the same as that for the (PAH 7.5/PAA 3.5) system and has been exploited to make films that display both tunable Bragg reflectivity [79] and controlled drug release [80].

1.2.4 Cell interactions with multilayers

Biological interactions with many different PEM systems have been studied both *in vivo* and *in vitro*. While in vivo research is still in the early stages, implanted devices such as stents [81] and tracheal prostheses [82] have demonstrated increased thromboresistance and anti-inflammatory behavior with PEM encapsulation and the addition of appropriate chemical factors. *In vitro* cell interaction with PEM films has been a growing area of research. Biomolecules such as polysaccharides and peptides have been used as components in PEMs in order to promote and prevent the clotting response of human blood [83], as well as for creating bio-inert and cell adhesive surfaces [84]. Picart and coworkers have used poly amino acids such as poly(L-glutamic acid) and poly(L-lysine) to control phenotype expression in film-adhered osteoblasts [85]. Purely synthetic systems include hydrogen-bonded layer-by-layer polyacrylamide (PAAm)/PAA multilayers that show cytophobicity but not cytotoxicity [41].

An emerging understanding of cell interactions with surfaces places substrate mechanical stiffness among the major factors in controlling behavior in anchorage-dependent cells. Cell properties such as phenotype [86], cell motility [87], migration direction [88], and cell adhesion and spreading [89] can be affected by the compliance of the underlying substrate, independent of, or in addition to, chemical signals.

Mendelsohn et al. have demonstrated this compliance effect with PAH/PAA multilayers through differing fibroblast adhesion behaviors to films constructed at different pH [77]. More specifically, films with a high degree of swelling, assembled at low pH, resisted cell adhesion, while films with lesser swelling promoted cell adhesion. This occurred independent of several other film properties, such as wettability, degree of

protein adsorption or surface charge [77]. Thompson et al. used nanoindentation measurements of stiffness in these films to confirm the inverse correlation between degree of swelling and modulus [90]. As well, the mechanical effects of ligand attachment have been shown to affect cell behavior [90] separately from chemical interactions. Picart and coworkers have shown that the system hyaluronic acid/poly(L-lysine) in particular demonstrates tunable cytophobicity/cytophilicity depending on degree of crosslinking (which affects mechanical compliance) and film thickness [91, 92].

1.2.5 Patterning and higher-level order in PEMs

Micro-contact printing, a technique first developed by Whitesides and coworkers [93], is the most well-documented approach to laterally patterning multilayer films. A stamp, usually made from crosslinked polydimethyl siloxane (silicone rubber), is covered with polymer or small molecules and pressed onto a surface. The molecule is deposited only where the stamp makes contact with the surface. This process has been used to pattern multilayer deposition on many different types of surfaces by depositing a charged polymer selectively onto a surface, only enabling assembly over those regions [94]. Hammond and coworkers have adapted the technique to deposit polyelectrolyte of opposite charge onto already assembled multilayers. Known as polymer-on-polymer stamping (POPS) [94, 95], this method is used to enable further assembly or reactivity only in those areas,. Microcontact printing can also be used to guide deposition of other components onto multilayers. Through control of charge, patterned deposition of polymer colloids and magnetic particles [96-98] have been demonstrated. POPS of biomolecules has been used for directed cell adhesion [99-101] and even multilayer films

previously assembled on patterned stamps have been wholly transferred using this technique [102, 103].

Other techniques have also been used to laterally pattern multilayer films. Lvov and others have used deposition on a substrate with polymer solutions guided by microfluidic channels [104, 105]. Wang et al. and Lu et al. have used patterned contact compression of assembled films [106, 107]. Mirkin and coworkers utilized dip-pen lithography to deposit charged molecules onto a surface with a nano-scale chemically wetted tip to promote polymer deposition [108]. The deposition of multilayers on lithographically patterned photoresist on silicon, followed by etching of the photoresist has been reported by Caruso and coworkers [109]. Lithography on multilayers with specialized photoactive components has also been employed for patterning, either by rendering the exposed regions of the multilayer more soluble as demonstrated by Rubner and coworkers [38, 41], or more often by creating covalent crosslinks to enhance stability, as will be discussed below.

1.2.6 Crosslinking in polyelectrolyte multilayers

There are several methods for crosslinking PEM films, each with advantages and disadvantages. For systems containing free amines and carboxylic acids, Bruening and coworkers have extensively studied amide crosslinks created with heating [110, 111]. This process has been used to make ion-separating thin film nylon membranes [15, 16], and to enhance film stability in various non-aqueous solvents [17, 112]. It has also been used to preserve metastable microstructures such as nano- and micropores [79, 80]. The disadvantage of this process is the need for temperatures close to 180 °C, which can damage any thermally sensitive film components such as proteins. Alternatively, low

temperature amide bonds can be formed using a crosslinking catalyst such as N-ethyl-N'-(3-dimethylaminopropyl) carbodiimide (EDC) [21, 84, 91, 113-118]. PEM capsules have been stabilized against dissolution with this process [21, 42] as well as planar films [91, 115]. Varying the quantity of catalyst controls the degree of crosslinking and this can lead to control over mechanical properties such as film modulus [91]. Both of these crosslinking methods rely on the presence of amines and carboxylic acid groups. As well, any components with free amines such as proteins or peptides will be covalently bound to the structure, which is not always desirable. Lastly, these techniques are not feasible for nano- and microscale patterning, since controlling the spatial application of thermal energy and/or small molecule diffusion in films on these scales is very difficult.

Photochemical crosslinking has been demonstrated as a route to patterning multilayers following several approaches. Cao and coworkers pioneered the use of diazo-resins (DARs), which are cationic and can covalently bind with sulfonate and carboxylic acid groups [119, 120]. Multilayers built from these polymers have demonstrated pattern-selective film etching [121], which has been used to guide colloid adsorption and create freestanding films [122]. While DARs are strongly charged, pairing with weak polyanions gives some of the pH-dependent behavior observed for fully weak systems, such as pH-dependent assembly thickness [123]. However, DARs have poor stability at high pH [124], which would make it difficult to build films using high pH conditions, necessary to achieve certain pH-induced behaviors, such as micro- and nano-porosity.

An alternative method for photo-crosslinking was developed by Advincula and coworkers, through the covalent binding of photoactive benzophenone to PAA and PAH

[125]. This method has the potential to address many of the problems associated with other crosslinking techniques, including the ability to take advantage of pH-sensitive behaviors of weak polyelectrolytes. Multilayers made from PAH-benzophenone and SPS have been used to make hollow capsules for small molecule loading and release [126].

1.2.7 Protein and small molecule interactions with multilayers

One of the most active areas of investigation for PEMs is that of controlling therapeutic drug interactions. Drug release mechanisms applicable to PEMs can be separated into three types. Matrix-type and dissolution-type both begin with the drug distributed within the film. The difference is that in matrix-type, the drug escapes by diffusion from the film into solution while release in dissolution-type occurs by the degradation of the polymer matrix, exposing the drug to solution. The third type, reservoir-type, is a delivery approach in which the polymer acts as a diffusion barrier (or membrane) for a separate large reservoir with a much higher diffusivity, thus controlling the release rate. For matrix-type systems, simple uptake into assembled multilayer films has been examined [71, 127, 128] as well as using the theraputic agent as a component in the assembly, such as with DNA [14, 75, 129, 130]. Recently, Hammond and coworkers have demonstrated pseudo-first order release from dissolution-type, hydrolytically degradable multilayer films made from amino esters and polysaccharides [131], but examples of this behavior in the field are rare.

Lvov, Caruso, Voegel, and others pioneered much of the initial investigation of multilayer systems with proteins as components and studied the effects of incorporation on structure [132-134], biological activity [135, 136], mobility [137, 138], and stability [139]. The consensus findings are that for most systems, incorporated proteins maintain

their solution state structure and function and can even demonstrate improved stability to temperature and pH changes. As these systems demonstrate usefulness for biological applications such as influencing cell behavior, patterning capability can further broaden the utility of PEMs in chemical and biological sensing, and diagnostics.

1.3 Thesis Scope and Goals

The basis of this thesis is the control of the morphology of polyelectrolyte multilayer films for various applications utilizing photoactive components. The nature of the layer-by-layer technique allows for programmed film heterogeneity in the growth direction through the choice of material incorporated into each layer. Through the layer-selective incorporation of photoactive polyelectrolytes, and the use of photolithography, control over structure in the plane normal to the film growth direction can be achieved, leading to the ability to dictate the properties of the film in three-dimensions.

Chapter 2 of this thesis is concerned with synthesis of a polymer that can be incorporated easily into the PEM assembly process, yet can enable localized patterning of the final film structure. This is in contrast to a small molecule used for crosslinking such as EDC [91, 116], that will travel throughout the assembled film. The reactivity of poly(acrylic acid) side groups gives the opportunity to attach vinylbenzyl iodide, a photoactive molecule, to this common PEM component, in quantities small enough to maintain a high overall charge density, yet large enough to substantially modify the physical properties of the final film. The photoactivity and solubility of the resulting polymer poly(acrylic acid-*ran*-vinylbenzyl acrylate) (PAArVBA) as well as the efficacy of the coupling reaction will be quantified.

In Chapter 3, the properties of films made from the modified polymer will be compared to those assembled with unmodified PAA, including film thickness, hydrophilicity, and stability under various aqueous environments. The effects of photo-crosslinking on the structure of assembled films will be observed, specifically the mechanical properties and swelling characteristics of films in aqueous solution.

The internal structure of PAH/PAA pH-asymmetric films (PAH 7.5/PAA 3.5, PAH 8.5/PAA 3.5) can be modified by exposure to acidic and neutral aqueous solution, but this can only occur because of the ability to break and reform electrostatic bonds between polymer chains. By the insertion of PAArVBA containing photo-crosslinking groups we can locally inhibit the reformation process in the layer plane because of the higher stability of the resultant covalent bonds. In Chapter 4 we will examine the effects of this covalent binding on the porosity transition observe the effects of two-dimensional patterning on porosity.

The inherent control in layer-by-layer assembly over polymer composition also enables control over porosity in the growth direction, through the insertion of PAArVBA, and/or components such as strong polyelectrolytes without pH-dependent behavior. This gives a degree of 3-dimensional control over the location of porosity within multilayer films. In Chapter 5 this will be demonstrated through the patterning of porosity in heterostructured polyelectrolyte multilayers (HPEMs) containing alternating stacks of pH-insensitive PAH/SPS and PAH/PAArVBA. Similar to previous work [79], this structure should lead to the ability to make Bragg-reflectors by inducing nanoporosity only in the pH-sensitive stacks, but with the addition of lateral patterning functionality obtained through the photocrosslinking inhibition of the porosity transition. The new

properties of PAArVBA also enable the construction of a new Bragg structure with the assembly of alternating PAH/PAA and PAH/PAArVBA stacks enabling patterning of regions of alternating porous polymer stacks side by side with fully porous regions. The reflectivity of these films is dependent on the stack thicknesses, the number of stacks and the refractive index difference between the alternating stacks.

Loading and release of biologically active molecules from PEM films is a complex process due to a number of factors. The molecule size, charge and hydrophilicity all determine what PEM system will be ideal for its binding or entrapping. Also, the incorporation method is important. Simple adsorption of the active molecule is the most straightforward method, but achieving a release profile that is significantly different from the adsorption profile requires either a strong interaction between the polymers in the film and the target molecule, or some way to alter the structure post-adsorption. The increased surface area presented by porous multilayers may enable enhanced adsorption of guest molecules. Chapter Chapter 6 will examine the loading of model dyes into as-built, crosslinked and porous (PAH 8.5/PAArVBA 3.5) multilayer films and the effects of charge and hydrophilicity on binding. Patterning of the porous structure will be used to demonstrate selective binding as well as the creation of capillary channels able to independently load different molecules onto the same film. In addition, albumin will be used as a model protein to assess the ability of these films to load larger molecules and their capability for release

Overall, this thesis will demonstrate the enhanced control that photocrosslinking brings to the already versatile technique of polylelectrolyte multilayer assembly. This should lead to new applications that take advantage of the many structures achievable in

weak PEMs, especially their sensitivity to local environments and their compatibility with biological and bioengineering systems.

Chapter 2. Synthesis and characterization of poly(acrylic acid-*ran*-vinylbenzyl acrylate)

The introduction of photo-crosslinking functionality into polyelectrolyte multilayer assembly is not new, but commonly the purpose of such endeavors has been to exploit the difference in robustness between the covalently and the electrostatically crosslinked regions of assembled films, enabling such applications as microcapsules that are stable in destructive environments [25, 126] or selectively etched films [122]. While we also wish to exploit this difference, we are as much concerned with the ability of the photo-crosslinking to control other aspects of film structure, especially for multilayer films containing weak polyelectrolytes. In order to explore this structural control, we require a polymer that is a weak polyelectrolyte with photo-crosslinking groups sufficient to preserve film morphology. Another of our aims is to use assembled films to house biological molecules, and as such a crosslinking mechanism that avoids direct interaction with the carboxylic acid groups and primary amines abundant on peptides and polypeptides is desired.

A straightforward method for photo-crosslinking is to use a polymer with unsaturated double bonds. Exposure of these groups to ultraviolet light in a film should promote the generation of tethered radicals that can readily attack other double bonds present, creating dimers to link chains. In addition, the localization of the double bonds to the polymer chains should prevent, or at least restrict, the migration of radicals from the intended pattern region, in contrast with small molecule crosslinking agents that would be expected to diffuse throughout the film, e.g. EDC [91]. To that end, we have developed a method to utilize the chemical activity of poly(acrylic acid) towards

appending groups with this crosslinking functionality. The chemical vinylbenzyl iodide serves as a good candidate for fulfilling our requirements. If reacted with PAA in a halide esterification reaction [140] in small quantities, the charge behavior of the polymer should be preserved while adding control over structural transformations.

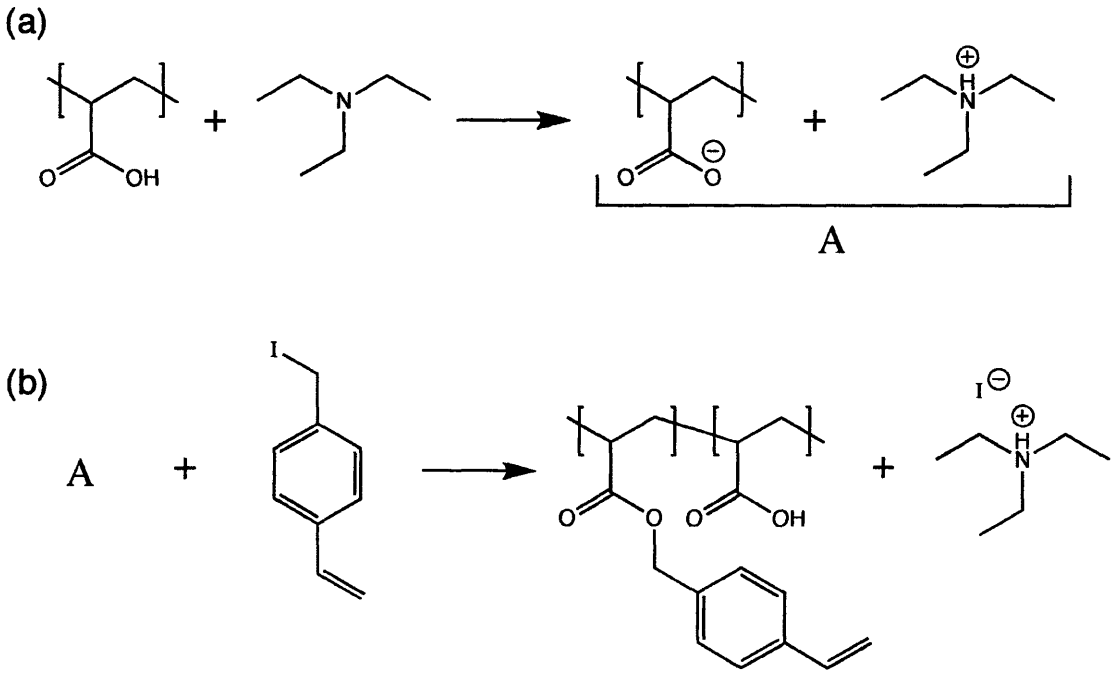

Scheme 2.1. The synthesis of poly(acrylic acid-*ran*-vinylbenzyl acrylate) (PAArVBA). (a) Poly(acrylic acid) is charged by the presence of trithethylamine. (b) The vinylbenzyl iodide couples to poly(acrylic acid) as long as the iodine can make a quarternary amine with the triethylamine, thus replacing some of the acrylic acid side groups with vinylbenzyl acrylate groups.

2.1 Materials

Vinylbenzyl chloride, sodium iodide, poly(allylamine hydrochloride) 70,000 g/mol (PAH), triethylamine (TEA), potassium iodate, poly(sodium-4-styrene sulfonate) (SPS) 1,8-diazobicyclo[5.4.0]undec-7-ene (Sigma-Aldrich), potassium iodide (Mallinckrodt), poly(acrylic acid) 90,000 g/mol (PAA), 25 wt% aqueous solution

(Polysciences), and sodium tetraborate decahydrate (Fluka) were used as received. All aqueous solutions were prepared using Milli-Q Academic (Millipore) water with a total organic content (TOC) of <15 ppb. Aqueous solution pH values were measured using either a Beckman Coultier Φ360, or a Thermo Electron Orion 230A pH meter with buffered calibration standards (VWR Scientific).

2.2 Synthesis of vinylbenzyl iodide precursor

To create the PAArVBA co-polymer, it is first necessary to synthesize the precursor that couples to the PAA acid groups, vinylbenzyl iodide. Sodium iodide (98.5 g, 657 mmol) and 500 mL acetone were added to a flask and stirred until the salt was completely dissolved. Vinylbenzyl chloride (21.48 g, 141 mmol) was added and the solution refluxed at 54 °C under nitrogen for three days. The solution was then filtered to remove precipitated sodium chloride and roto-evaporated until nearly dry. The recovered product was re-dissolved in 60 mL of acetone and the resulting solution precipitated in 1 L hexane. The liquid portion was roto-evaporated to precipitate additional salt, decanted and filtered in hexane through a silica column. The filtered liquid was roto-evaporated to remove the remaining hexane, leaving the vinylbenzyl iodide (VBI) product. ^{1}H NMR spectra of vinylbenzyl chloride and vinylbenzyl iodide samples dissolved in deuterated chloroform were measured on a Bruker Avance-400 NMR spectrometer (Figure 2.1). Upon completion of the reaction, the vinylbenzyl chloride peak at 4.6 ppm, attributed to the chloromethyl groups, was observed to shift to 4.5 ppm, corresponding to iodomethyl protons.

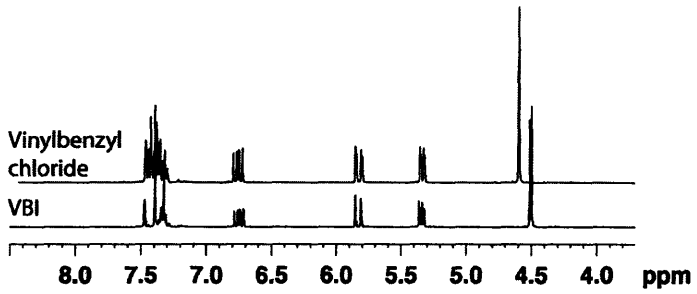

Figure 2.1. NMR spectra of vinylbenzyl chloride and the more reactive vinylbenzyl iodide in deuterated chloroform ($CDCl_3$). The halide exchange is confirmed by the shift of the peak for the protons nearest the halide from 4.6 ppm to 4.5 ppm.

2.3 Coupling of vinylbenzyl iodide to poly(acrylic acid)

2.3.1 Scheme 1

PAA (2.5 g) was dried from solution under vacuum overnight and added to a flask containing 300 mL dimethylformamide (DMF). The solution was purged with nitrogen and heated to 90 °C under stirring until the PAA dissolved. After lowering the temperature to 30 °C, 2.6 mL triethylamine (TEA, excess) was added along with 2.2 mL VBI (excess) and the mixture was stirred overnight. Progress of the reaction was indicated by the solution changing color from clear to bright yellow. The mixture was precipitated in 1.2 L tetrahydrofuran (THF) producing a pale yellow solid. The recovered product was dissolved in 200 mL water, filtered to remove insoluble particulates of polymer with too high of a VBA:AA ratio, then dialyzed using 3500 MWCO Snakeskin dialysis tubing (Pierce) in 2 L of water exchanged once a day for three days. Subsequent poly(acrylic acid-*ran*-vinylbenzyl acrylate) (PAArVBA) formulations were made from diluted portions of this solution. The concentration was determined by weighing the vacuum dried product from a 1 mL initial volume sample. Coupling was verified with ^1H

NMR in deuterated water, by observing the shift from 4.4 ppm (a5) to 5.0 ppm (b5'), and broadening of the peak for the hydrogen pair adjacent to the iodide group (Figure 2.2). Some formulations were recovered from the solid form, placed into a vacuum oven for at least 24 hours and used subsequently without dialysis. ^{1}H NMR was also used to verify coupling in this case. Evident in Figure 2.2 are additional peaks at (6) 3.05 ppm, (9) 1.25 ppm, and (9) 1.12 ppm. These match the NMR signature of TEA. While the majority of THF and DMF can be removed through the precipitation, vacuum drying and dialysis processes, triethylamine persists. The peak at 3.2 ppm corresponds to the protons bound to the carbons nearest the nitrogen center but the two peaks at 1.2 and 1.3 ppm are believed to belong to the same chemical group, that of the protons in the three terminal methyl groups as suggested by the 3:2 peak area ratio between the sum of those two peaks and the first peak. The reason for the peak separation is possibly the two different chemical environments that these protons experience, namely the charged and neutral states of the central nitrogen. It is understandable that the charged TEA molecule would electrostatically bind to free carboxylic acid groups along the polymer chain, making it hard to remove. Less clear is the binding of the neutral TEA to PAArVBA. It may be due to hydrogen bonding effects, or hydrophobic association with the coupled vinylbenzyl groups.

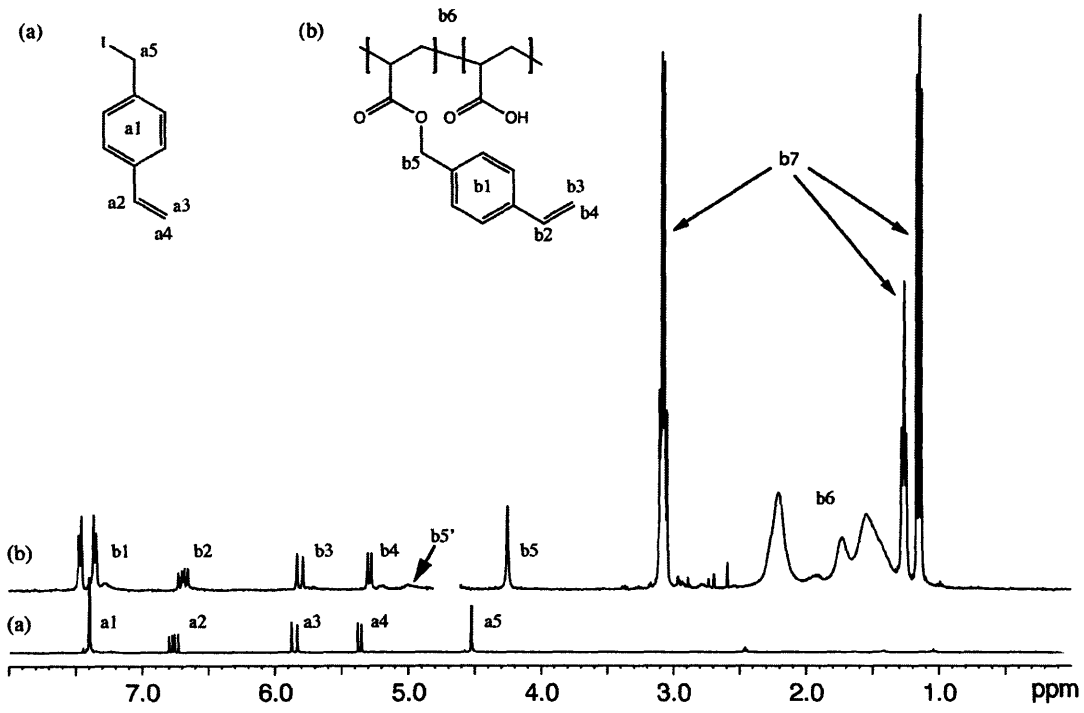

Figure 2.2. NMR of vinylbenzyl iodide in $CDCl_3$ (a) and PAArVBA in D_2O. The iodomethyl proton peak shift for vinylbenzyl iodide (4.5 ppm at a5 to 5.0 ppm at b5') and the accompanying broadening of the peak indicate coupling to the polymer. The (b7) peaks correspond to triethylamine (TEA). D_2O peak removed from (b) for clarity.

The presence of triethylamine in the polymer solution especially in the charged state will have an effect on the assembly behavior and the final film structure in the same manner that any additional ions in solution would. However, it should not affect the ability of the polymer to create covalent bonds when exposed to UV irradiation.

2.3.2 Modifications to Scheme 1 to improve purity

In the latter stages of this research, a new protocol was developed for coupling which results in higher purity material and more consistent polymer solubility in water after drying. Triethylamine was replaced with 1,8-diazobicyclo[5.4.0]undec-7-ene (DBU), a stronger tertiary amine that enables greater reactivity of the esterification

reaction [15]. With this new modification, it was no longer necessary to pre-dry the polymer, making dissolution in DMF simpler. In addition, dialysis was more successful at removing the amine post-coupling.

PAA 25 wt% in aqueous solution (10 g) was added to a flask containing 100mL dimethyl formamide and stirred until dissolved. DBU (0.5 g) was added and allowed to dissolve before adding 0.5g VBI. The flask was then sealed and purged with nitrogen for 5 min and allowed to stir overnight at room temperature. The solution was then precipitated in 1.2 L THF, producing fine particulates. The precipitate was allowed to settle/aggregate and the remaining liquid was decanted. The product obtained at this point was a pale yellow viscous fluid. The polymer was allowed to dry until semi-solid and then small amounts of sample were taken for NMR measurements and the remainder was dissolved into 50 mL Milli-Q water. NMR samples were dissolved in deuterated DMSO ($DMSO_{d6}$) in order to compare peak locations exactly with VBI, which is also soluble in DMSO. Shown in Figure 2.3 are the spectra of VBI and of DBU-catalyzed PAArVBA taken from the sample produced before dialysis.

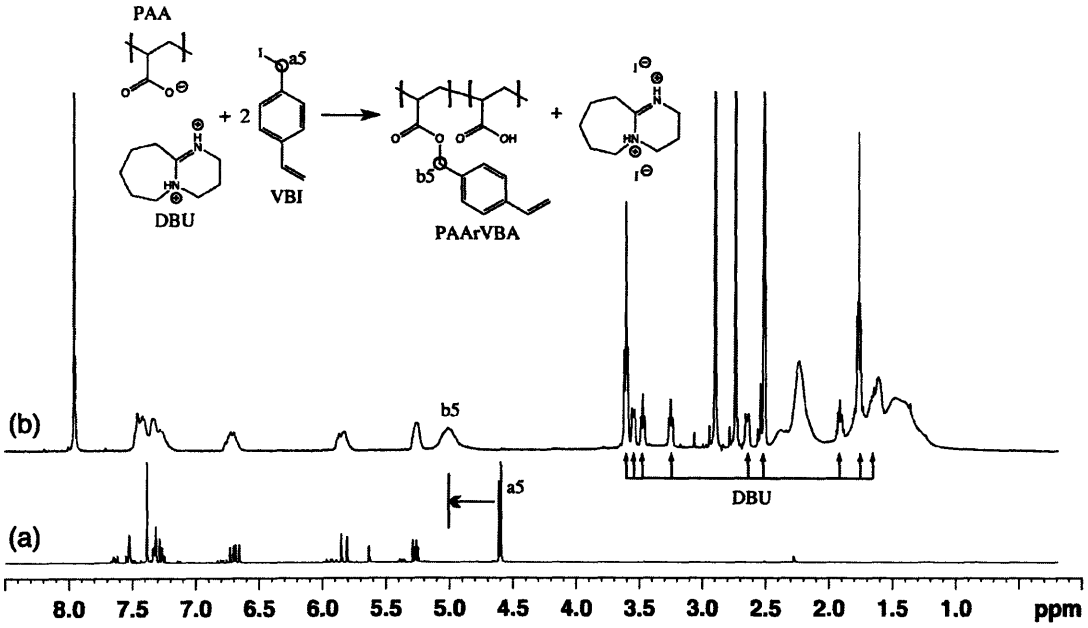

Figure 2.3. NMR of VBI (a) and PAArVBA (b) in $DMSO_{d6}$. The broadening of all side group peaks after synthesis is apparent. 1,8-diazabicyclo[5.4.0]undec-7-ene and dimethyl formamide peaks show up in the lower end of the spectrum of PAArVBA before purification.

The large peak shift for the iodomethyl protons (a5 to b5) is apparent, as is the lack of residual VBI, since it is all consumed in the reaction. There is also residual DMF (2.7, 2.8, 8.0 ppm) and DBU (labeled in Figure 2.3). To purify the samples, the polymer water solution was dialyzed following the same procedure as the previous section, except in a solution of pH 3.5, below the pKa of PAA in solution, which should allow the charged amine to decouple from the acrylic acid side groups. Shown in Figure 2.4 is the NMR of samples taken at three time points for the dialysis. The large peak at 3.4 ppm is residual water from drying the sample, but the peaks from DBU can be seen superimposing upon them. After three days of dialysis, the contaminants are mostly removed. The small peak at 2.5 ppm is from $DMSO_{d6}$.

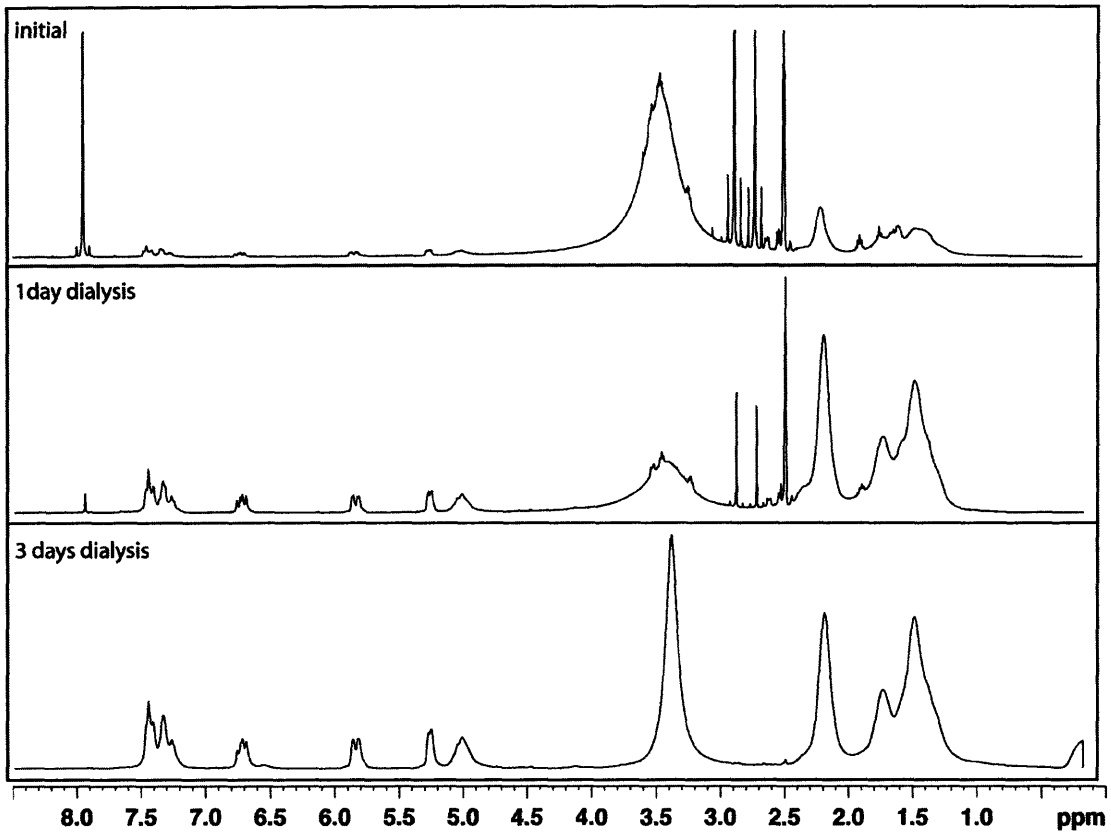

Figure 2.4. NMR of PAArVBA purification in $DMSO_{d6}$. The peaks attributed to DMF (2.6, 2.8, 8.0 ppm) and DBU (as noted in **Figure 2.4**) disappear from the spectrum after 3 days of dialysis in aqueous solution at pH 3.5.

In all following sections, where this polymer synthesis was employed, it will be denoted as DBU-catalyzed PAArVBA (DPAArVBA) and the previous synthesis product will be referred to as TEA-catalyzed PAArVBA (TPAArVBA).

2.4 Characterization of poly(acrylic acid-ran-vinylbenzyl acrylate) in solution

2.4.1 Calculating ratio of acrylic acid to vinylbenzyl side groups in PAArVBA

In order to control the nature of structural changes in multilayer films containing PAArVBA, it is necessary to characterize the behavior of the polymer when exposed to activating radiation. Firstly, the available amount of crosslinking groups must be determined. From NMR measurements we can estimate the percentage of pendant vinylbenzyl acrylate groups in the copolymer (Figure 2.2). The most direct comparison can be made between the (b5') peak at 5.0 ppm, attributed to the proton pair between the ester oxygen and phenyl group, and the peak at 2.17 ppm, attributed to the single proton of the first carbon on the polymer main chain. From various syntheses, this value has been calculated as between 3.1% and 6.0%. Of note is that this is not necessarily the percentage for all polymer created in this coupling reaction, but rather the polymer that is hydrophilic enough to precipitate in tetrahydrofuran and dissolve in water. It may be possible to isolate polymer with a larger vinylbenzyl side group percentage, but multilayer deposition would have to be carried out at least partially in non-aqueous or semi-aqueous solution. Typical initial yields for TPAArVBA were ~60%. Typical yields for DPAArVBA were 90% or higher.

2.4.2 Quantifying UV reactivity of PAArVBA

UV-vis spectroscopy measurements were made on a Cary 5E Spectrophotometer (Varian). Aqueous solution measurements were made using a quartz cuvette with a path

length of 10mm. Solutions were crosslinked by exposure to a Model UVG-11 short wave ultraviolet lamp transmitting at 254 nm and 4 W from a distance of 3 cm.

In order to determine the reactivity of the PAArVBA to UV light, it is necessary to establish several parameters. The amount of light impinging on the sample must be quantified, as well as several parameters relating to the interaction of the polymer with light. The first is the molar absorptivity, which is used to relate the amount of adsorbed light in a solution to the concentration of molecules in that solution. The second is the quantum yield, which relates the amount of adsorbed light to the number of reactions that take place.

For most solutions, where the solute is of low enough concentration, the ratio of incident light to adsorbed light is related to the concentration in a prescribed fashion. The Beer-Lambert law describes this relationship as

$$-\log\frac{I}{I_0} = A = \alpha l c \qquad (2.1)$$

where I_0 and I are the intensities of the incident light on and transmitted light through the sample, respectively, A is the absorbance, l is the length of the light path through the solution, c is the concentration of light adsorbing solute in the solution, and α is the molar absorptivity. When the Beer-Lambert law applies, the molar absorptivity is a constant and the absorbance is linearly related to the concentration of the solute. As the concentration goes above a certain amount, the relationship becomes non-linear and the absorptivity becomes a function of concentration.

The UV-vis spectrum of the TPAArVBA in aqueous solution between 200 and 300 nm reveals a significant peak with its maximum at 254 nm (Figure 2.5). This peak is

attributed to the double bond located on the end of the pendant vinylbenzyl groups, which are resonant with the nearby phenyl ring. The concentration of VBA groups was determined through NMR by comparison of the areas of the VBA peak at 5.0 ppm, the polymer backbone peak at 2.17 ppm and the TEA peak at 3.05 ppm. By determining the molar ratios of these components in the solid, the concentration of VBA groups per unit mass could be determined and subsequently the concentration in solution.

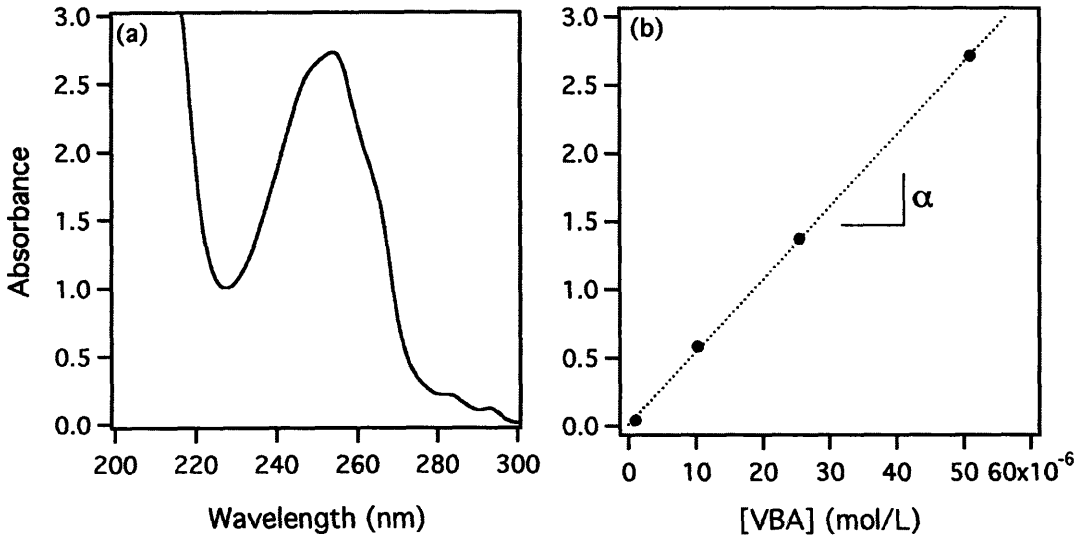

Figure 2.5. UV-vis spectroscopy of PAArVBA in solution. (a) The photoactive side group peak at 254 nm and (b) measurement of absorbance versus side group concentration showing a linear relationship.

The absorbance at 254 nm was determined from concentration measurements to obey the Beer-Lambert law up to 0.165 mM (of polymer repeat units) and within that regime, the molar absorptivity was determined to be $5.30\pm0.08\times10^{6}$ L mol^{-1} cm^{-1}.

The mechanism for crosslinking is assumed to be similar to that shown in Figure 2.6, where UV irradiation produces a triplet state and then free radicals at either end of the former double bond. The terminal radical is much more reactive and can attack

another double bond, or nearby polymer chains. This mechanism has been previously proposed to explain the UV induced autopolymerization and grafting of styrene [141]. Through the exposure of the solution to UV light at 254 nm, the crosslinking reaction can be followed through the decrease in the peak at 254 nm upon the loss of vinyl groups.

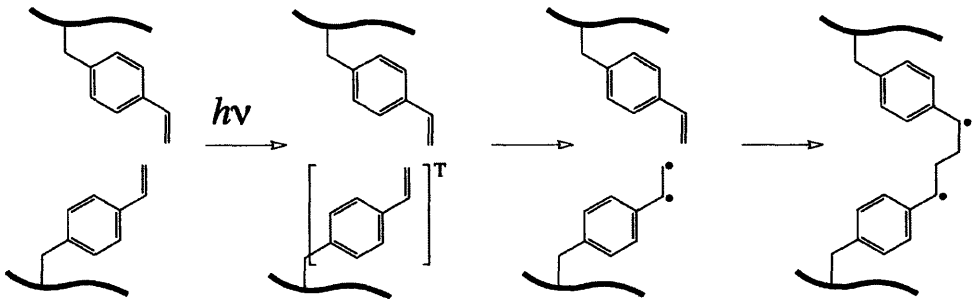

Figure 2.6. Possible mechanism for crosslinking. UV irradiation induces a singlet state leading to a stable triplet state followed by two free radicals. The terminal radical attacks nearby double bonds or other polymer chains.

Photon flux of the lamp was determined using the photoreaction of potassium iodide as an actinometer along with potassium iodate as an electron scavenger as described in the literature [142]. Briefly, solutions of 0.6 M potassium iodide and 0.1 M iodate in 0.01 M sodium tetraborate decahydrate buffer were measured with UV-vis and then exposed to radiation from our UV light source at the same distance as our crosslinking conditions for fixed amounts of time (30 seconds or one minute) and measured again. The reaction is given by

$$8I^- + IO_3^- + 3H_2O + h\nu \rightarrow 3I_3^- + 6OH^- \qquad (2.2)$$

The quantum yield of the reactants is 0.75 and with knowledge of the iodate and iodide concentrations, the number of photons directed at our samples was determined

from the increase in the absorbance peak at 352 nm due to the formation of triiodide from iodide (Figure 2.7).

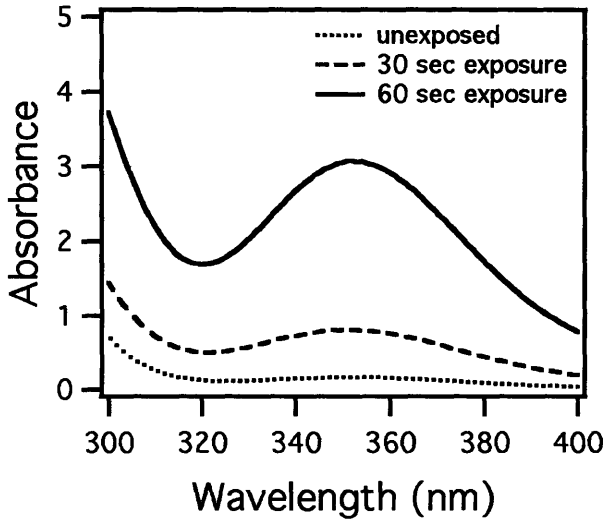

Figure 2.7. UV-vis spectroscopy of the photochemical formation of triiodide from iodide with 254 nm wvelength light. The increase in the adsorption peak of triiodide at 352 nm can be used to quantify the amount of light adsorbed by the sample.

One of the more common methods for quantifying a photochemical reaction is the quantum yield, which is calculated as the number of reaction events that occur per photon adsorbed by the reactants. Looking at the change in absorbance for a solution of PAArVBA before and after UV exposure, the number of reaction events N per unit volume can be defined by

$$N = \Delta C_{db} = \frac{\Delta A}{\alpha l} \qquad (2.3)$$

where ΔC_{db} is the change in concentration of double bonds, ΔA is the change in absorbance after exposure at 254 nm, and the path length l is 1 cm.

Through the potassium iodate actinometry, we can determine the incident photon flux at 254 nm for identical exposure conditions. By measuring the absorbance before and after the UV exposure, we can determine, using the concentration calibration, the change in the number of double bonds for any given exposure. From a series of one-minute exposures using the experimental setup, a quantum yield of 0.013 was calculated.

Table 2.1. Crosslinking properties of PAArVBA

% of vinylbenzyl side groups	Molar absorptivity	Quantum yield
3.1-6.0	$5.30 \pm 0.08 \times 10^6$ L mol^{-1} cm^{-1}	0.013

Chapter 3. Structural characterization of poly(acrylic acid-*ran*-vinylbenzyl acrylate) multilayers

Although the ability of multilayers to significantly change their structure with small changes in assembly conditions is beneficial for their versatility, it also means that unintentional or unavoidable changes in polymer composition can adversely influence their assembly behavior. The addition of vinylbenzyl groups to PAA to enable photo-activity can have unintended effects during assembly that must be characterized in order to predict and control final film structure.

3.1 Multilayer film assembly

Solutions of 10^{-2} M PAA and PAH in water were made from received materials (concentration based on the molecular weight per repeat unit). PAArVBA solutions of 0.375-0.400 mg/mL were made from the diluted aqueous product of the polymer synthesis or from the solid form. Polymer solution pH values were adjusted to within ±0.05 units of the noted pH by adding either 1M aqueous NaOH or HCl.

Silicon 3" x 0.5" substrates cut from 8" diameter p-type test wafers (University Wafer) were prepared by immersion overnight in chromic sulfuric acid while glass (VWR) and fused quartz (Quartz Scientific, Inc.) 3" x 1" slides were sonicated in detergent solution for 15-30 minutes. All substrates were then thoroughly rinsed with and sonicated in deionized (DI) water for a minimum of 15 minutes. Films were then assembled using an automated HMS series programmable slide stainer (Zeiss/Microm). Substrates were immersed in polycation solution for 15 min followed by immersion in three DI water rinse baths for 2, 1, and 1 min, respectively. Substrates were then

immersed in polyanion solution and rinse baths following the same pattern. This was repeated until the desired number of bilayers was achieved.

3.2 Measuring film thickness

Film thickness measurements were performed on a Gaertner 126B ellipsometer using a He-Ne 633 nm wavelength laser at an angle of incidence of 70°.

The most commonly measured property of multilayer films that is structure dependent is film thickness. To that end (PAH/TPAArVBA) films were constructed from pH-symmetric polymer solutions on silicon for ellipsometric thickness measurements in order to compare to (PAH/PAA) films. Ellipsometric measurements were taken of the (PAH/TPAArVBA) system for three separate samples at 15 and 16 bilayers each per pH assembly condition. Thickness was determined as the difference between 15 and 16 bilayers. Shown in Figure 3.1 is the thickness per bilayer at various pH, for the PAH/PAA system taken from Shiratori et al. [68], and the PAH/TPAArVBA system.

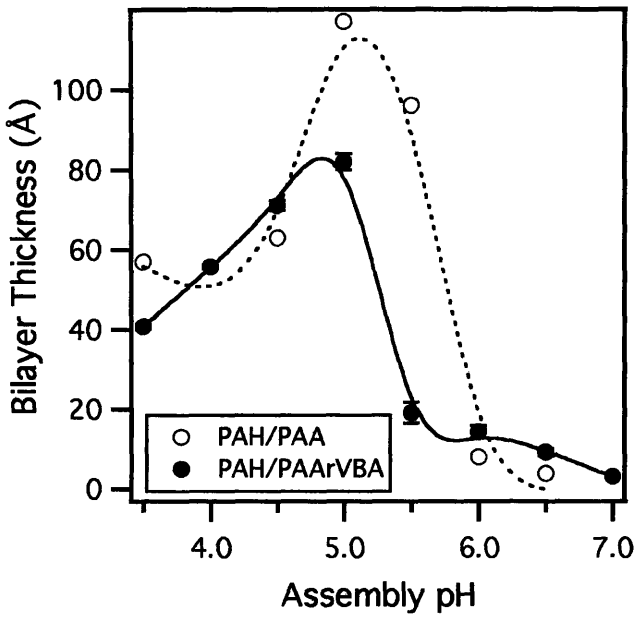

Figure 3.1. Thickness per bilayer versus assembly pH for the (PAH/TPAArVBA) system compared to literature data for (PAH/PAA) [68]. The critical pH at which the thickness drops discontinuously is lower for the (PAH/PAArVBA) system. Data measured from 15 and 16 bilayer films.

Both systems demonstrate similar trends in that the thickness of the films increases with increasing pH up to a critical point, where the thickness rapidly drops down to values close to the chain cross-section. This is attributed to the transition from a mismatch in charge density between the polycation and polyanion to a closely matched, fully charged state for both polyelectrolytes. The slight mismatch at lower pH causes a structure containing many internal loops, while the fully matched chains adopt a one-to-one correlation between charged side groups, giving a flatter, ladder-like conformation (Figure 3.2).

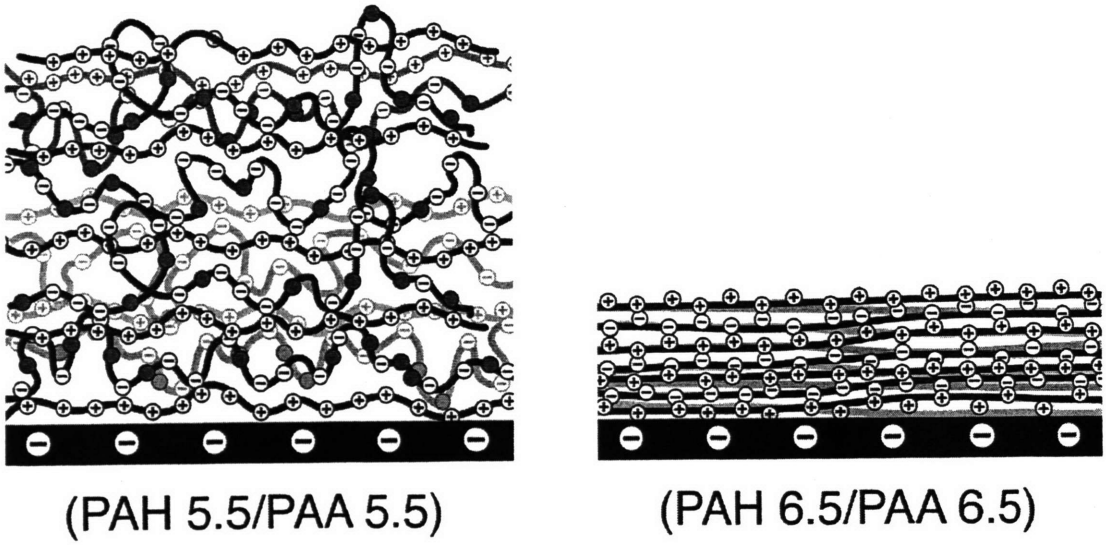

Figure 3.2. Simplified schematic of the difference in structure between (PAH 5.5/PAA 5.5) and (PAH 6.5/PAA 6.5) films. At pH 5.5, the polymer chains are slightly mismatched leading to frustrated, loopy conformations and greater film thickness. At pH 6.5, chain side groups are bound one-to-one in a "ladder" conformation.

The main difference in the thickness trends between the two polymer systems is that, for PAArVBA-containing films, the critical pH is lower than for those containing PAA. For the PAH/PAA system, the transition occurs between pH 5.5 and pH 6.0, while for the PAH/PAArVBA system the transition occurs between pH 5.0 and 5.5. This can be explained by the difference in structure between the two polymers. The vinylbenzyl side groups of PAArVBA, in addition to carrying no charge, are much larger than the acrylic acid side groups on PAA and PAArVBA. As such, there is a greater free volume associated with the polymer. Theoretical models have been developed to explain the abrupt thickness transition of weak PEMs by comparing the free energy state of a polyelectrolyte chain adsorbing in a loopy confirmation (entropically favorable) or in a flat confirmation (enthalpically favorable) [69, 70]. The transition occurs at a polymer

chain charge density where the former becomes greater than the latter. The adsorption free energy is linearly dependent on the free volume described by Park et al. as [69]

$$F_{ad} = F_{conf} + F_{stick} + F_{rep} \qquad (3.1)$$

where F_{conf} is the conformational free energy, F_{stick} is the free energy from the summation of all electrostatically paired segments, and F_{rep} is the segment-segment repulsive free energy. The segment-segment repulsive free energy is composed of an electrostatic contribution and a free volume contribution [69]

$$\beta F_{rep} \approx \frac{\pi f^2 N l_B \phi}{\kappa^3 H^3 a}(e^{-2\kappa H} - 1 + 2\kappa H) + \frac{1}{2}N\phi \qquad (3.2)$$

where $\beta = 1/k_BT$, l_B is the Bjerrum length, f is the ionization fraction, N is the number of chain segments, ϕ is the segment (or loop) volume fraction and κ is the Debye parameter [69]

$$\kappa \approx a\frac{(f_A + f_B)[segment] + [salt]}{3.04}\text{Å}^{-1} \qquad (3.3)$$

where f_A and f_B are the ionization fractions of the polyanion and polycation respectively, and a is the segment size. Any increases in the segment-segment repulsive free energy act to lower the critical pH at which the transition from a looped state to the fully flat state occurs. Free volume increases in the model act to lower the entropic favorability of the looped state, but the more significant influence is that of the electrostatic repulsion. Due to the uncharged nature of the vinylbenzyl groups, the PAArVBA ionization fraction at a given pH is effectively lowered relative to PAA. Thus f and κ are similarly decreased in the previous equation. The repulsive free energy is more strongly dependent

on κ, however, which should lead to an increase in F_{rep} for decreasing f_A and a subsequent decrease in the transition pH.

The other difference between the two systems is the thickness at pH $\geq$ 6.0. The PAH/PAArVBA system is slightly thicker in that pH regime and this is due to the TEA residue during assembly. Adding salt to polymer solutions during assembly has been shown to produce thicker films in strong polyelectrolyte films and this is likely what is occurring here.

3.3 Determining degree of crosslinking in PAH/PAArVBA films

In Figure 3.3 is shown the UV-vis absorbance spectrum for a (PAH 6.5/TPAArVBA 6.5)$_{40}$ film built on quartz which is transparent to a minimum wavelength of ~180 nm. When incorporated into multilayer films with PAH, the double bond peak at 254 nm is still visible in the UV-vis spectrum. We can use the presence of this peak to follow the progress of the crosslinking reaction. As the 254 nm peak decreases from increased exposure, a separate peak at 209 nm shifts to the left. This peak is attributed to the phenyl ring adjacent to the double bond on the side groups. The hypsochromic shift is due to the loss of conjugation between the phenyl rings and the vinyl groups, which are being consumed in the crosslinking reaction. From the graph, the peak at 254 nm is no longer visible after 15 minutes of exposure. This exposure time or longer was thus used to achieve full crosslinking of experimental samples.

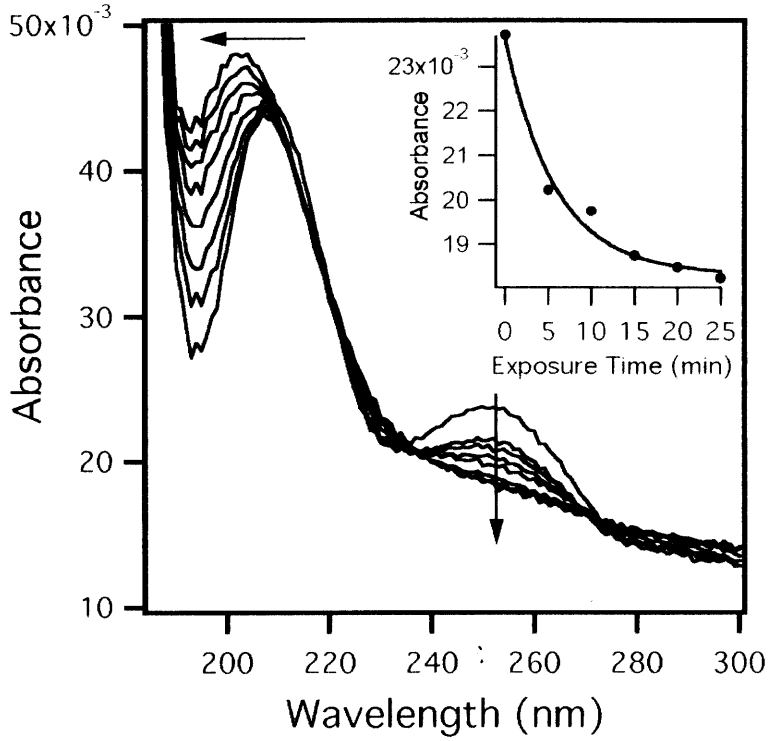

Figure 3.3. UV-vis spectrum of a (PAH 6.5/PAArVBA 6.5)$_{40}$ film on quartz. The photoactive peak at 254 nm decreases upon exposure to 254 nm wavelength light. The absorbance at 254 nm is almost flat at 15 minutes exposure (inset).

3.4 Crosslinking effects on swelling in PAH/PAArVBA films

3.4.1 Thickness measurements in aqueous solution

To determine the effects of crosslinking on the swelling ability of PAH/ PAArVBA films, multilayers were assembled at acidic pH, where PAH/PAA films are known to swell significantly in neutral or near-neutral pH due to the de-protonation of embedded carboxylate groups [127] (Figure 3.4). Fluid-cell ellipsometry was used to determine thickness of films built on reflective silicon substrates.

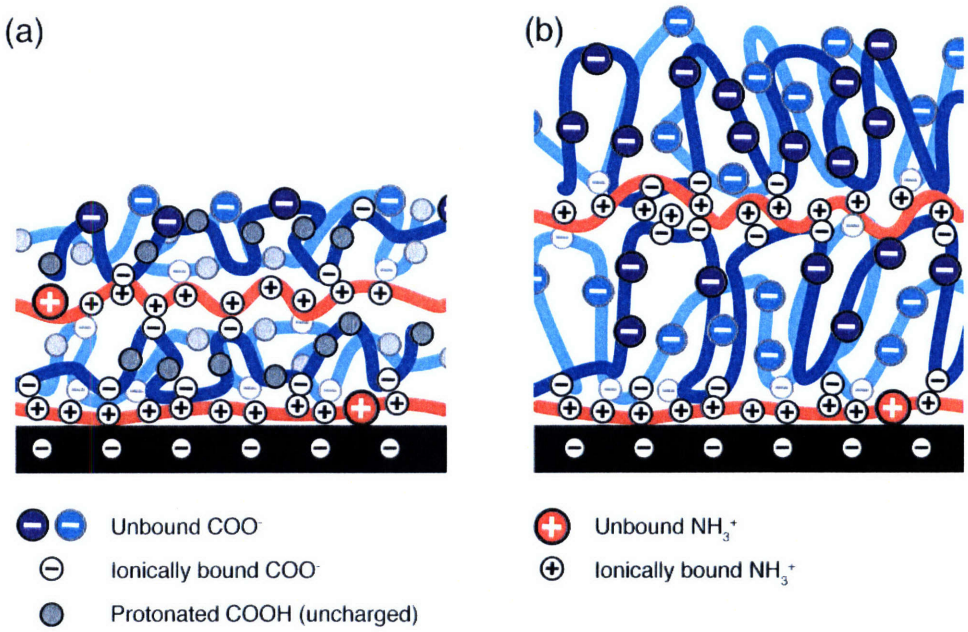

Figure 3.4. Simplified schematic of the swelling effect in (PAH/PAA) films assembled at low pH when placed into neutral pH. **(a)** During assembly, many of the side groups of PAA are protonated and uncoupled to a corresponding PAH side group. (b) In neutral water these groups become charged and repulse each other along with solvating water molecules leading to swelling.

Ellipsometry exploits the polarization of most electromagnetic plane waves. Light propagating in the z-direction of a Cartesian coordinate system will display a time dependent intensity that precesses elliptically in the plane normal to z. This intensity E can be described in vector form as

$$\vec{E}(t) = \begin{bmatrix} E_x(t) \\ E_y(t) \end{bmatrix} = \mathrm{Re}\left\{ \begin{bmatrix} Xe^{i\Delta} \\ Y \end{bmatrix} e^{i\omega(t-t_0)} \right\} \qquad (3.4)$$

where E_x and E_y are the x and y components of the intensity vector, Re is the real part of the expression, X and Y are the maximum amplitudes of the wave in the x and y directions respectively, t is the time, ω is the angular frequency and Δ is the relative phase of the wave [143]. The parameters commonly described in ellipsometry measurements are Δ

and ψ, where $\tan\psi = \gamma = X/Y$, and the state of elliptical polarization of light can be described by the Jones vector [143],

$$\begin{bmatrix} \sin\psi e^{i\Delta} \\ \cos\psi \end{bmatrix} \qquad (3.5)$$

By measuring the change in polarization of light after interacting with a sample, various properties about the sample can be determined. For isotropic thin films deposited on substrates of a known material, the refractive indices and thicknesses can be measured. In addition, with the proper model, these properties can be determined for more complex structures such as multi-stack films. While standard ellipsometry uses monochromatic light, typically from a laser, spectroscopic ellipsometry measures light from a wide range of the spectrum, giving greater accuracy.

Film thickness measurements were performed on a Gaertner 126B ellipsometer using a He-Ne 633 nm wavelength laser at an angle of incidence of 70° as described in section 2.4.2. For *in situ* aqueous measurements, samples were placed into a fluid cell with quartz windows constructed in-house after a similar cell described in the literature [144]. The windows for the cell were angled to be normal to the incident beam. Additional *in situ* measurements were performed with the same type of cell on a spectroscopic ellipsometer (J.A. Woollam, M2000-D) using a spectral range from 190 nm to 1000 nm.

Figure 3.5 shows the time dependent ellipsometric thickness for representative (PAH 3.0/TPAArVBA 3.0)$_{20}$ samples in pH 7.0 aqueous solution, one as-built, and the other UV exposed for 15 minutes. The degree of swelling ΔS is shown as

$$\Delta S = \frac{T_{wet} - T_{dry}}{T_{dry}} \qquad (3.6)$$

where T_{wet} *and* T_{dry} are the thicknesses in solution and in the dry state, respectively.

While the crosslinked film swells, the thickness change reaches a plateau at 20% of the dry film thickness. The as-built film shows a much greater degree of swelling, equal to double the thickness of the crosslinked films after 90 minutes.

It is worth noting the choice of pH 3.0 as the film assembly pH. Assembly at lower pH, which should result in a greater swelling differential, was not suitable for the PAH/PAArVBA system, as the as-built films were unstable and had a tendency to delaminate or disassemble in neutral pH aqueous solution. By contrast PAH/PAA films have been shown to be stable at pH 2.0. The difference can be attributed to the lower charge density of PAArVBA as compared to PAA.

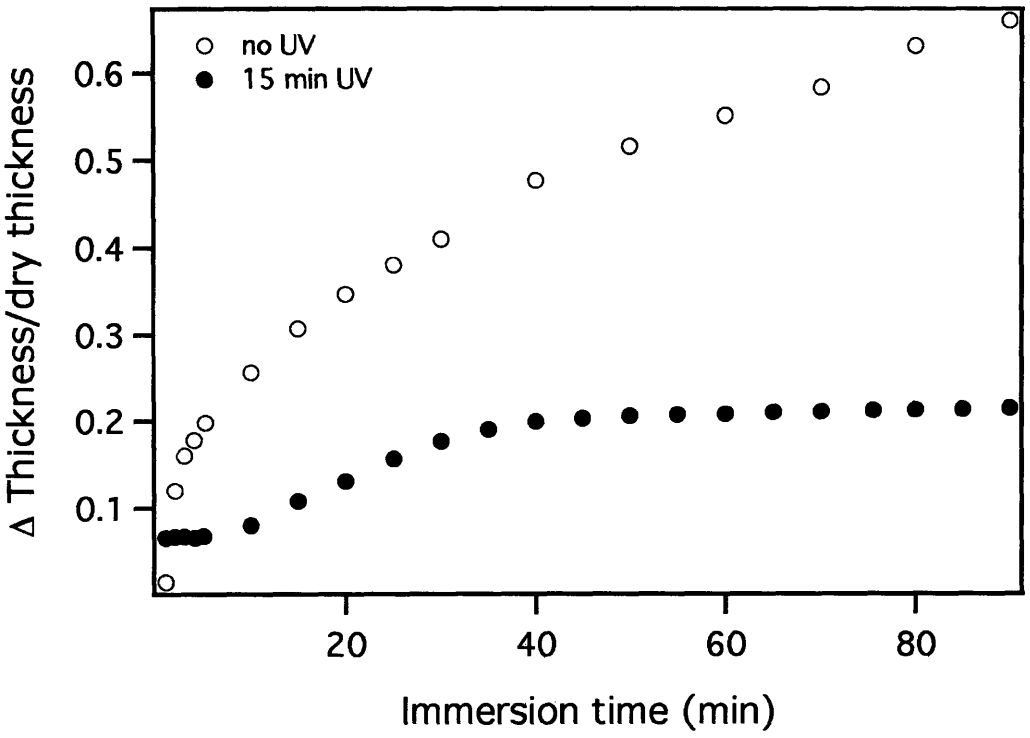

Figure 3.5. Ellipsometry of (PAH 3.0/TPAArVBA 3.0)$_{20}$ in water pH 7.0 crosslinked (●) and uncrosslinked (○). The crosslinked film shows a plateau in swelling as compared to the uncrosslinked film.

When assembled at a pH below the pKa of PAA, there are relatively few anionic groups for binding. In addition, the residual presence of triethylamine in the polymer when making solutions may influence the building behavior. If the TEA is fully charged in solution, it can act in a similar way to a salt, causing charge screening of the PAArVBA acrylic acid side chains, making the structure looser and more prone to instability. From NMR on the polymer batch used for this experiment, the TEA concentration is equivalent to 18% of the number of monomer units on the polymer. For a typical 10 mM solution of polymer, this is equivalent to 2 mM of TEA groups that are fully charged for these assembly conditions (pKb 11.01).

A similar behavior to that of the pH 2.0 assembled films in water was apparent for pH 3.0 assembled films in saline solutions. For biological applications, films are likely to be exposed to environments that contain salts and other charged molecules, so it is important that multilayer films remain stable under these conditions. To that end phosphate buffered saline, a common buffer for biological studies, was used to assess these effects on our system. Shown in Figure 3.6a is the γ vs. wavelength data for a (PAH 3.0/TPAArVBA 3.0)$_{20}$ uncrosslinked film in 1xPBS solution taken at various time points. The spectrum is relatively unchanged between 5 and 60 minutes, indicating that the majority of film swelling occurs within the first 5 minutes.

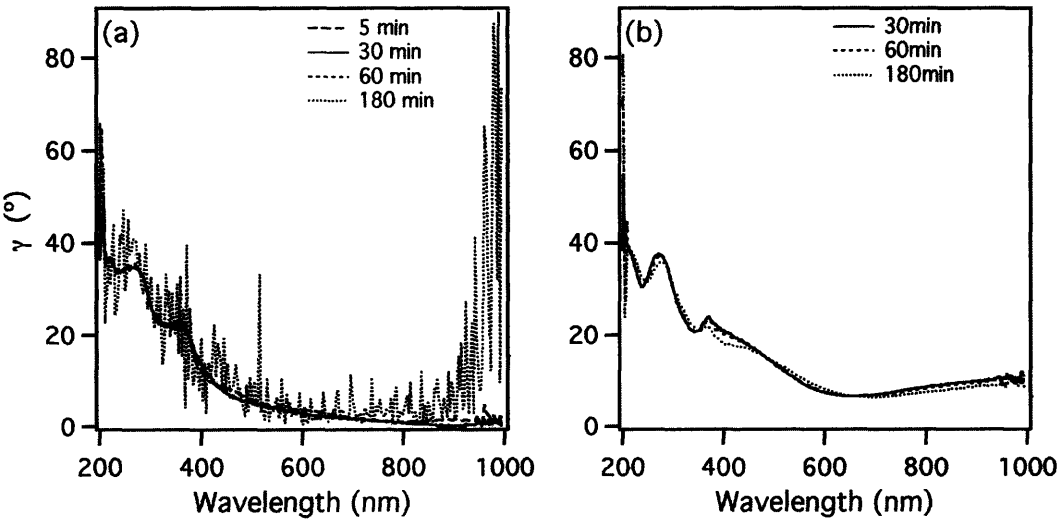

Figure 3.6. Ellipsometric spectra for an uncrosslinked (a) and 5 minutes crosslinked (b) film immersed in phosphate buffered saline. The uncrosslinked film begins to show an erratic spectrum after 1 hour in solution, while the crosslinked film spectrum remains stable.

At 180 minutes, however, the spectrum becomes erratic, indicating partial loss of film stability. For films UV exposed for 5 minutes, the ellipsometric data demonstrates stability out to 180 minutes, the extent of the measurement time. However, this stability

for lightly crosslinked films was not universal. We noted that in some cases, the stability of films crosslinked for 5 minutes was shorter-lived than that for films crosslinked for longer times (15 or 30 min).

Shown in Figure 3.7 is the time-dependent thickness for (PAH 3.5/TPAArVBA 3.5)$_{20}$ films in pH 7.1 aqueous solution for 3 different crosslink times as a function of immersion time. The lightly crosslinked film (5 min exposure) loses stability after approximately 20 minutes, while the other films remain stable.

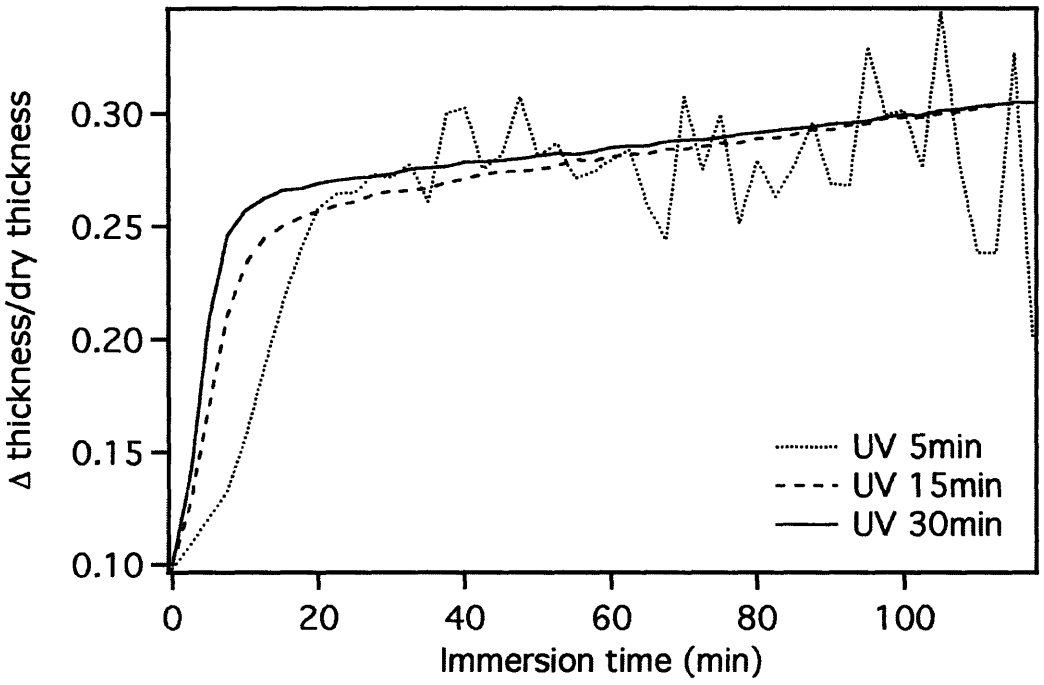

Figure 3.7. Ellipsometric thickness as a function of immersion time in pH 7 water, and crosslink time. Values from films crosslinked for 15 and 30 minutes are stable, while those from the film crosslinked for only 5 minute become erratic after 25 minutes.

3.4.2 Surface topography of patterned PAH/PAArVBA films in aqueous solution

To demonstrate patterning of the photo-crosslinkable PEMs in two dimensions, (PAH 3.0/TPAArVBA 3.0)$_{20}$ films were exposed to UV light using a chrome-coated quartz mask with regularly spaced 10 μm-diameter circular features. Atomic force microscopy (AFM) measurements were made on samples deposited on glass coverslips, attached by epoxy to Falcon 60 mm diameter polystyrene culture dishes and measured in various aqueous solutions using an MFP-3D (Asylum Research) with an Olympus Biolever gold-coated silicon nitride cantilever in both contact and AC (tapping) modes.

Contact mode images taken of a film surface in solution at pH 7.0 and pH 8.0 are shown in Figure 3.8. The unexposed regions are visibly more swollen than the surrounding crosslinked regions, confirming the results obtained from ellipsometry. For 20-bilayer films, the dry thickness is approximately 100 nm. The difference in height between swollen crosslinked and unexposed regions is roughly 15 nm, or 15%, after approximately 30 minutes in solution, consistent with swelling studies described in the previous section. When subjected to higher pH, a greater differential swelling is observed in the AFM cross-section. The swelling difference between crosslinked and unexposed regions is 30 nm at pH 8, after a similar amount of time in solution.

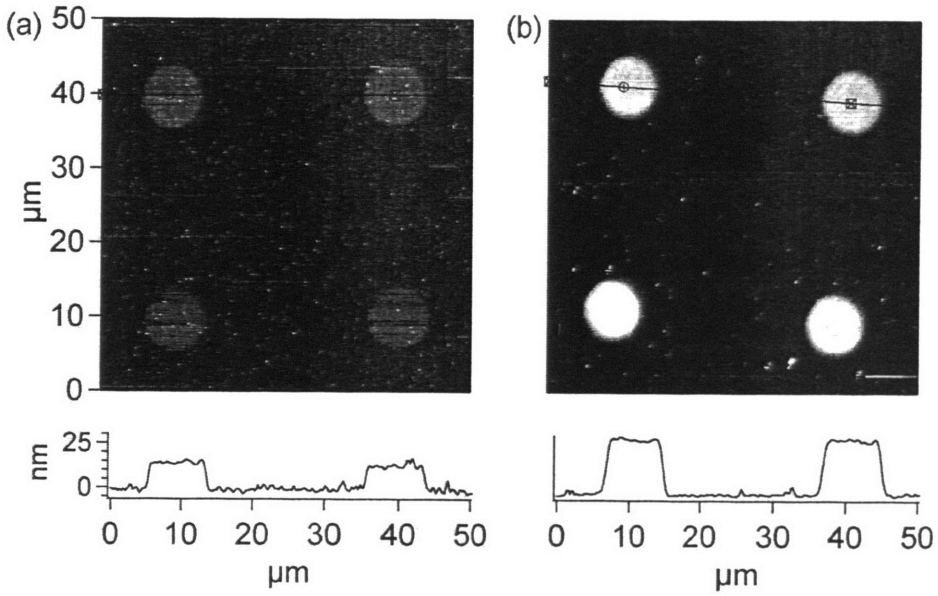

Figure 3.8. Atomic force microscopy top-down and profile images of a (PAH 3.0/ TPAArVBA 3.0)$_{20}$ film UV crosslinked with a positive dot-shape mask immersed in (a) pH 7 and (b) pH 8 solution. The film swells to a greater degree at higher pH due to increased deprotonation of acrylic acid side groups. Dot size is 10 μm.

The additional swelling at higher pH is consistent with the behavior of PAH/PAA films assembled at low pH [77]. The higher pH results in a greater number of acrylate groups on the PAArVBA chain becoming protonated, leading to greater chain-chain repulsion as well as an influx of small counterions and water molecules into the film. This is further evidence of unexposed PAArVBA behaving similarly to PAA. When immersed in a solution above the pKa of PAH, the films undergo a dramatic swelling transformation due to the sudden decrease in the number of amine binding groups. Shown is an image of the same film at pH 9.0 (Figure 3.9). The difference in thickness between the crosslinked and uncrosslinked regions increases to 1.05 μm–almost an order of magnitude of the thickness difference at pH 7. The scan of the masked regions in this case is only partial, as the extreme height of the sample caused difficulty in maintaining

proper contact between the probe tip and the surface. In addition, the swelling patterns of the film are the uncrosslinked regions. Ellipsometry suggests that these regions are somewhat unstable after a period of time in solution. Hence the impinging motion of the contact-mode tip may have been enough to pull the peaks off of the surface or tear the film in those regions. The strange surface features or artifacts above the midpoint of the top pair of dots supports this hypothesis, as this scan was taken by rastering upwards from the bottom of the image. If the film were pulled off partially, one would expect the flat surface of the crosslinked regions to be interrupted.

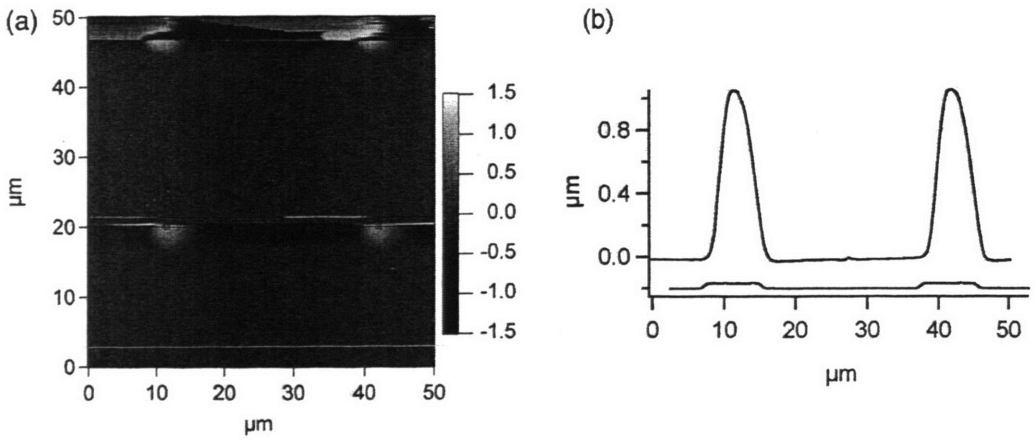

Figure 3.9. AFM of (PAH 3.0/TPAArVBA 3.0)$_{20}$ UV crosslinked with a positive circle mask, immersed in aqueous solution pH 9. (a) Top-down image (b) profile image, with pH 8 profile offset below for comparison. Dot size is 10 μm.

A separate film in aqueous solution above pH 8 gives an example of an intact pattern with swelling of the same order of magnitude as above (though lower), but without film damage (Figure 3.10). The 3 μm patterned dots swell significantly, showing that it is possible to achieve micron scale topological features from a nanometer thickness film simply through environmental pH changes.

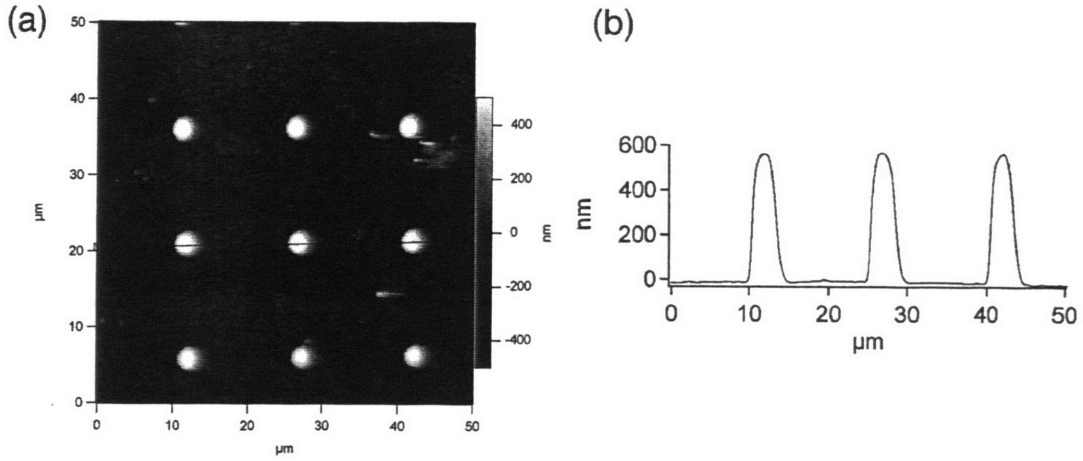

Figure 3.10. AFM image of UV-patterned (PAH 3.0/TPAArVBA 3.0)$_{20}$ in aqueous solution pH > 8. (a) Top-down and (b) profile images. Dot size is 3 μm

3.4.3 Mechanical compliance of PAH/PAArVBA films in aqueous solution

The atomic force microscope is a useful tool for measuring local elastic properties of surfaces and thin films due to its small measurement area (on the order of nanometers). It is also well suited for polymer systems because of the ability to generate very small forces and accurately record small deformations, which are necessary for materials with elastic moduli in the mega- and kilopascal range and below. One of the novel methods developed for determining elastic properties of thin polymer layers is direct indentation with an AFM probe, monitoring the deflection of the cantilever as the probe is brought into contact with the surface [145].

Using this technique with film thicknesses on the order of several hundreds of nanometers to microns is straightforward. The measurement of thinner films, i.e., below 300 nm, brings to the fore a new set of concerns, namely, effects from having a probe tip radius of the same scale as the film thickness, as well as the challenge of reaching an

indentation depth sufficient to give signal above thermal noise without registering the influence of the underlying substrate.

Several studies of indentation of nanometer-scale thickness polymer films have been published including for polyelectrolyte multilayer films [146]. Almost all of these begin from Hertzian contact models using a spherical geometry as an approximation of the parabolic end of a pyramidal AFM probe tip. The basic setup is shown in Figure 3.11 for a cantilever indenting a compliant surface (diagram based on similar image from [90]). The deflection is measured through the movement of the light spot reflected from the back of the cantilever, measured by a photodetector. The cantilever can be moved up or down through the actuation of a piezoelectric crystal located in the instrument head and the displacement **d** is directly measurable as the crystal produces a well-characterized movement based on input voltage for small enough actuation.

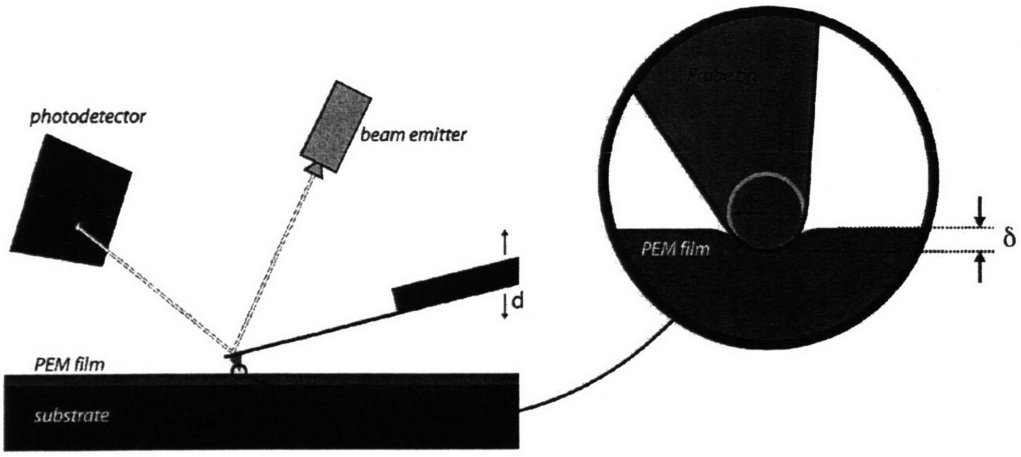

Figure 3.11. Schematic of nanoindentation experimental setup.

The Hertz model for a hard sphere impinging on a surface is derived from the case of two spheres impinging on each other with the assumptions of the radius of the surface "sphere" being much larger than the indentation sphere. Assuming that the cantilever tip is much harder than the film, the relationship between the indentation depth and the applied force is approximated as

$$P = \frac{4}{3}\frac{E}{(1-\nu^2)}R^{1/2}\delta^{3/2} \qquad (3.7)$$

where P is the force applied, E is the Young's modulus of the material, R is the effective radius of the indenter, δ is the depth of indentation into the film and ν is the Poisson's ratio of the film. The assumption for this model is that of a semi-infinite surface, which begins to break down when the film is thin enough to be influenced by the underlying substrate's mechanical properties. Several studies have looked at the applicability of this model to nanometer-scale films and the limitations on its accuracy [147, 148]. Dimitriadis et al. derived an extension of the Hertz equation for finite thickness samples as

$$P = \frac{4}{3}ER^{1/2}\delta^{1/2}[1 + 1.133\chi + 1.283\chi^2 + 0.769\chi^3 + 0.0975\chi^4] \qquad (3.8)$$

where $\chi = (R\delta)^{1/2}/h$ (h is the film thickness) and the Poisson's ratio ν is assumed to be 0.5 for an incompressible material. This extension was assumed to be significant when the first term was greater than 10% of the total force, or equivalently when $h \leq 12.8R$ [148].

More recently, modulus measurements of weak PEM films of 200 nm or less have been shown to be comparable to thicker systems under the right conditions of low strain [90]. Finite element analysis of indenter size and film thickness effects on modulus

accuracy have shown that for standard SPM indenter tip sizes (assumed to be 25 nm radius), films below 320 nm begin to show substrate influence, both for the Hertzian model and for the Dimitriadis extension. This overestimation of modulus for stiff substrates was reported to maximize at 89% for 50 nm thick films, which is still of the same order of magnitude [149].

A goal of this work was to determine whether the PAH/PAArVBA systems showed modified mechanical properties upon UV exposure using nanoindentation on UV exposed and unexposed films. Thompson et al. [90] have shown that the degree of swelling in weak polyelectrolyte multilayer films is directly related to their indentation modulus (which is in turn proportional to elasticity).

The actual parameters that are measured by the MFP3D for indentation are the change in photodetector signal from the light beam reflection off of the back of the cantilever versus sample z-displacement, which is separate from indentation depth δ in Figure 3.11. In order to translate those parameters into force (P) and δ several calibrations must be made prior to sample testing. The force on the cantilever is equal to the spring constant k times the deflection, so to determine the spring constant, the well known thermal fluctuation method is used [150]. Briefly, the cantilever at room temperature will oscillate due to thermal excitation. It can be approximated as a one-dimensional simple harmonic oscillator

$$k = \frac{k_B T}{\langle q^2 \rangle} \qquad (3.9)$$

where k_B is the Boltzmann constant, T is temperature and $\langle q^2 \rangle_s$ is the mean square cantilever displacement. A typical thermal measurement is plotted in Figure 3.12. As

shown, the MFP-3D software fits the first thermal resonance peak. The mean square displacement is equivalent to the integral of that peak, except that the thermal fluctuations are measured by the MFP-3D in (V^2/Hz), which is the output from the photodetector receiving light reflected from the back of the cantilever. To convert this spectrum to (m^2/Hz) requires knowledge of the inverse optical lever sensitivity (InvOLS), which is the voltage change in the photodetector response per unit of cantilever deflection, a value that changes from experiment to experiment. To determine the InvOLS, the cantilever is brought into contact with a non-deforming surface such as glass or mica, which gives a 1:1 correlation between the directly measurable z-axis sample displacement and the deflection. Measurement of the slope of the displacement-voltage curve gives the InvOLS value, which in turn allows calculation of the spring constant. For the cantilever used in these measurements, k was determined to be 0.01 N/m, 30% of the manufacturer reported value of 0.03 N/m.

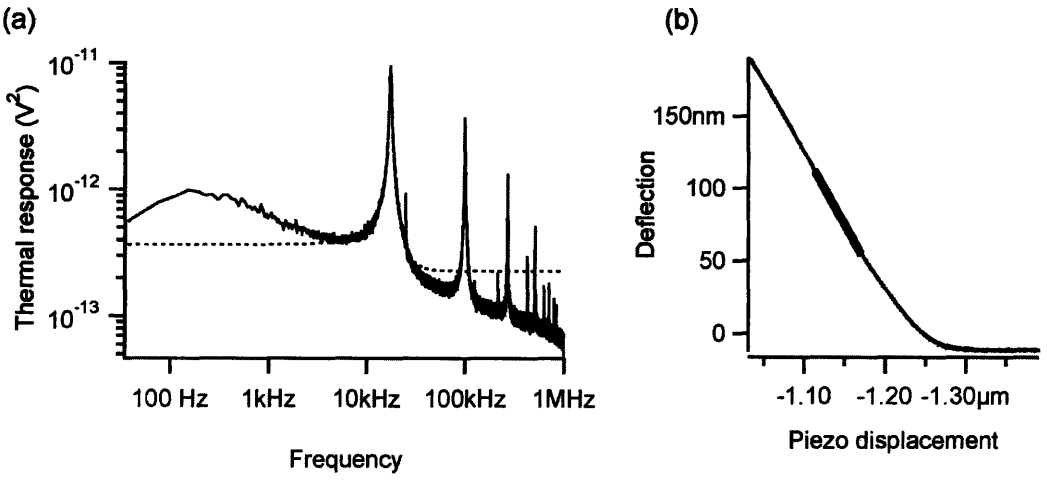

Figure 3.12. (a) Thermal resonance spectrum for a cantilever in the MFP-3D and software peak fit. (b) Calibration curve for determining InvOLS value. The thicker region of the curve is the linear fitting region.

The determination of the slope of the displacement-voltage curve, the integration of the thermal resonance peak (through a Lorentzian peak fit of the data) and the calculation of the spring constant are all semi-automated by the MFP-3D software package, run within the IGOR v5 software package (WaveMetrics, Inc.).

Samples of (PAH 3.5/TPAArVBA 3.5)$_{20}$ were built on glass slides, then cut to fit within and adhered by epoxy into Falcon 60 mm dia. culture dishes. Some samples were exposed to UV in the same manner as previously described. Samples were then immersed in PBS solution before and during indentation. The AFM probes used in these measurements were MLCT-AUNM-type (Veeco Instruments, Inc.). The cantilever used on the probe was the "D"-type, which has a V-shape and a vendor-estimated resonance frequency of 10-20 kHz. The radius of the indenting tip was taken as the manufacturer reported radius of 25 nm.

In order to avoid effects from the cantilever pressing against the surface before taking force measurements, samples were "scanned" only for a few lines at the bottom of the measurement field. This would produce a blank image field as the surface had not been scanned, but the scan field would be defined while leaving the surface untouched. For each measurement field, typically 20 μm^2, up to 60 points of contact were identified and a single force pull was taken at each point sequentially. The minimum distance between measurement points was 2 μm to insure that there was no influence of one measurement on the surface for the next measurement. The instrument was programmed to indent up to a cantilever deflection between 200 and 300 nm before withdrawing. All samples were tested with the same cantilever. Separate scans were performed on

identically built samples to determine the RMS surface roughness, which was calculated as 2.53 nm or lower for all conditions.

As the z-range of the piezo actuator is several microns, we were able to capture a large region of data before contact, which was used later for calibration of drift. Shown in Figure 3.13 is a set of typical data curves measuring force versus displacement. This data is converted from deflection versus LVDT, which is the signal from the piezo actuator. The absolute displacement is the difference between the piezo value for the movement **d** (Figure 3.11) and the deflection. The force acts as in a typical beam cantilever, $F = k\delta$, where k is the cantilever spring constant. The indentation depth δ is the difference between the displacement at any point and the displacement at the contact point. All data fitted was within a voltage range of the photodiode of –2V–0.7V. This is well within the linear voltage rage of the photodiode, which has been determined for this instrument to be approximately –6V–3V.

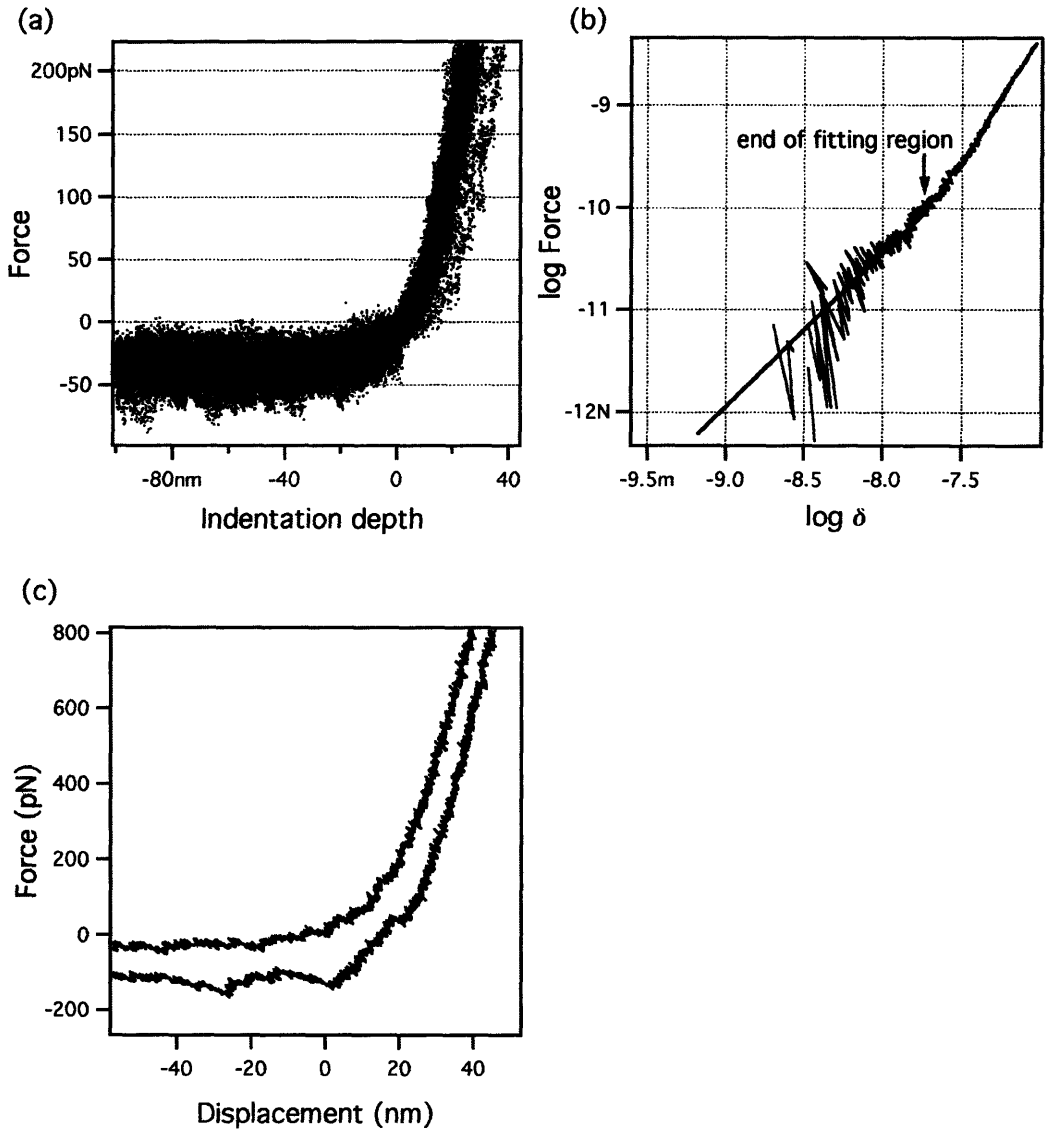

Figure 3.13. (a) A typical set of MFP-3D nanoindentation curves for (PAH 3.5/PAArVBA 3.5)$_{10.5}$ crosslinked for 15 min, (b) a single curve replotted on a log-log scale with "linear" fit and (c) a single approach and retraction curve.

To obtain a measure of the indentation modulus for a data set, several steps were necessary. Firstly, any drift in the cantilever deflection that showed up was corrected for by performing a linear fit of that region before contact and adjusting the whole curve under the assumption that the pre-contact region should have a zero slope. Secondly, the

curve was converted to log force versus displacement in order to find the contact point and fit for the modulus. The contact point was determined empirically by locating the region on the curve where the noise of the cantilever deflection became suppressed. This was in lieu of a jump to contact behavior, which was not observed. After this, the region directly following the contact point was fit to determine if the slope was between 1.49 and 1.51 (the exponent of the displacement in the Hertz model). In order to remain within the region of good agreement with the Hertz model, the fit was only extended to 20 nm past the contact point. After that, the probe tip cannot be reasonably modeled as a sphere. If the data didn't fit the slope, the fitting length was reduced until a fit was determined, or the number of points was assessed as too small to obtain a reasonable expectation of the behavior of the system. A minimum threshold of 60 data points was required to give a good fit, which was for the data density used, usually 5-6 nm. If no good fit was achieved at that point, the next point on the curve was named as the contact point and the fitting routine was repeated. This cycle of moving the contact point forward and performing a fitting routine was continued until a fit was achieved or until the "assumed" contact point was far out of the region of determined contact. From the fit, the value for the modulus was calculated. For the actual data sets, the minimum fit length used was 10.1 nm. In order to prevent completely erroneous or coincidental fits, all of the well-fitted curves were empirically compared for general shape and misshapen curves or curves with a significantly displaced contact point were discarded. The whole process for fitting and curve comparison was semi-automated using a function running in IGOR originally developed within the research group of Professor Krystyn Van Vliet and subsequently modified for increased automation. The system was assumed to be elastic

for the fitted region, though for the full indentation and retraction (which extend far beyond the fitted region), there is some non-elastic behavior evident. An example of this is shown in Figure 3.13c where the approach and retraction curves do not overlap completely and there is some sticking of the tip to the surface indicated by the negative force on retraction near the surface before a jump back to baseline. We assumed that the fitted region was elastic due to the 1.5 power-law dependence of the force on δ.

The results for (PAH 3.5/TPAArVBA 3.5)$_{20}$ films are shown as a function of UV irradiation time (Table 3.1). Each data value corresponds to two individual samples measured at three sample sites. The first significant finding is that the modulus measured for these films before crosslinking is significantly lower than for similar pH PAH/PAA systems. From Thompson et al., the most compliant system that they examined (PAH 2.0/PAA 2.0) had a modulus more than an order of magnitude higher than our (PAH 3.5/PAArVBA 3.5) system.

Table 3.1. Modulus versus crosslink time for (PAH 3.5/TPAArVBA 3.5)$_{10.5}$ films. Data for each exposure time is taken from three sample locations on two separate samples.

UV exposure time	Total number of indentation curves	Indentation modulus (kPa)	Standard deviation (kPa)	**Ratio**
0 min	19	25.3	10.8	0.427
15 min	25	133.8	41.5	0.310
30 min	32	125.8	46.4	0.369

The modulus of films crosslinked for 15 minutes and 30 minutes shows a significant increase over that of the uncrosslinked films, which supports the previous observations of swelling reduction. An unpaired t-test showed that the difference between 15 and 30 minute exposure times is statistically insignificant for a confidence interval of p=0.57, while both of those conditions showed a difference from the as-built

sample. For 15 min vs. as-built, $p=5x10^{-14}$ and for 30 min vs. as-built, $p=7x10^{-9}$. The statistically equivalent values for the two exposure times supports the UV-vis data showing that the majority of crosslinking occurs within the first 15 minutes. However, the increase in modulus still puts the films in the range of the (PAH 2.0/PAA 2.0) system. This is again likely due to the presence of TEA in the PAArVBA solution during assembly. As the stability was affected for films assembled near this pH, the same loosely bound together structure leads to softer films. The same effect would likely be observed for (PAH 2.0/PAA 2.0) films assembled with added salt.

Weak polyelectrolyte multilayer assemblies exhibit significant variability in properties as a function of assembly pH. This raises the possibility that films made using other sets of assembly pH would be able to exhibit UV exposure-dependent elasticity differences in other ranges. The large proportionate change in modulus is significant, considering the small amount of crosslinking in the film. This suggests that our system might restrain large-scale morphological changes in weak PEM systems.

Chapter 4. Controlling porosity transitions in PAArVBA-containing films with photocrosslinking

There are examples of polyelectrolyte multilayer films that undergo porosity transitions due to environmental changes in ionic strength [62] and porosity created through removal of sacrificial polymer [151]. The earliest method reported for inducing porosity in multilayer films however, was through changing the environmental pH for films constructed from weak polyelectrolytes [67].

Certain asymmetrically assembled weak PEM films are able to undergo a porosity transition when exposed to acidic solution. Polycation deposited at neutral to high pH assembled with polyanion deposited at low pH yields a film with a unique structure. When depositing from solution, PAA is relatively uncharged, leading to large numbers of loops and a rough surface. However, when PAH is depositing from solution, PAA is fully charged with many unpaired AA groups to assemble with. PAH, which is relatively charged in all cases, adsorbs strongly, with high interpenetration between chains. This can be qualitatively seen in the change in surface roughness of dried films, depending on which polymer is the top layer (Figure 4.1). This pattern of assembly also makes possible structural rearrangements when these films are subjected to an environment below the pKa of PAA within the film (pH < 2.5) [67]. This environment severely reduces the number of charged acid groups available for binding, and if the pH is low enough (<1.75), leads to the dissolution of the film [67].

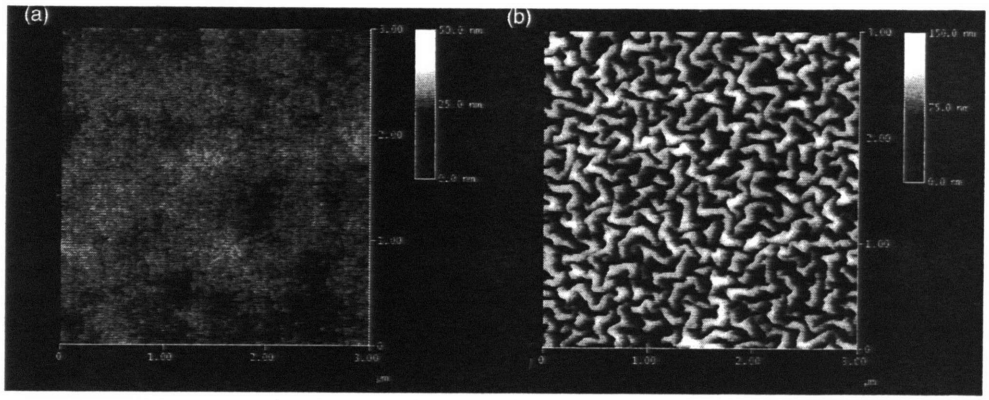

Figure 4.1. AFM images of (a) PAH-topped and (b) PAArVBA-topped (PAH 7.5/ TPAArVBA 3.5) films. The surface structure is highly dependent on which polymer is the top layer. Height color bar for (a) 50 nm, (b) 150 nm.

In the pH regime between the pKa of PAA and the dissolution point, the protonation of acrylic acid side groups breaks many of the PAA electrostatic binding pairs with PAH, allowing much greater chain conformational freedom for both polyelectrolytes. When returned to neutral pH, the film undergoes a water-polymer phase separation that on short time scales creates a continuous microporous network and on longer scales moves towards the thermodynamically stable dense film state (shown in Figure 4.2 with some through-pore defects, from [67]).

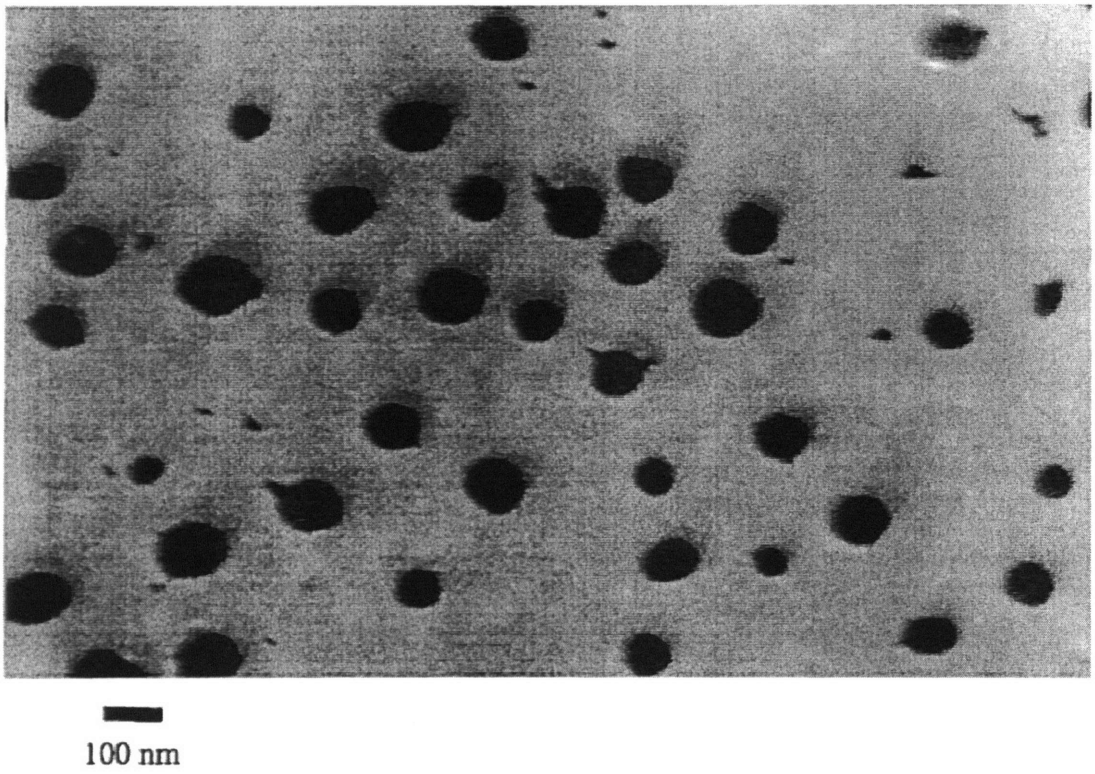

Figure 4.2. SEM of porous (PAH 7.5/PAA 3.5) film after annealing in water for 1 hour. Image from reference [67].

Similarly, films assembled as (PAH 8.5/PAA 3.5) have exhibited nanoporous transitions by the same mechanism when exposed to pH below the pKa of PAA [78]. Nanopore-forming systems for short enough exposures to low and neutral pH solutions, can shuttle between open and closed pores over many cycles. The changes in structure are accompanied by changes in film properties such as refractive index (*n)* [79], and affinity for chemical adsorption [80].

Since it is the breaking of ionic bonds that prompts film reorganization, our photo-crosslinking system should enable us to selectively inhibit the formation of pores by forming covalent bonds. This may lead to applications that take advantage of locally modified film porosity.

4.1 Controlling porosity transitions in microporous multilayer films

4.1.1 Experimental methods

Films were assembled on glass and silicon substrates in the same method as described in section 3.1. (PAH 7.5/TPAArVBA 3.5)$_{20.5}$ films were exposed to UV irradiation for 20 minutes using the setup described in Section 3.3. Films were then immersed in aqueous solution pH-adjusted to 2.3 ± 0.02 with HCl for varying lengths of time, followed by a DI water immersion (pH ~5.5-6) for 10 s, and then blown dry in a focused air stream. AFM surface measurements were taken in air in tapping mode using a Veeco D3000 AFM with a TAP300 cantilever (Nanodevices, resonant frequency 300 kHz) both before and after acid exposure. Spectroscopic ellipsometry measurements in open air were taken using the same apparatus described in Section 3.4.1, on films built on Si substrates. Three samples were measured for each data point.

4.1.2 Results and discussion

Shown in Figure 4.3 are the thicknesses and refractive indices of crosslinked and uncrosslinked films versus acid exposure time. The y-axis for the first and second graph is the ratio between the film refractive index and thickness, respectively, as-built and after the acid exposure; and between the films as-built and after the rinse, which are plotted as separate data sets. For as-built films the thickness was 226.0 ± 2.3 nm while for crosslinked films, the thickness was 221.4 ± 2.2 nm.

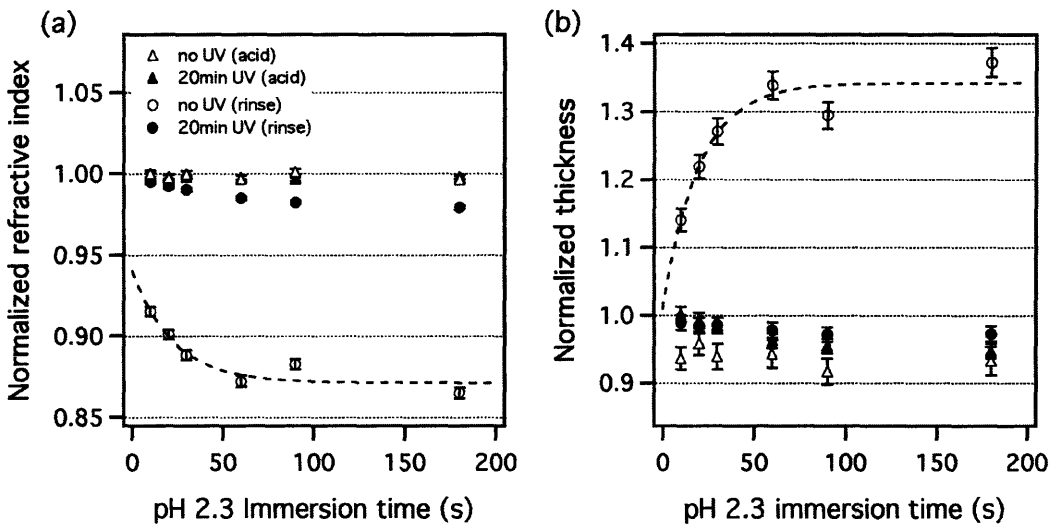

Figure 4.3. Thickness and refractive index changes in (PAH 7.5/TPAArVBA 3.5)$_{10.5}$ films as a function of acid immersion time. All rinsed samples were rinsed for 90 s in deionized water. The y-axes normalized to the pre-treated state of the sample films.

Like previous observations for (PAH 7.5/PAA 3.5) systems, the immersion in acid does not immediately cause the microporous transition to occur. Under those conditions, one would expect the thickness to increase and the refractive index to decrease as the polymer film (n ~1.54) becomes a "composite" of polymer and air ($n \approx$ 1.0). The acid-treated/initial thickness ratio values for both as-built and crosslinked films (open and filled shapes, respectively) show rather, a nominal decrease, indicating either film densification, or loss of material rather than pore formation. For densification, one would expect an increase in refractive index, as more of the film is made of polymer and less of air, but this does not appear to be the case. In fact, the refractive index stays close to its original value, which suggests that there is some material loss. Previous studies of (PAH 7.5/PAA 3.5) gave no evidence that immersion in pH 2.3 solution caused material loss [67]. The explanation for the loss then must be linked to a difference between PAA and PAArVBA in the multilayer structure.

It was observed in Section 3.2 that for pH-symmetrically assembled PAH/PAArVBA multilayers (PAH 3.0/PAArVBA 3.0, PAH 4.0/PAArVBA 4.0, and so on), the lower charge density on the PAArVBA chain had an effect on the critical pH of the thickness transition from loopy chains to tightly stitched chains. Here, the lower charge density may have an effect on the overall stability of these films.

Nolte et al. have observed a phenomenon whereby PAH/PAA films will partially dissolve or etch in high salt solutions and the percentage of dissolution has a strong dependence on the solution ionic strength. The root cause of the partial dissolution is the increased solubility of PAH-PAA complexes with high asymmetries in chain length, i.e., short PAA chains complexed with long PAH chains and vice versa. More closely matched chains will remain stable within the film [Nolte, submitted]. This effect could be especially significant for our system, as the commercial PAA used in this study for synthesis of PAArVBA (Polysciences, 90.000 M_n) has a polydispersity of ~6.2. Low pH coupled with the reduced charge density on the PAArVBA chain as compared to PAA, along with the effectively increased ionic strength from the presence of TEA, may act equivalently to high ionic strength for PAA-containing films. This could result in partial removal of (high M_w PAH)/(low M_w PAArVBA) complexes from the films. The (PAH 7.5/PAA 3.5) system behaves similarly to our (PAH 7.5/TPAArVBA 3.5) system in that the porosity transition does not occur immediately upon treatment with acid, but only after the neutral rinse step [67]. Whether this dissolution effect also occurs in that system has not been documented.

The most dramatic difference in thickness for the displayed data is that for as-built films after rinsing vs. before treatment. As expected for a microporous transition,

the thickness increases, while the refractive index drops. In addition, although it does not become apparent until after the rinse step, the duration of acid immersion has an effect on the extent of the transformation. For longer times in pH 2.3, the thickness increases and the refractive index correspondingly decreases, though this behavior reaches a plateau. Below the pKa of PAArVBA ionically bound amine and acrylic acid side groups prevent film dissolution while film reorganization is occurring.

UV-exposed films show a noticeably different behavior after rinsing in DI water. The change in both the thickness and refractive index as compared to the non-crosslinked films is almost negligible, due to the covalent bonds restricting segmental motion. This change is not zero however, as the refractive index of these films does decrease. The thickness ratio of rinsed films to before acid treatment films is less than one, but the measure of porosity must take into account the partial dissolution during the acid immersion. In examining the thickness increase from post-acid immersion to post-rinse these films can be seen as displaying a small amount of porosity. For 180 s acid immersions, the crosslinked films indicate a porosity of 2%, while the non-crosslinked films show a porosity of 32%. AFM images of the films after rinsing show this difference qualitatively in Figure 4.4 through the surface roughness.

As with the ellipsometry data, the un-crosslinked films' surfaces show increasing porosity with increasing acid immersion time. The crosslinked films show little change in structure for the length of the acid treatment. This marked difference opens up the possibility of lateral control of microporosity through photo-crosslinking.

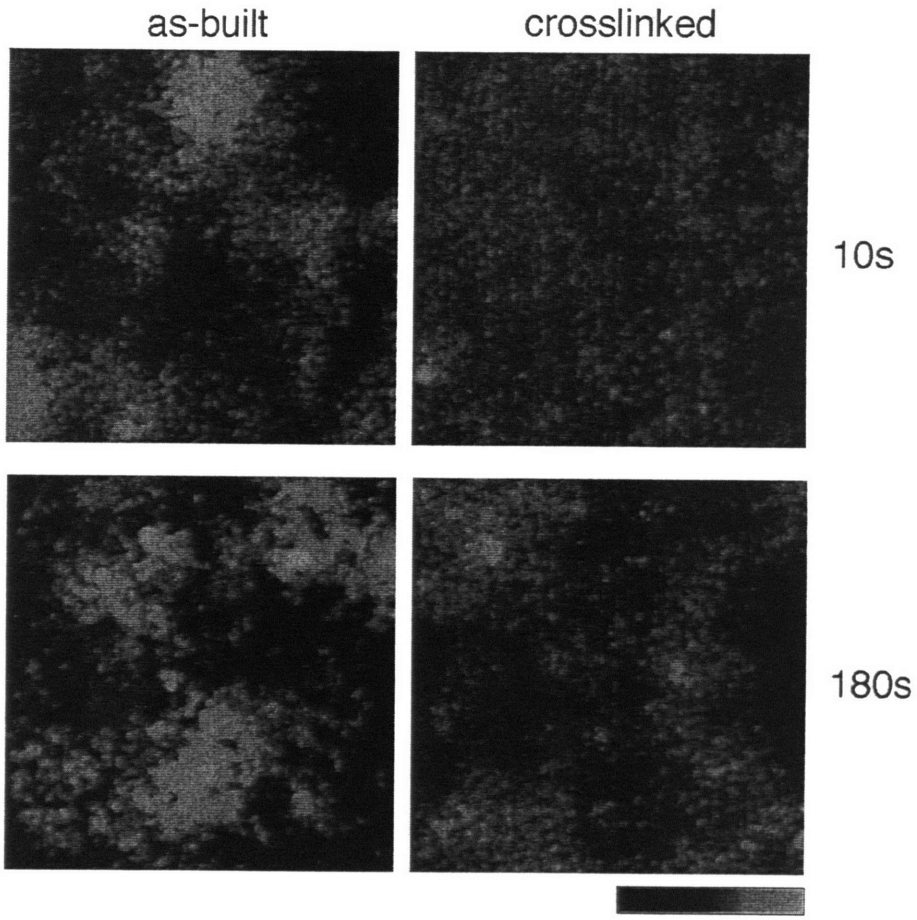

Figure 4.4. AFM images of (PAH 7.5/TPAArVBA 3.5)$_{10.5}$ films exposed to pH 2.3 for varying times and then rinsed in deionized water for 90 s. The uncrosslinked films show increasing surface roughness, while the crosslinked films remain static. Each image is 5x5 μm^2 and the height color bar is 50 nm.

4.2 Controlling porosity transitions in nanoporous multilayer films

Studies of the (PAH 8.5/PAA 3.5) system have shown that the nanoporous transition, like the microporous transition, requires sequential exposure of the film to acidic and neutral or near-neutral pH solutions [78]. Furthermore, the pores once formed can be closed reversibly through re-immersion of these films in acidic solution. Films of

this type have demonstrated useful anti-reflection properties [78], as well as potential as substrates for controlled drug release [80]. The ability to spatially control the formation of nanopores holds the same promise as that for micropores, namely, spatial control of film properties, possibly allowing selective drug release or patterned optical structures. In order to assess the ability of our polymer system to control nanopore formation, we seek to understand the basic effects of crosslinking on (PAH 8.5/PAArVBA 3.5) films. While this study has similarities to that of the (7.5/3.5) system, in this case the reversible pore expansion and collapse behavior also must be examined.

4.2.1 Experimental methods

Films were assembled as in section 3.1 and treated with acidic and neutral aqueous solutions in the same manner as the previous section. $(PAH\ 8.5/TPAArVBA)_{20.5}$ films built on silicon were examined using spectroscopic ellipsometry. One sample for each cycle time was measured, immersed in pH 2.3 solution, blown dry, and remeasured. Samples were then immersed in pH 5.5-6 aqueous solution, blown dry, and again remeasured. This cycle of immersion in pH 2.3 and immersion in pH 5.5-6 was repeated several times to yield thickness and refractive index data on the reversibility of the films' nanoporosity.

4.2.2 Results and discussion

As displayed in Figure 4.5, the nanoporous transition occurs readily in uncrosslinked films (open shapes) only after exposure to acidic conditions followed by rinsing in near neutral conditions. The porosity is evidenced by the increasing thickness and the decreasing RI of the films. This behavior is in agreement with previous studies on the (PAH 8.5/PAA 3.5) system. The nature of the transition is dependent on the acid

exposure time as well as the number of acid-rinse cycles. For acid immersion times of 5 s (a), 15 s (b), 30 s (c), and 90 s (d), the films require multiple cycles to reach a point where the porosity in the open pore state is constant with respect to cycling. This appears to occur at the fifth cycle for all of these immersion times. The initial cycle is sufficient to cause a drop in refractive index, however, for all of the immersion times studied.

There is also a difference in the amplitude of the thickness change as a function of the immersion time in acid. For increasing acid immersion time, the thickness after a full cycle increases, but the pores still collapse to the same level in acid. This implies that the mechanism for the porosity transition is dependent on a transformation that is occurring during the acid immersion, which correlates with our study of the (PAH 7.5/TPAArVBA 3.5) system.

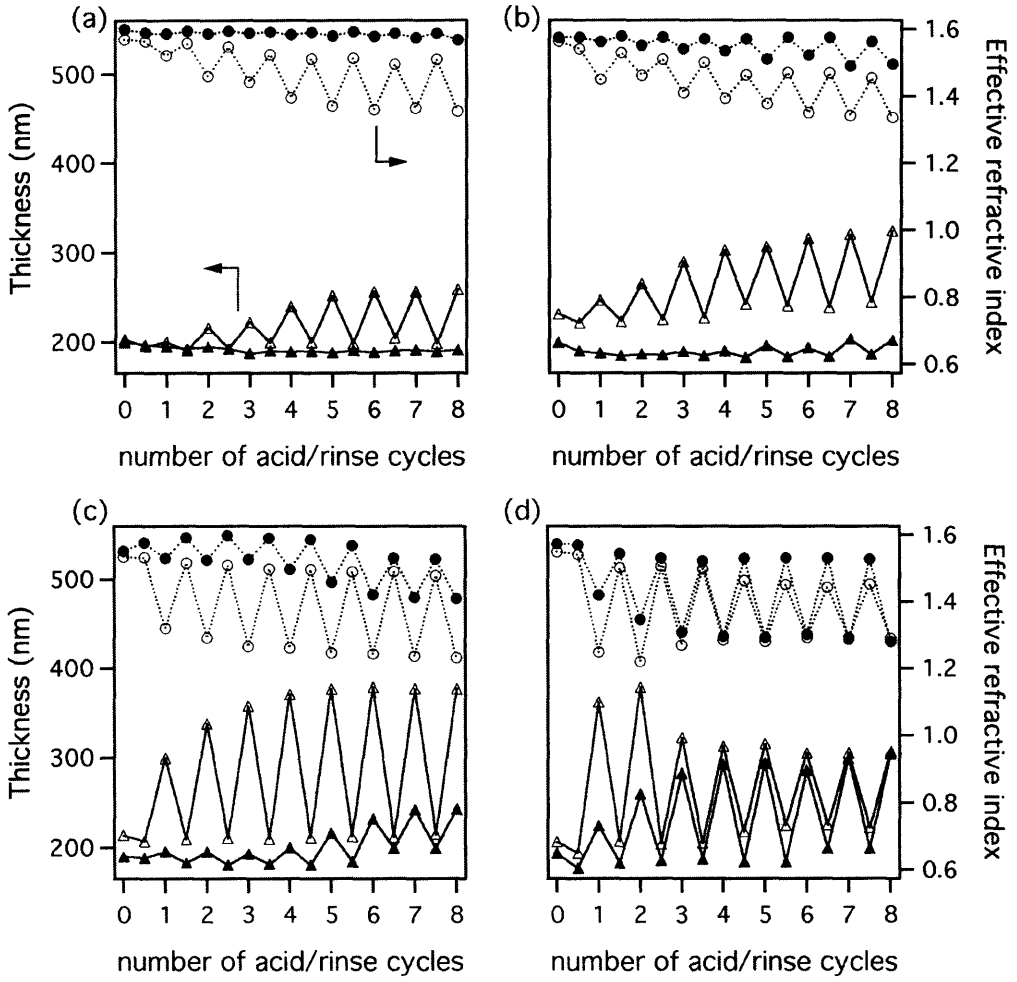

Figure 4.5. Thickness and refractive index values from ellipsometry on films cycled between pH 2.3 for (a) 5 s, (b) 15 s, (c) 30 s and (d) 90 s; and deionized water for 90 s. (filled shapes) refer to crosslinked thickness and refractive index and (open shapes) refer to uncrosslinked thickness and refractive index.

Crosslinked films (filled shapes) show a marked difference in the degree of structural transformation vs. uncrosslinked films. The porosity for all of the immersion conditions is suppressed, as evidenced by the lower thickness increases and the smaller decreases in RI, though it is not completely inhibited. In fact, for the 90 s acid immersion case (d), the crosslinked film reaches an equilibrium open porosity essentially equivalent

to that of the uncrosslinked film. Only in the 5 s immersion case is there no significant evidence of porosity after eight cycles.

Samples made using the purer synthesized polymer catalyzed with 1,8-diazabicyclo[5.4.0]undec-7-ene (DBU) (see section 2.3.2) were cycled through the pore opening and closing to determine if there was a difference in behavior, in preparation for their use in Bragg reflector films. Figure 4.6 shows the comparison between films made with (a) TPAArVBA, and (b) DPAArVBA, cycled between pH 2.3 and DI water for 90 s each. The films made with DPAArVBA are initially much thicker (150 nm for 10.5 bilayers to 200nm for 20.5 bilayers). In addition, there is a marked difference in the ability of the two polymers to inhibit pore opening under these conditions. DPAArVBA-containing films completely inhibit pore formation, while TPAArVBA-containing films act as though uncrosslinked after a couple of cycles, as previously noted. In addition, the DPAArVBA-containing as-built films show a slow increase in pore size per cycle as compared to TEA-catalyzed. This suggests that DPAArVBA-containing films subjected to shorter acid immersion times might require more cycles to achieve the same porosity as their TPAArVBA-containing counterparts.

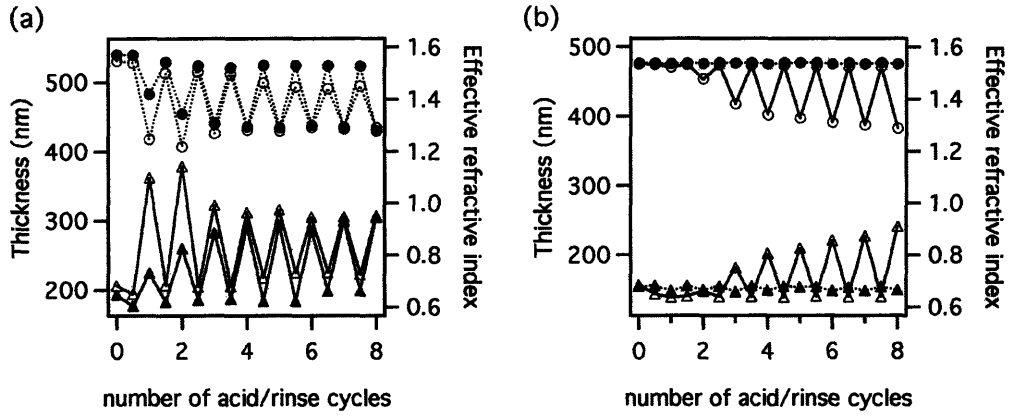

Figure 4.6. Thickness and refractive index from films cycled between 90 s at pH 2.3 and 90 s in deionized water. (a) TPAArVBA-containing system (b) DPAArVBA-containing system.

AFM measurements of these films show evidence of porosity as well as the effect of rinse time on pore structure (Figure 4.7). Shown are 5x5 μm^2 surface images of (PAH 8.5/TPAArVBA 3.5)$_{10.5}$ after immersion in pH 2.3 for 15 s and subsequent rinsing for 15 s, 1 min, and 3 min. There are clearly observable sub-micron scale pores throughout the films, with some variation in size, though most are less than 100 nm. The overall effect of longer rinse times appears to be the smoothing of the surface and reduction in the pore size. There appears to be an overall reduction in the pore number, but as the pore size in this case is close to or smaller than the radius of the AFM probe tip, it is hard to definitively state that pores are disappearing. They may be simply unresolvable with the instrument. In addition, it is uncertain whether the reduction in pores is occurring through the bulk of the film, or is merely a surface phenomenon.

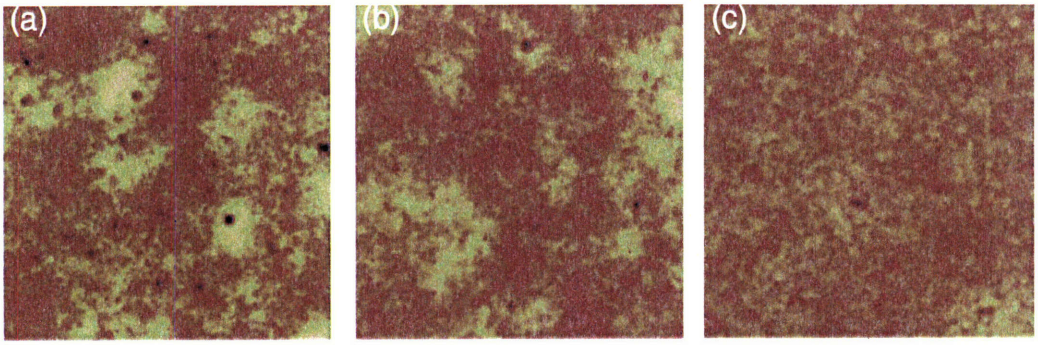

Figure 4.7. AFM of (PAH 8.5/TPAArVBA 3.5)$_{10.5}$ films immersed in pH 2.3 for 15 s and deionized water for (a) 15 s (b) 1 min (c) 3 min. Longer rinse times reduce visible surface porosity.

4.3 Lateral patterning of porosity in PAArVBA-containing multilayer films

Spatial control of porosity in PEM films can be demonstrated by 2-dimensional patterning through masked UV light exposure and subsequent porosity treatments for both microporous and nanoporous films. By using a reflective substrate, changes in thickness due to pore formation are readily observable by changes in the interference colors generated by the film.

4.3.1 Experimental methods

Single samples of (PAH 7.5/TPAArVBA 3.5)$_{20}$ and (PAH 8.5/DPAArVBA 3.5)$_{10}$ were assembled on glass and silicon according to the method described in Section 3.1, covered with a photomask and exposed to UV for 15 minutes. (PAH 7.5/TPAArVBA 3.5) films were then immersed into pH 2.3 aqueous solution for 30 s followed by a 10 s DI water rinse (pH 5.5-6.0) and blown dry in a directed air stream. Films were cycled through pH 2.3 aqueous solution (5 s) and DI water (90 s) 5-10 times as in the previous section and then thermally crosslinked at 180°C for 4 hours to stabilize the structure. The

thermal crosslinking was necessary for later studies of patterned Bragg reflectors, so it was employed here to provide a more direct comparison. Samples were examined using optical microscopy, tapping mode AFM using the D3000, and profilometry with a P10 Surface Profiler (Tencor).

4.3.2 Results and discussion

Figure 4.8 shows an optical micrograph of a TEM grid used as a photomask (a) and a representative (PAH 7.5/TPAArVBA 3.5)$_{20}$ film after treatment (b). Regions that were blocked by the grid show the characteristic microporous morphology, while exposed regions show no visible changes, consistent with ellipsometric measurements on unmasked, exposed films. The image also reveals a difference in the width for the three struts extending from each central node on the film. This is due to the particular shape of the TEM grid, where although the strut thickness does not vary significantly, the structure is not completely flat. The struts that yielded the thinnest pattern in the multilayer were elevated slightly from the surface of the film during UV exposure while the thickest struts were flush against the surface.

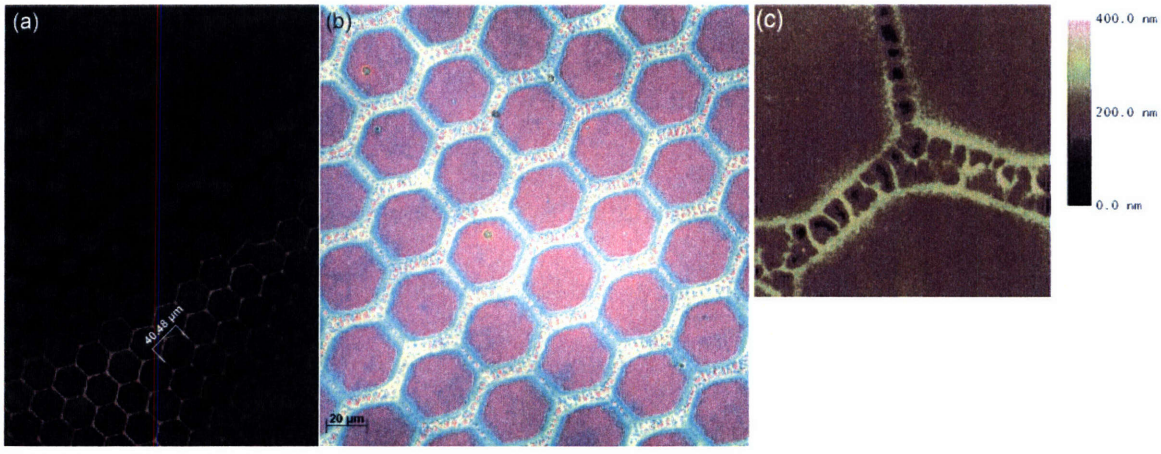

Figure 4.8. (a) Microscopy image of a TEM grid. (b) (PAH 7.5/TPAArVBA 3.5)$_{20}$ film UV crosslinked with the TEM grid mask. (c) AFM of one node in the film. Color height scale bar is 400 nm.

AFM measurements of the same surface confirm this structure, and show the effect of restricting the pore-forming region in the film (c). All of the pores in the narrowest arms have edges that are nearly perpendicular to the arm length, rather than the more random structure along the wider arms. However at the interface between the porous regions and the nonporous regions, the pore edges all start normal or nearly normal to the interface edge. The pore wall height varies depending on location within the pattern. For the thinner struts, which we presume to have had some UV exposure, the edge height rises up to 95 nm above the crosslinked film regions. This value is within 40% of the plateau value for the non-patterned, porous films (section 4.2.2). On the wider struts, the pore edge thickness is closer to 145 nm, which is much greater than for the non-patterned films (Figure 4.9).

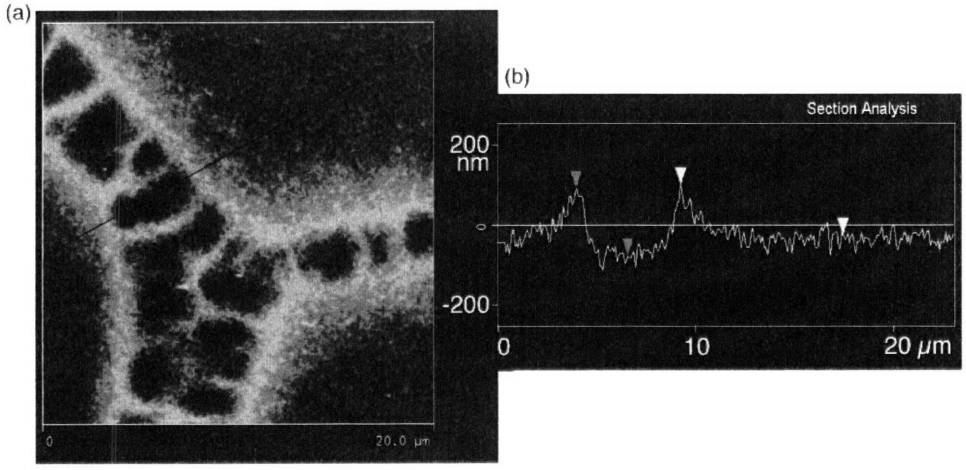

Figure 4.9. AFM of one node in TEM patterned (PAH 7.5/TPAArVBA 3.5)$_{20}$ film. Height range is 200 nm. (b) The cross-section of one patterned arm shows the raised edge between the porous and crosslinked film regions.

Films patterned with a different photomask show similarly influenced pore structures. Shown in Figure 4.10a is an optical micrograph of a film patterned with a

photomask containing circles of 5 μm diameter. Again the pore walls tend to begin normal to the edge of the interfacial regions. The crosslinked regions maintain the surface topography of the PAArVBA-topped (PAH 7.5/TPAArVBA 3.5) film (Figure 4.11).

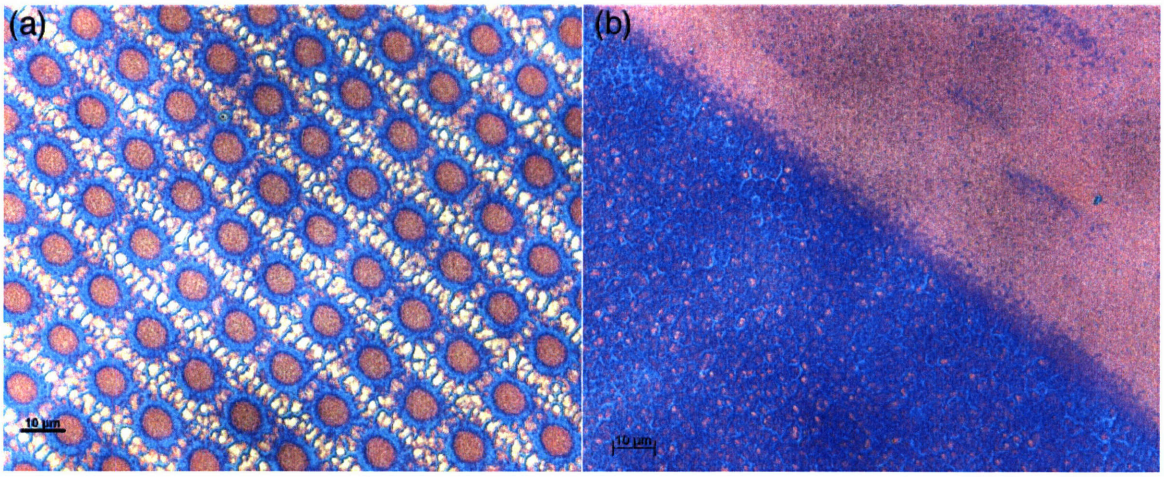

Figure 4.10. Optical microscopy images of patterned (PAH 7.5/TPAArVBA 3.5)$_{20}$ films. (a) 5μm diameter circle negative mask. (b) Half masked film image.

The increase in thickness for the overall film is expected from the porosity transition. When the pattern is not confining, as in the case of a half-masked film (Figure 4.10b), the same porous structure is evident, but without the raised edge separating crosslinked from non-crosslinked regions. In that case, the pore edges run directly into the crosslinked regions of the film and simply shrink in height. This can be seen by the lack of abrupt color change at the edge between the two regions. In all of these cases, the crosslinked regions remain nonporous, while the unexposed regions show the visible lateral microporosity.

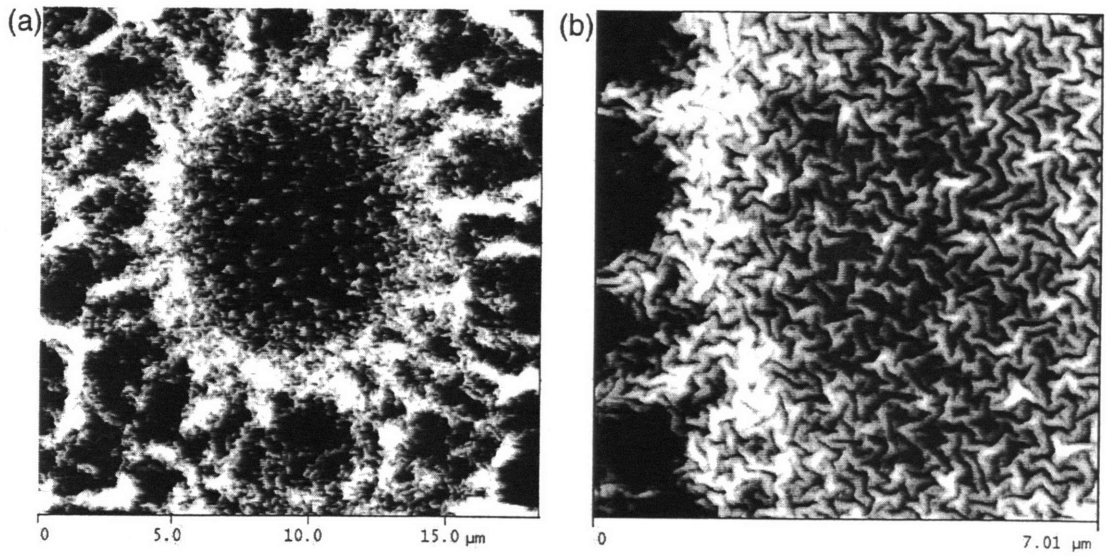

Figure 4.11. AFM of dot-patterned, porous (PAH 7.5/TPAArVBA 3.5)$_{20}$ film showing the raised edge around a crosslinked region of the film. (b) Closer scan shows the crosslinked region maintains the surface topography of the PAArVBA-topped film.

Patterned films constructed of (PAH 8.5/DPAArVBA 3.5)$_{10.5}$ also demonstrate selective porosity. For films built on glass, the difference in thickness can be visualized by a change in the interference color of the film. Shown in Figure 4.12 is a sample film with patterned 40 μm-wide porous lines. The apparent waviness of the lines is actually due to the mask, which was based off of a transparency template. The minimum resolution of this mask was 5-10 μm and as such, features at that scale can demonstrate irregularities. To observe the extent of transformation, the thickness increase was measured with profilometry.

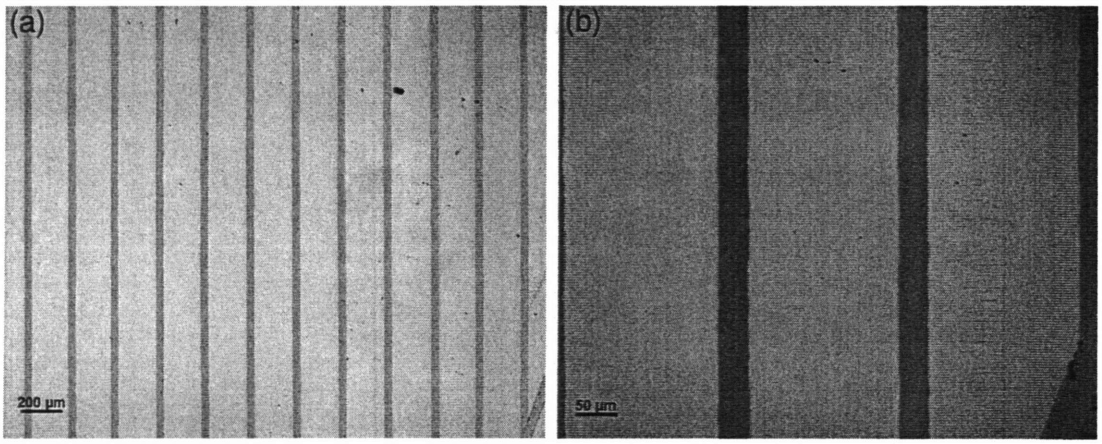

Figure 4.12. Optical microscopy images of patterned nanoporous (PAH 8.5/DPAArVBA 3.5)$_{10.5}$ film at two different magnifications. The deliberate scratch at the lower right was used to measure film depth with profilometry.

A sample profile of a (PAH 8.5/DPAArVBA 3.5)$_{10.5}$ film with a deliberate scratch is shown in Figure 4.13(a), along with a five histograms of film depth taken from different profiles (b). As measured, the thickness is between 155 and 165 nm, consistent with ellipsometric measurements of 154 nm for as-built films. For the nanoporous patterned films, the cross-sections of the lines are apparent as regularly spaced bumps (c). From histogram data of five scans (d), the thickness of the film is between 147 and 152 nm, which is again consistent with previous measurements. The change in thickness for the nanoporous regions is between 21 and 27 nm, which is only 30-50% of what would be expected from ellipsometry data in Figure 4.6.

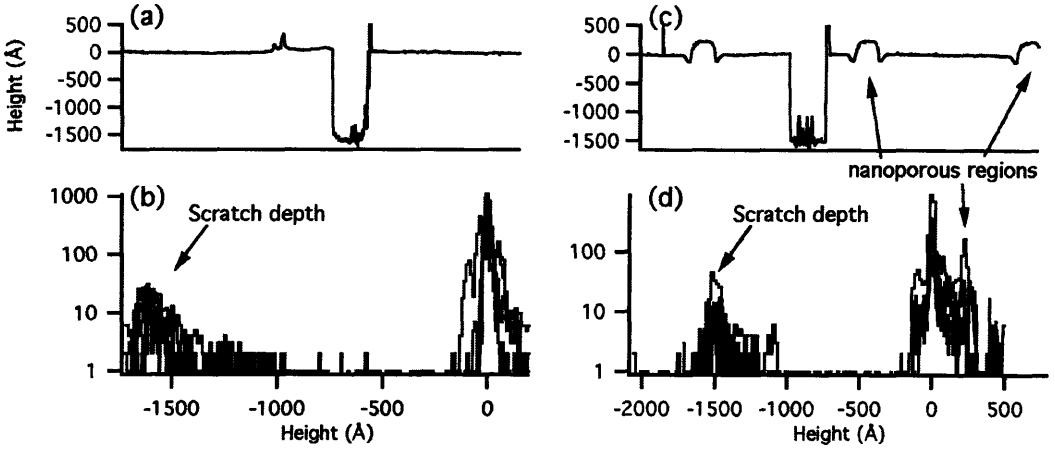

Figure 4.13. Representative profilometry curves for (a) as-built and (c) patterned nanoporous (PAH 8.5/DPAArVBA 3.5)$_{10.5}$ films. Histograms for each type (b,d) show the approximate film thickness through scratch depth and (d) the height of the uncrosslinked porous regions of the films. Note log scale for histogram y-axes.

This discrepancy in nanoporous region thickness could have several causes. It could be attributed to the thermal crosslinking. While the dense portions of the film undergo covalent amide bond formation at elevated temperatures, since they are already dense in the dry state, the change in thickness should be negligible. However the pores in the film are filled with air and as such, will not strongly resist any contraction forces exerted by the film. As the pores shrink, the overall thickness of the film should decrease as compared to the cycled nanoporous films in section 4.2.2. The other possible explanation is that the force exerted by the profilomter tip led to partial collapse of the porous regions. This is supported by the features seen either side of the porous lines. There is a slight dip, suggesting that if that was the beginning of the porosity, that it was slightly collapsed there.

The ability to pattern porosity is promising in that porous structures have interesting optical and physical properties that can be used to build more complicated

structures. The high volume fraction of air in these films significantly lowers their refractive index and also significantly increases their available surface area for molecular adsorption.

Chapter 5. Patterning porosity in heterostructured PAArVBA-containing films

The distributed Bragg reflector or Bragg stack structure consists of alternating layers of material with different refractive indices. Depending on the thickness of each layer, and differences in refractive index, incident light can be reflected at various wavelengths and with varying efficiency [152].

The additive nature of the PEM assembly process makes it an ideal candidate for the creation of these structures by controlling what materials are deposited when. There have been several demonstrations of PEMs constructed specifically to act as Bragg reflectors. Simply layered polyelectrolytes do not tend to have large refractive index (n) contrast, and the interfacial mixing between layers for most systems also acts to prevent the creation of optically distinct alternating layers; thus the creation of a Bragg reflector without additional modification would involve an impractical number of bilayers to create appreciable reflectivity. In order to make reflective films, some processing must be performed on these systems to greatly increase or decrease the refractive index at regularly spaced intervals.

The first PEM Bragg reflectors were achieved through increasing the refractive index of specified layers. Films were made from stacks composed of 77 of bilayers of PAH/SPS alternating with stacks of 24 PAH/PAA bilayers built at low pH [153]. In this case, the interfacial mixing of polyelectrolyte layers of adjacent stacks was negligible compared to the thickness of the stacks. To create a significant refractive index difference, the chemical reactivity of unbound acrylic acid groups on PAA was exploited by immersing the films in Ag^+-containing salt solutions. The Ag^+ ions bound to unpaired

acrylic acid groups in the PAH/PAA stacks of the film and, after reduction in hydrogen gas, formed nanoparticles selectively and uniformly within the PAH/PAA stacks, increasing their effective refractive index. This process was repeated to grow more and larger nanoparticles increasing the refractive index to as high as 2.3. This in turn lead to films with reflectance of near 80% at their maximum for nine stacks [153]. This nanoparticle growth technique along with the z-directional compositional control of PEM assembly was further used to create variation in stack thicknesses to yield more complex 1-D optical structures, such as digital rugate filters that approximate a sinusoidal gradient in refractive index [154].

Alternatively, PEM Bragg reflectors have been generated in an opposing manner by reducing the refractive index of alternating stacks below that of the dense polymer. HPEMs made from PAH/SPS stacks alternating with pH-asymmetric PAH 8.5/PAA 3.5 stacks have been exposed to cycles of low pH and near neutral pH to yield nanoporosity only within the weak polyelectrolyte stacks [79]. These stacks have reduced refractive indices due to their pores being filled with air ($n \approx 1.0$) rather than polymer. Along with the reduction in refractive index, stacks undergoing the nanoporous transition significantly increase in thickness. This must be taken into account when deciding on the number of layers in each stack, as the layer thickness significantly impacts the optical properties.

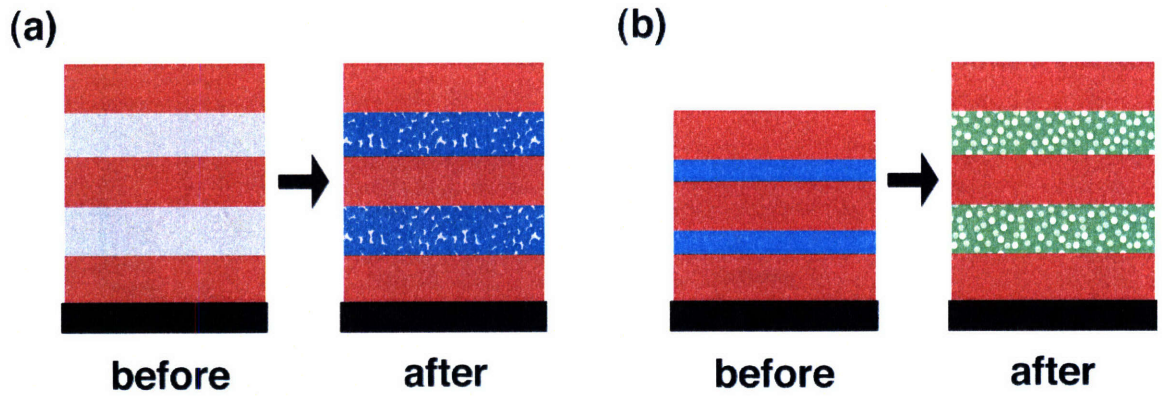

Figure 5.1. Two method of creating refractive index differences in multi-stack films. (a) Selectively filling stacks with silver nanoparticles to increase refractive index. (b) Selectively inducing nanoporosity to decrease refractive index.

The differences between these two HPEM systems are evident in their approach to refractive index variation. However, they are also very similar in that they rely on the alternation of a an "inactive" stack composed at least partially of strong polyelectrolytes alternating with an "active" stack made fully from weak polyelectrolytes. In one case the activity is chemical, promoting the binding and reduction of silver ions, and in the other case the activity is structural, allowing reorganization of polymer chains in the stack to make pores. The incorporation of PAArVBA into the nanoporous HPEM structure will enable the creation of two distinct patternable versions of the active/inactive stack structure.

In the first system (Figure 5.2a) PAArVBA can be substituted for PAA in nanoporous Bragg reflector films to give rise to photo-crosslinking only within the active stacks. As such, the crosslinked regions will not show reflectivity due to inhibition of the nanoporous transition in selected regions of the PAArVBA/PAH stacks. In this case, the lateral pattern is defined by fully dense regions adjacent to regions containing alternating

porous/non-porous stacks. The reflective parts of the film are where the porous layer has created a significant refractive index difference while the fully dense regions remain transparent.

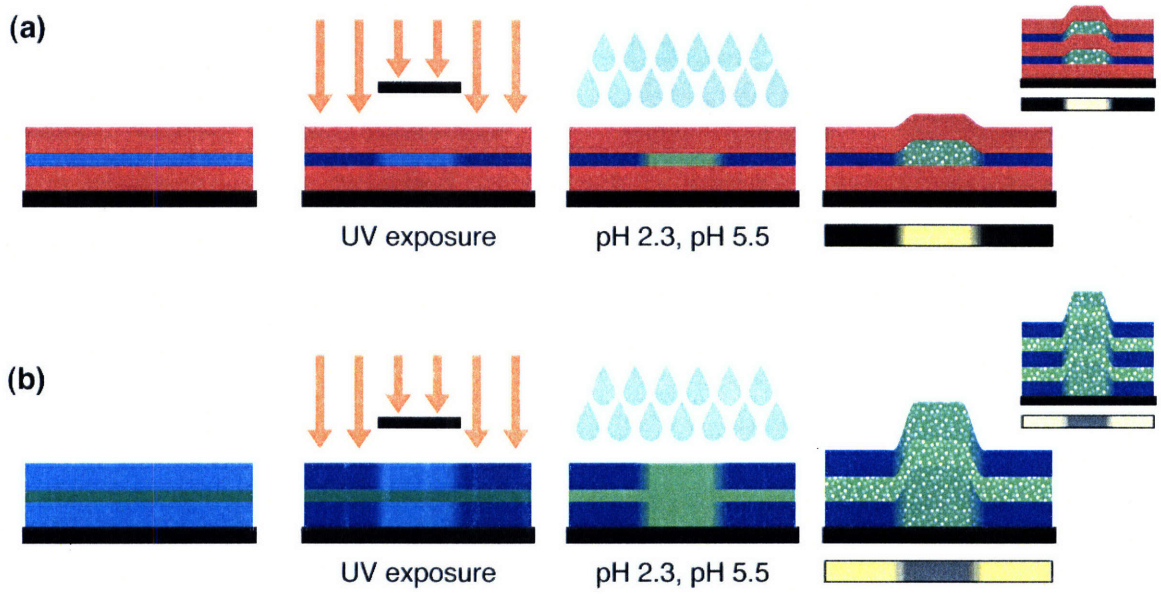

Figure 5.2. Two approaches to making patterned nanoporous Bragg reflectors. (a) Using PAArVBA in the middle stack means that only the masked off regions of the film achieve alternating refractive index differences. Crosslinked regions of the film do not change. (b) Using PAArVBA in the outer stacks means that the UV-exposed regions of the film achieve alternating refractive indices and the whole film changes in thickness.

In the second system, PAArVBA can be substituted for SPS in the "inactive" stack (Figure 5.2b). This assembly changes the overall structure of the system. In this case, the effect of the photo-crosslinking is reversed. Wherever the film is crosslinked, it will have the reflective alternating porous/non-porous-stack structure while uncrosslinked regions of the film will be completely porous rather than completely dense. The completely porous regions of the film will transmit light based on the size of the pores, remaining transparent in the nanopore case and scattering visible light in the micropore case. This system is also notably constructed entirely of weak polyelectrolytes and has

the ability to engage in chemistry using free acrylic acid groups through the entirety of the film.

5.1 Patterned nanoporous Bragg-reflector films incorporating strong and weak polyelectrolytes

5.1.1 Experimental methods

For film construction of PAH/SPS stacks and PAH/PAArVBA stacks, two different solution formulations were used. For PAH/SPS, both polymers were dissolved at 10^{-2} M concentration along with 0.1 M sodium chloride to increase overall film thickness and stability. For PAH/PAArVBA, solutions were made as previously described in section 3.1. All polymer solutions were pH adjusted as described in section 3.1. For this section, DPAArVBA was used.

Stacks were constructed to emulate the structure studied by Zhai et al. [79], with 50 bilayers of (PAH 4.0/SPS 4.0) followed by 5 bilayers (PAH 8.5/PAArVBA 3.5) and finished with 50 bilayers of (PAH 4.0/SPS 4.0). Unlike previous assemblies, deposition of the PAH/SPS stacks was carried out with polymer immersion times of 5 minutes and rinse times of 2, 1, and 1 minutes, in that order. PAH/PAArVBA stacks were built with immersion times of 15 minutes for polymer depositions and 2, 1, and 1 minute rinses. Polymer layers were added continuously for the first stack and the second stack after which a pause in building occurred for up to one hour for changing of solutions, during which time the samples were immersed in DI water. After the change, the final stack was added, or in the case of some samples, another bi-stack followed by another pause and then the final stack. The last stack was in all cases (PAH 4.0/SPS 4.0), so we will refer to assemblies by the number of active stacks or "A-stacks". For example, a one A-stack

film has one stack of PAH/PAArVBA and one stack of PAH/SPS above and below (Figure 5.3a), while a two A-stack film is assembled as $(PAH/SPS)_{50}$-$(PAH/PAArVBA)_5$-$(PAH/SPS)_{50}$-$(PAH/PAArVBA)_5$-$(PAH/SPS)_{50}$ (Figure 5.3b).

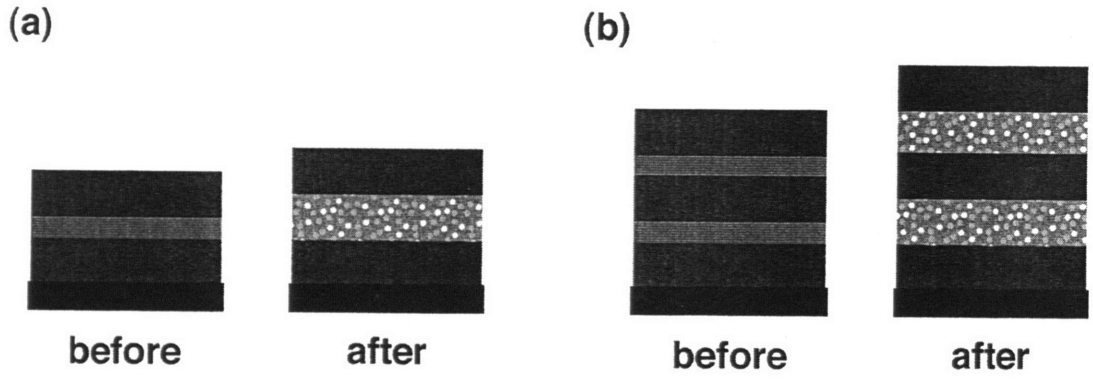

Figure 5.3. Illustration of a (a) one A-stack film and a (b) two A-stack film, before and after nanoporosity. The number refers to the number of low refractive index stacks within the film.

The dipping pattern followed a standard bilayer pattern within each stack, but the interface between stacks was not straightforward. When transitioning from a (PAH/SPS) stack to a (PAH/PAArVBA) stack, the top polymer layer did not make a difference in the quality of the films, but the inverse was not the case. When the salt-containing PAH at pH 4.0 was assembled onto PAArVBA at pH 3.5, the resulting films were cloudy and inhomogeneous, indicating poor adhesion between the stacks. In addition, the PAH solution would become cloudy. The most likely explanation of this phenomenon is that PAArVBA was being pulled off of the multilayer to complex with PAH in solution, resulting in some precipitate and poor binding of the next film layer. While previously the high charge density of PAH at low pH didn't appear to affect assembly, the addition of salt likely decreased the charge-charge interactions within the film, enabling its partial dissolution. In contrast, if the last layer of the weak polyelectrolyte stack was PAH

deposited at pH 8.5, there were no film clarity problems or solution precipitation problems during SPS deposition. This is likely because within the SPS bath at pH 4.0, the PAH on the surface is fully charged.

In order to obtain nanoporosity in the PAH/PAArVBA stacks, assembled films were immersed in aqueous solution of pH 2.3, blown dry, immersed in Milli-Q deionized water (pH 5.5-6), and blown dry with a filtered air stream for several cycles as in section 4.2.1. All films were thermally crosslinked at 180 °C for 4-5 hours after the porosity treatment to create amide bonds between PAH and PAArVBA that preserve the final structure. AFM on films was performed on a Nanoscope D3000 (Veeco) as described in section 4.1.2.

UV-vis specular reflectance measurements were performed using a Cary 500i spectrophotometer (Varian) with the double-bounce absolute specular reflectance accessory at 7 ° incidence normal to the substrate surface. As our samples were typically smaller than the sample window for both bounces in the light path, an aluminum mirror of known reflectivity was used in conjunction with our measurements to act as the reflector for the first bounce (Figure 5.4). This is the setup prescribed by the instrument vendor. All sample substrates were sanded on the backside with a Dremel tool to eliminate non-film-based reflections from the glass.

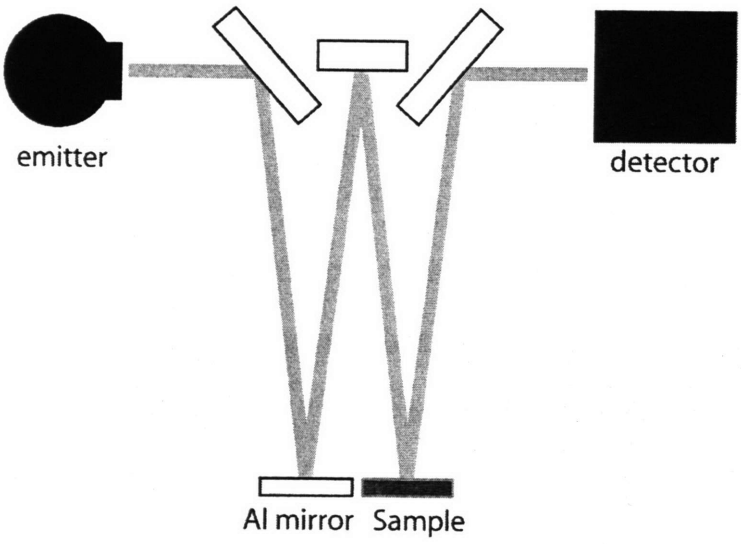

Figure 5.4. Schematic of double bounce specular reflectance accessory beam path.

The complex composition of these films in the z-direction makes it difficult to determine their thickness using ellipsometry, as the changes in refractive index for the porous stacks are initially unknown. That paired with the alternation of dense polymer stacks make profilometry and AFM more straightforward techniques for obtaining film thickness measurements. It should be noted that care must be taken to sample multiple spots on the film surface, as these techniques typically don't cover a large enough areas per spot to guarantee that the thickness is typical of the entire sample. AFM measurements typically don't sample areas larger than 100x100 μm^2 and while profilometry can cover distances on the order of millimeters, it is a one-dimensional measurement. Profilometry was measured on a P10 Surface Profiler (Tencor).

In order to corroborate the film structure, simulations of the reflectivity were generated using experimental data. Using a program developed by Adam Nolte for MATLAB (***) and knowledge of the thickness and refractive indices of each stack, the

reflectivity can be modeled with the transfer matrix method [155]. The specific application of this method to PEM systems is well described in the literature [79, 154]. Briefly, the refractive index and thickness of each homogeneous stack of the multi-stack structure is used to create a 2x2 matrix. The matrices are then multiplied together in order, from top surface to substrate-adjacent surface, to yield a transfer matrix for the total structure. This matrix can then be used to model reflectivity of the structure for a selected range of incident wavelengths of light.

5.1.2 Results and discussion

We can immediately see the effects of UV crosslinking on the reflectivity of a one A-stack film (PAH 4.0/SPS 4.0)$_{50}$-(PAH 8.5/DPAArVBA 3.5)$_{5.5}$-(SPS 4.0/PAH 4.0)$_{50.5}$. Shown in Figure 5.5 is the reflectivity as a function of incident wavelength for a sample film as-built and after 8 porosity treatment cycles. The treated sample was previously UV-crosslinked on one half for 20 minutes and spectra for both regions are shown. The porous region of the film shows a reflectivity peak at 547 nm while the reflectivity of the crosslinked region of the treated film almost superimposes over that of the as-built film. The undulations in the as-built film spectrum are presumed to be due to interference fringes generated by the thickness of the film itself.

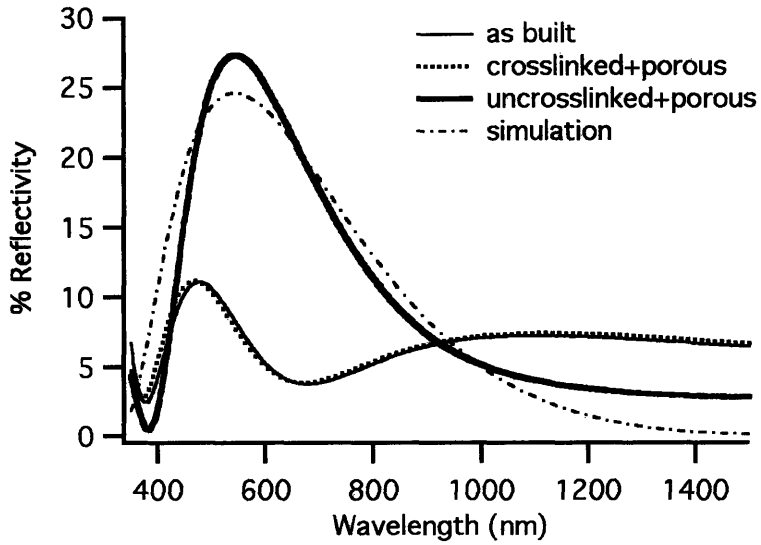

Figure 5.5. Reflectivity spectra of one A-stack $(PAH/SPS)_{50}$-$(PAH/PAArVBA)_{5.5}$-$(SPS/PAH)_{50.5}$ HPEM films for various processing conditions, along with a simulation of the reflectivity spectrum of the porous film.

The lack of change in the crosslinked, treated film is promising, as it supports the spectroscopic ellipsometric measurements of homogeneous (PAH 8.5/DPAArVBA 3.5) films discussed in Section 4.1.2, wherein the short acid immersion caused a thickness transformation in the non-crosslinked films without significantly affecting the crosslinked films. The thicknesses and refractive indices of the PAH/SPS stacks were measured with spectroscopic ellipsometry, while the thickness of the total film both before and after porosity was determined with profilometry.

To find the other relevant physical parameters, several relations were used. Firstly, the wavelength of the first order peak of a Bragg reflector can be related to thickness and refractive index by [156]

$$\lambda_{max} = 2(d_p n_p + d_{np} n_{np}) \quad (5.1)$$

where λ_{max} is the wavelength, d_p and n_p are the thickness and refractive index of the porous regions and d_{np} and n_{np} are the thickness and refractive index of the nonporous regions, respectively. In our case, n_p is the only unknown. In addition we can independently estimate n_p by using a volumetric argument to relate the pore volume to the refractive index. Assuming that the mass of the porous stack is conserved during the transition, the new refractive index will be [157, 158]

$$n_p = f_{air} n_{air} + (1 - f_{air}) n_{np} \quad (5.2)$$

where n_p is the refractive index of the porous stack, f_{air} is the volume fraction of the stack occupied by the pores, and n_{np} is the refractive index of the solid (polymer) portion of the porous stack and n_{air} is the refractive index of the air within the pores ($n_{air} \approx 1$). The volume fraction of the pores is simply $(H-H_0)/H$, where H is the final stack thickness and H_0 is the initial stack thickness. Table 5.1 gives the relevant values determined experimentally that were used to simulate the reflectivity of the porous film along with directly related values and extrapolated values (grey cells).

Simulation accurately captures the behavior of the film using experimentally determined thickness and n values as inputs. The porous stack refractive index n_p in this case from equation (5.1) is 1.085, which is much lower than the original polymer film value of 1.53. In fact, deriving n_p using equation (5.2) and the known H_0 gives a value of 1.36; however this value gives a poor simulation fit to the reflectivity spectrum. Using equation (5.2) with an input value of 1.085 for n_p gives a value of 20.19 nm for H_0,

which does not fit with all other obtained data. A reasonable explanation for the drop in refractive index while staying consistent with the measured thickness change is simply a loss of material from the porous stacks. This is also consistent with measurement of the homogeneous (PAH 8.5/DPAArVBA 3.5) films during the porosity treatment (section 4.2.2). In that case, films in the closed-pore state demonstrated thickness reduction, while maintaining the as-built refractive index, indicating reduced material in the dense state brought about by the porosity transition.

Table 5.1. Experimentally determined, derived and simulated values for one A-stack HPEM films.

	% R at max	λ_{max} (nm)	n_p	H=d_p (nm)	H_0 (nm)	n_{np}	d_{np} (nm)	d_{tot} (nm)
Experimental	27.328	547		133.8	85.3	1.53	83.9	301
Extrapolation from λ_{max}		547	1.085	133.8	85.3	1.53	83.9	301
H_0 defined			1.360	133.8	85.3	1.53	83.9	301
n_{np} defined				133.8	20.2	1.53	83.9	301
From simulation	24.591	544	1.085	133.8		1.53	83.9	301

The reflectivity is also visually apparent in Figure 5.6 with 50 μm wide porous lines patterned in a one A-stack film. As with homogeneous (PAH 8.5/DPAArVBA 3.5) patterned films, the edge between the porous and non-porous regions is not sharp, and in this case is 5-10 μm. This is likely due to the increased overall film thickness, which broadens any abrupt changes in film thickness such as in the case of pattern edges.

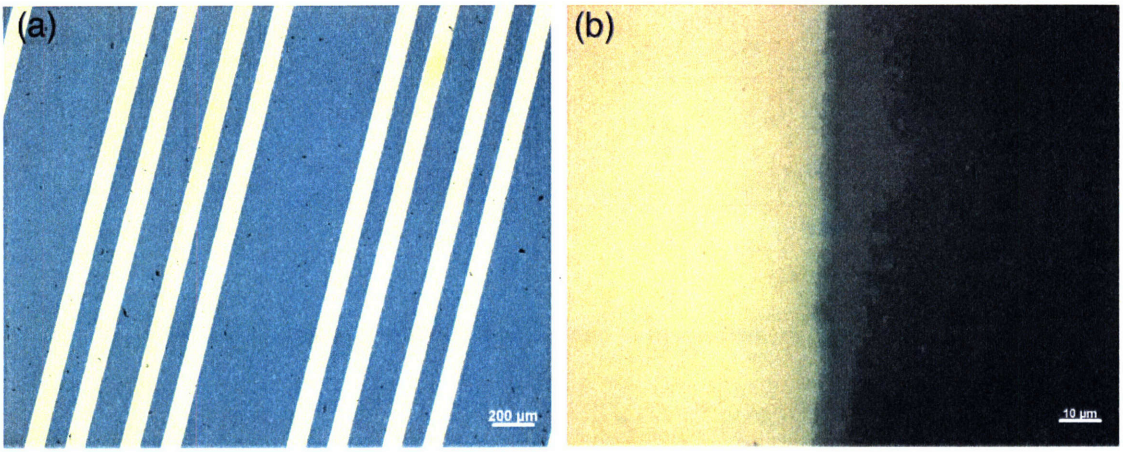

Figure 5.6. Optical microscopy images of a one A-stack film. (a) The porous regions are clearly reflective, while the crosslinked regions of the film have a residual green color, the same as the unprocessed film. (b) The width of the edge region is less than 10 μm.

Profilometry measurements of a patterned film show the overall film thickness as well as the difference in height between crosslinked and non-crosslinked regions after the porosity transition (Figure 5.7). The film thickness for the porous region is clearly increased over that of the crosslinked region. The overall film height was measured by scratching the film with a razor as previously indicated. Total initial film height was 253 nm which, after subtracting the thickness of the two PAH/SPS stacks gives a value of 83.8 nm for the (PAH 8.5/DPAArVBA 3.5)$_{5.5}$ stack, or 15.2 nm per bilayer, This correlates with previous thickness measurements of single composition (PAH 8.5/DPAArVBA 3.5) films (Figure 4.13). The increase in thickness for the porous regions of the film is 49-54 nm from a histogram analysis of the film profiles, which is within 25% of the value of 64 nm measured by Zhai et al. for (PAH 4.0/SPS 4.0)$_{50}$-(PAH 8.5/PAA 3.5)$_{5.5}$-(PAH 4.0/SPS 4.0)$_{50}$ [79].

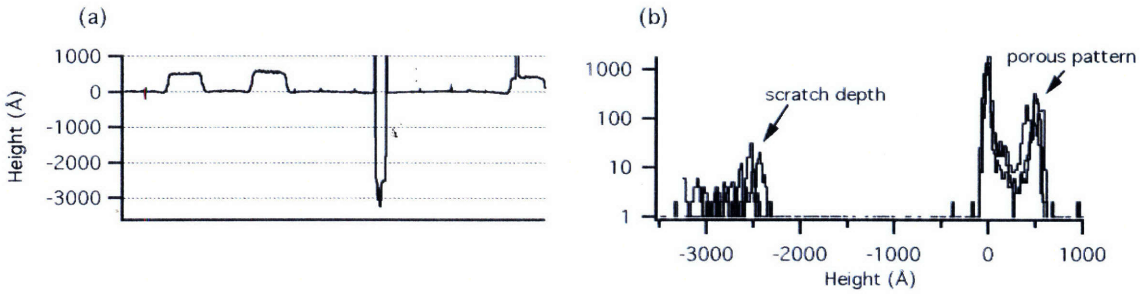

Figure 5.7. (a) Profilometry measurement of one A-stack patterned porous film and (b) histogram of several profiles.

The discrepancy can be explained by the difference in treatment method. In that study, the samples were immersed in pH 2.3 for 1 minute, and then into DI water for 1 minute but not thermally crosslinked. Thermal crosslinking was shown in that same study, but not with that exact layer pattern, to reduce the thickness of porous multilayers.

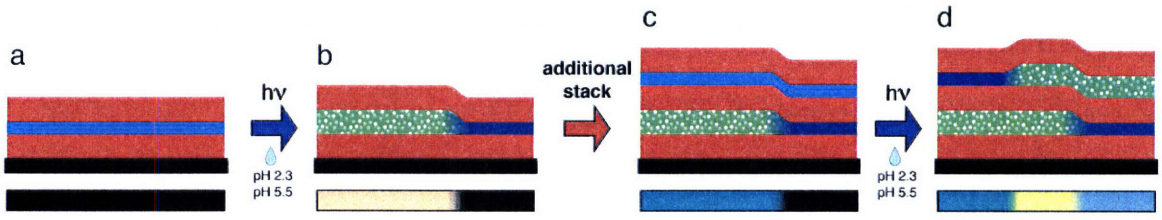

Figure 5.8. Steps to making a dual-patterned film. (a) Building a one A-stack film, (b) patterning and inducing porosity, then thermal crosslinking to preserve the structure; (c) Building an additional structure with another active stack and (d) patterning that structure. Where the two patterns overlap, the reflectivity will be enhanced while maintaining the original pattern.

The additive nature of the PEM assembly process also allows us to create additive patterns in our films. By patterning, and making porous a one A-stack film and thermally crosslinking the whole film to preserve the structure, we can assemble another stack of (PAH 8.5/PAArVBA 3.5) followed by a stack of (PAH 4.0/SPS 4.0) to make a second A-stack (Figure 5.8). We can then pattern this stack in the same manner as the first, giving two distinct patterns that may or may not overlap. The addition of the second A-stack

modifies the reflective spectrum of the first pattern simply through the effective increase in thickness of the top nonporous stack. Where the patterns overlap, the change in reflectivity is due to an increase in the number of repeats of the Bragg stack alternating structure. Visible in a representative sample (Figure 5.9), the two overlapping patterns show different colors in reflection and transmission.

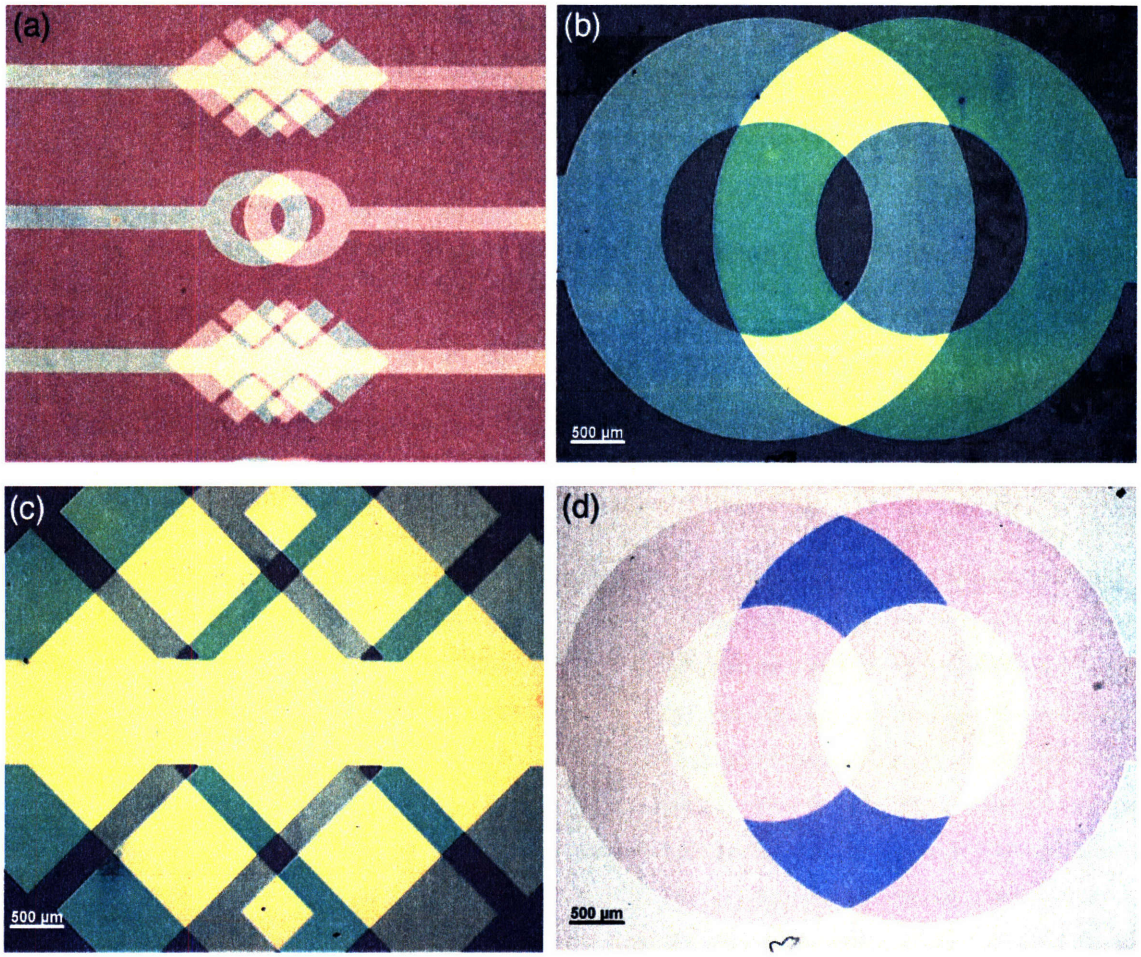

Figure 5.9. A dual stack patterned film. (a, b, c) The two patterns show slightly different reflective colors and where they overlap, the reflectivity is significantly enhanced. (d) The patterns show similar behavior in transmission.

The dual A-stack structure is also evident in profilometry of the patterned film shown below (Figure 5.10). The raised surfaces of the nanoporous regions are evident as

in the one A-stack film. In addition, the overlapping region has a thickness change approximately twice that of the single A-stacks, as expected. The curvature is due to the difficulty for the instrument to maintain a constant baseline over long measurement distances, in this case several millimeters.

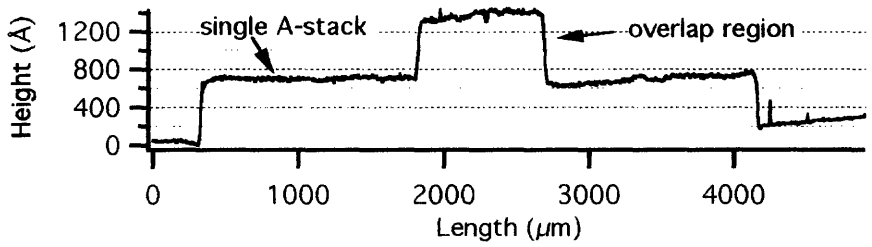

Figure 5.10. Profilometry curve of dual-patterned two A-stack film where the patterns overlap. The height change for two porous stacks is double that of each single porous stack.

The reflectivity of these films correlates with visual appearance. For the singly patterned regions, the λ_{max} are close to each other at 497 nm and 509 nm for the bottom and top patterned layers, respectively. The pattern overlap region shows enhanced reflectivity along with a wavelength shift, which is expected for two A-stack films versus one A-stack films.

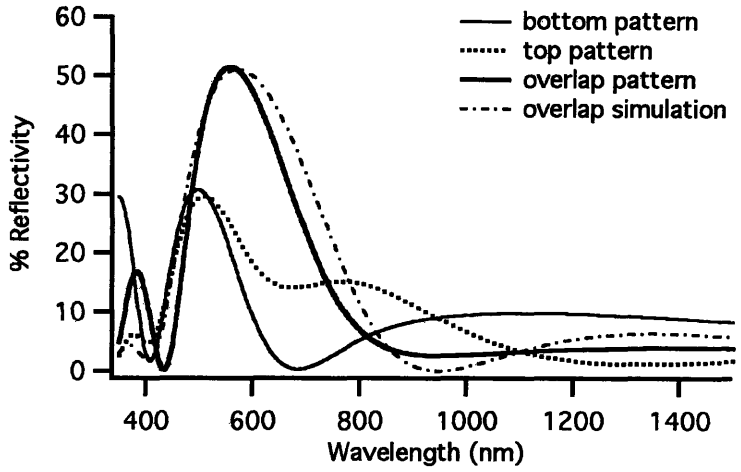

Figure 5.11. Reflectivity spectra for different regions on a dual patterned two A-stack film along with a simulation of the overlap region.

The thicknesses determined from profilometry along with the previously derived refractive indices can be input into the simulation to yield a curve that approaches the experimental result. This suggests that our low value of $n_p = 1.08$ is valid and that the porous stacks are almost completely filled with air (~85%), in part due to material loss.

The additive technique is not restricted to two stacks, but can be easily used to produce more reflective patterns with a further shift in color leading to several colors on the same film depending on the locations of the overlaps. A three A-stack structure could conceivably contain a Fabry-Perot-type structure where the top and bottom A-stack was activated, but the middle stack was crosslinked.

5.2 Patterned nanoporous Bragg-reflector films incorporating only weak polyelectrolytes

5.2.1 Experimental methods

Film construction was carried out in the same manner as described in section 3.1. Solutions of PAH were pH adjusted to 8.5 and solutions of PAArVBA and PAA were pH adjusted to 3.5. TPAArVBA was used for this section. Film thicknesses were measured with profilometry as previously described.[1] Porosity treatments will be discussed in the results section. Reflectance measurements were carried out as previously described (section 5.1.1), except that the backside of glass substrates with films for testing were not sanded down to eliminate direct reflection, though the films were removed from that side with a razor blade. For simulations of the reflectivity, this was taken into account. AFM surface measurements were taken using the Veeco D3000 in tapping mode as described in section 4.1.1.

5.2.2 Results and discussion

There are several differences between this heterostack system and the previously examined one. PAH 8.5/PAArVBA 3.5 and PAH 8.5/PAA 3.5 bilayers deposit more thickly than PAH 4.0/SPS 4.0 due to decreased charge density of the polymers in solution and in the films during adsorption. As our goal is to achieve stack thicknesses that are optically relevant to reflection, it will take fewer bilayers to replace the thickness of 50 bilayers of PAH 4.0/SPS 4.0 in the inactive stacks. In addition, the non-patterned regions of the film, instead of remaining in their initial state after acid and neutral water

---

[1] Profilometry measurements were carried out by Adam Nolte.

treatment, will become porous. For thinner films, this should not be any different from previous (PAH 8.5/PAArVBA 3.5) films, but for films with several stacks, the thickness of the films plays a role in the choice of immersion times.

To assess the ability of PAArVBA to inhibit the porous transformation, films of $[(\text{PAH 8.5/TPAArVBA 3.5})_{10}\text{-}(\text{PAH 8.5/PAA 3.5})_5]_x$ were assembled, where bi-stack number $x = 0.5, 1.5, 2.5, 3.5, 4.5$. Attempting to cycle the thicker films ($x = 2.5, 3.5, 4.5$) for similar times as the previous system (90 s each for acid and DI water immersion) resulted in millimeter-sized bulbous defects forming in the film. These defects, when dried carefully, did not result in film removal, but the edge of the defect was clearly visible due to wrinkling, and when they occurred in regions intended to be reflective, were instead scattering. This suggests that the cause was poor adhesion either between the film and the substrate, or between some layers in the film, rather than a problem through the whole thickness of the film or a problem laterally within layers. The frequency of these defects increased with increasing numbers of cycles, suggesting that the rapid swelling and deswelling was destabilizing the film. To obtain more uniform reflective films required extending the acid and water treatment times to 10 minutes and 20 minutes, respectively, using only one cycle.

Shown in Figure 5.12 is the thickness data for films under various processing conditions. Each data point is the average of three profilometry thickness measurements on single samples. The effect of UV exposure on the porosity transformation is not completely inhibitory as in the PAH/SPS/PAArVBA system, because half of the stacks do not contain PAArVBA and are unaffected by the exposure. There is no data on the porosity treatment for 4.5 bi-stack films because of the difficulty in obtaining defect free

samples, though visually they appeared reflective. The thickness of as-built films increases linearly with bi-stack number as expected for this system, and the thickness increase in the unexposed porous case is linear as well.

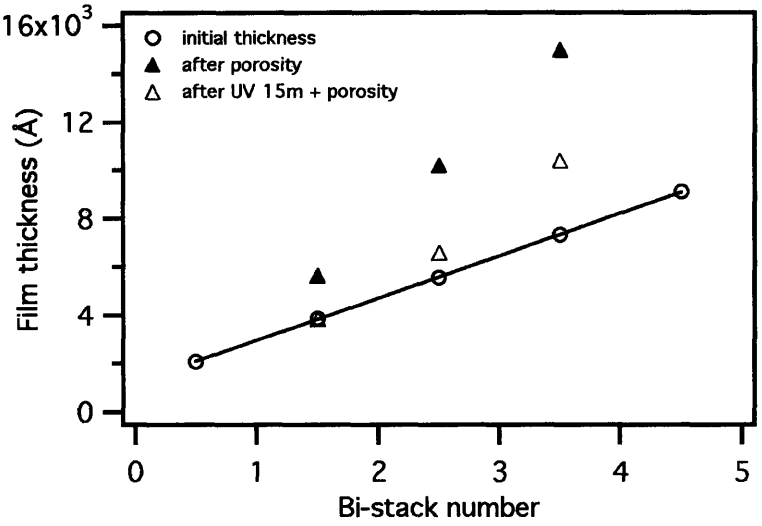

Figure 5.12. Profilometry of $[(PAH\ 8.5/TPAArVBA\ 3.5)_{10}\text{-}(PAH\ 8.5/PAA\ 3.5)_5]_x$ films after different processing treatments, where *x* is bi-stack number.

The reflectivity also increases with stack number as expected (Figure 5.13). UV exposed porous films demonstrate reflectivity as high as 72% at 732 nm for 3.5 bi-stacks. We can compare the reflectivity of the 2.5 bi-stack film to the two A-stack film in the weak/strong PEM system, which has the same number of porous and nonporous blocks. The reflectivity in both cases is near 51%, but there is a significant shift upwards in wavelength of maximum reflectance for the all-weak PEM system from 547 nm to 663 nm.

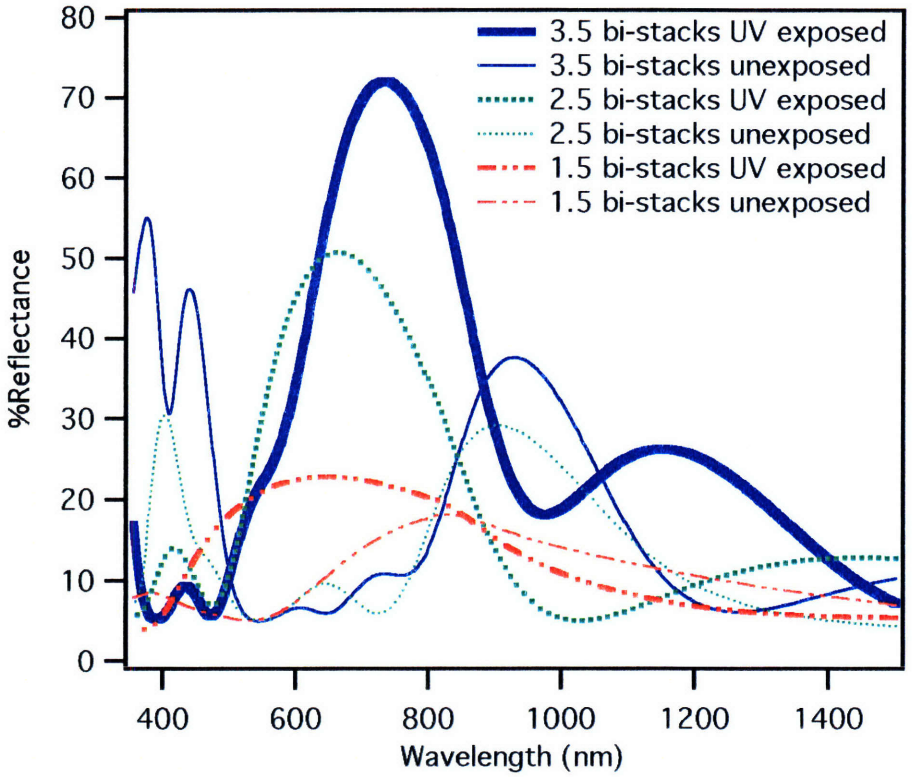

Figure 5.13. Reflectivity for $[(PAH\ 8.5/TPAArVBA\ 3.5)_{10}\text{-}(PAH\ 8.5/PAA\ 3.5)_5]_x$ films after porosity treatment for crosslinked and uncrosslinked films where *x* is bi-stack number.

From equation (5.1) we can assume that the wavelength increase would be the result of a greater thickness in the porous stack, the nonporous stack, or both. From Table 5.2, the difference in film thickness fits with the difference in wavelength.

Table 5.2. Comparison of properties of PAH/SPS-containing and PAH/PAA-containing two A-stack films.

2-porous-stack system	% R_{max}	λ_{max} (nm)	Initial thickness (nm)	Porous thickness (nm)
PAH/SPS/DPAArVBA	51.43	558	373	479
PAH/PAA/TPAArVBA	50.7	663	555.7	660

The unexposed films in this system also exhibit reflectivity, though to a lesser degree than for the crosslinked systems, as seen in Figure 5.13. Our expectation was that a fully porous film would not show any stratification that would lead to reflectivity, but although the unexposed regions of these films scatter light, consistent with a microporous morphology, those regions also display heterogeneous reflection (Figure 5.14). The cause of the reflectivity may be related to the same behavior that we have seen for all pH-asymmetric PAArVBA-containing systems thus far, namely that of material loss from uncrosslinked stacks during the acid/neutral treatment. If material were being lost from those stacks, it could account for the porosity and refractive index differences from adjacent PAH/PAA stacks. The λ_{max} for those film regions is much higher than for the crosslinked regions, presumably due to the 40-50% increase in film thickness.

Figure 5.14. Photograph of patterned porous $[(PAH\ 8.5/TPAArVBA\ 3.5)_{10}$-$(PAH\ 8.5/PAA\ 3.5)_5]_{3.5}$ film.[2] Regions with alternating porous/non-porous stacks show visibly uniform reflection, while fully porous regions show heterogenenous reflection [159].

---

[2] Photograph taken by Felice Frankel

Other evidence for the inhibition of pore formation by PAArVBA can be seen by AFM imaging of the film surface. Shown in Figure 5.15 are representative surfaces of a 4.5 bi-stack film in noncrosslinked (a) and crosslinked (b) regions. Region (a) clearly shows open pores several hundred nanometers in diameter, consistent with the visual scattering. Region (b) by contrast is relatively uniform and pore-free. This morphological difference was the same throughout the two regions of the film, though in some areas of the crosslinked region, mild depressions could be discerned, suggesting the top stack was collapsing into a sub-surface porous region. As the sub-surface is composed of PAH/PAA, the formation of pores is to be expected regardless of the structural state of the stack above. There were, however no open pores found by AFM.

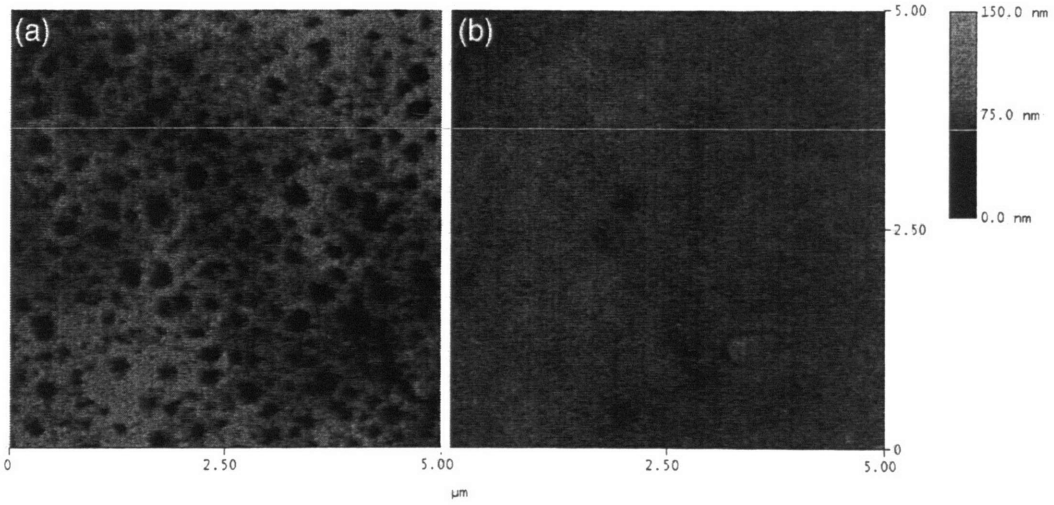

Figure 5.15. AFM of (a) uncrosslinked and (b) crosslinked regions of a patterned [(PAH 8.5/TPAArVBA 3.5)$_{10}$-(PAH 8.5/PAA 3.5)$_5$]$_{3.5}$ film. Images are 5x5 μm^2, height color bar is 150 nm.

Crosslinked film reflectivity was simulated using thickness inputs from profilometry measurements of processed films.[3] It is important to note that the first stack of PAH 8.5/TPAArVBA was much thicker than any of the bi-stacks that were later added and this was reflected in the model, where all other stacks of the same composition were set to the same thickness. Shown in Figure 5.16 are the reflectivity measurements for 1.5, 2.5, and 3.5 bi-stacks and associated simulations. Keeping mass conservation and simulating the porous stack parameters through volume changes can accurately capture the shapes of the reflectivity curves, but fails to capture the intensity. For the 3.5 bi-stack film, we can see that lowering the refractive index to 1.09 assuming material loss gives an accurate wavelength and intensity for the maximum reflectivity peak.

---

[3] Simulation performed by Adam Nolte

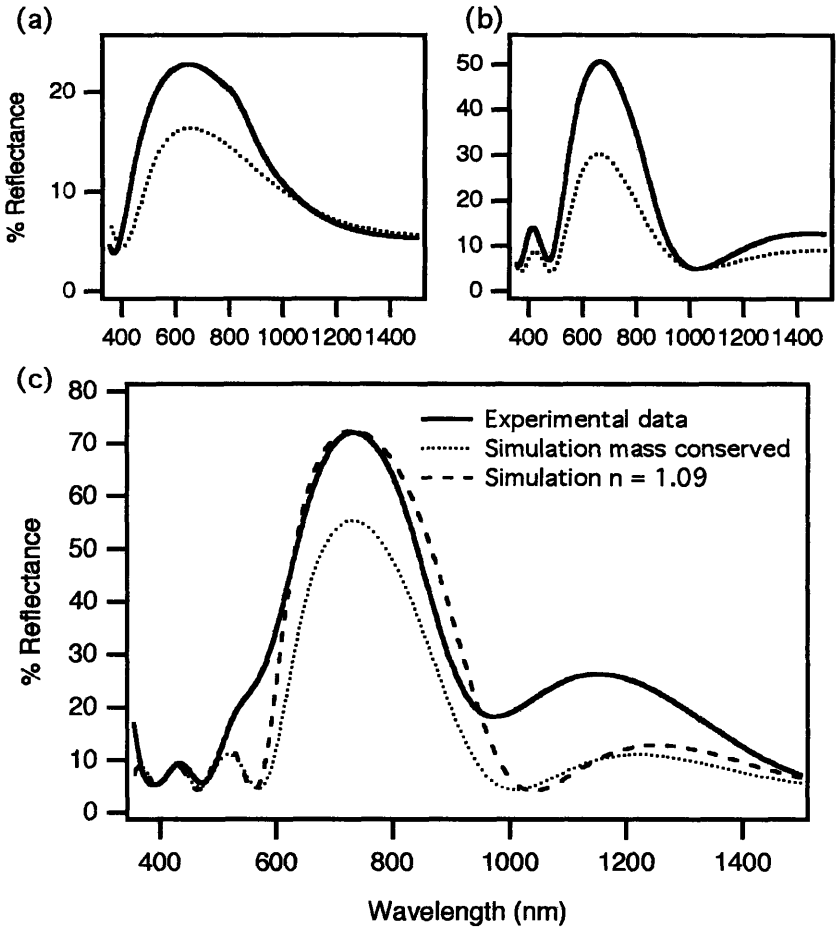

Figure 5.16. Reflectivity spectra and simulations for $[(\text{PAH 8.5/TPAArVBA 3.5})_{10}\text{-}(\text{PAH 8.5/PAA 3.5})_5]_x$ films where x = (a) 1.5, (b) 2.5, (c) 3.5. In the x=3.5 case, simulations using n where mass is conserved and n set to 1.09 are shown.

Chapter 6. Adsorption of guest molecules in PAArVBA-containing pH-asymmetric films

As many PEM systems can be considered as a type of thin film hydrogel, there has been a great deal of interest in utilizing them as carriers for therapeutic drugs and biological molecules such as peptides, proteins, and DNA. As such, we are interested in the potential of our systems to entrap different types of small molecules for use in release or as sensing elements. Using dyes to monitor adsorption will provide a facile method for gauging the effectiveness of our patterning methods.

As a model protein, albumin has been well studied in the cases of assembly or adsorption within multilayers [137, 138], mostly in systems incorporating strong polyelectrolytes such as SPS. Albumin suits our purposes for determining whether location and degree of guest molecule adsorption can be controlled in PEM films by UV-crosslinking and application of porosity.

6.1 Small molecule adsorption

6.1.1 Experimental methods

Methylene blue, fluorescein sodium salt, rhodamine B, propidium iodide (PI), 1,8-diaminonaphthalanene (DAN), and 7-amino-4-methyl-3-coumarinylacetic acid (AMCA) were obtained from Fluka. Dyes were dissolved at 1mg/ml in either water pH 7.0 for adsorption, phosphate buffered saline pH 7.4 (PBS) for adsorption, or dimethyl sulfoxide (DMSO) for adsorption and for capillary loading. Samples used for adsorption were immersed in dye solution for a fixed amount of time. When being removed from dye-containing water solution, samples were rinsed briefly (5 s) with deionized Milli-Q

water (Millipore) to remove loosely bound dye and blown dry. PBS solution-immersed samples were rinsed briefly in fresh PBS, and then blown dry. DMSO-solution immersed samples were rinsed for 1 minute in deionized water and blown dry. The experimental setup for capillary loading will be discussed in the next section.

Samples were examined with fluorescence microscopy using a Zeiss Axioskop2 microscope and band pass filter sets for blue, green and red light. The sets allow excitation wavelengths of 353-377, 450-490, and 534-558 nm and allow viewing of all transmitted light above 397, 515, and 590 nm for the blue, green, and red sets respectively.

(PAH 8.5/PAArVBA 3.5)$_{10.5}$ films were assembled and patterned in the same manner as described in section 4.3.1. (PAH 4.0/SPS 4.0)$_{50}$-(PAH 8.5/PAArVBA 3.5)$_{5.5}$-(SPS 4.0/PAH 4.0)$_{50}$ were assembled as in section 5.1.1.

6.1.2 Results and discussion

To assess the ability to selectively adsorb small molecules to porous regions of PEM films, we looked at patterned films in four processing states. The first was simply UV-exposed films that were patterned to present two states (UV-exposed versus unexposed) in close proximity for optical examination. The second was UV-patterned films that were cycled through the porous transition and then thermally crosslinked, again presenting two processing states (porous versus nonporous) in close proximity.

Previous studies of (PAH 8.5/PAA 3.5) porous films suggested that the porous regions possess excess negative charge [78] and thus, they should strongly adsorb positively charged molecules. To assess this behavior in our system, we examined adsorption of the cationic dye methylene blue (MB) to films that were UV patterned over

the whole film, and cycled through the porous transition on half of the film. Figure 6.1 shows two samples after immersion in methylene blue solution for 2 hours. As can be seen, the top half of both films shows no evidence of dye present, likely due to the PAH top layer of the films tested, which resists cationic dye loading. The bottom half of both films is porous in a dot pattern as can be seen in the light reflection (b), but the thermally crosslinked film shows no visible dye uptake (a). This suggests that the anionic porous regions are being chemically transformed by the thermal crosslinking. To test whether the pores were capable of adsorbing any dye, we placed the thermally crosslinked film into dye solution for longer times (48 hours) and saw evidence of small amounts of dye uptake, though still far below that for non-thermally crosslinked films. This is shown in the UV-vis spectrum of samples before and after thermal crosslinking (c). The maximum peak adsorption wavelength for methylene blue changes depending on the association state. The spectrum for the noncrosslinked porous film denotes dimers or higher order aggregates (peak below 600 nm), while the spectrum for the thermally crosslinked porous film denotes dimers (607 nm) and monomers (664 nm), which fits with the reduced affinity.

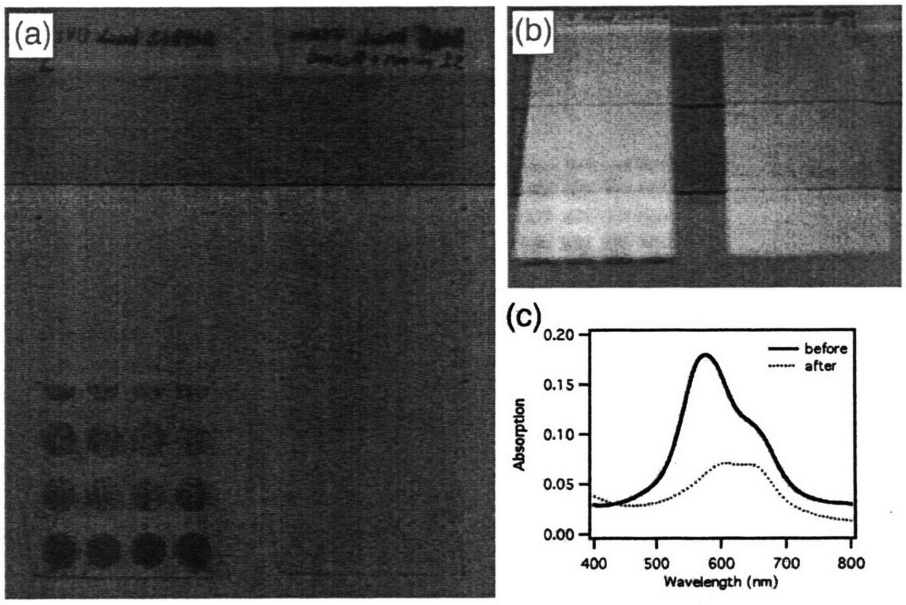

Figure 6.1. Methylene blue (MB) adsorption to UV patterned porous (PAH 8.5/DPAArVBA 3.5)$_{10.5}$ films. (a) The right-hand side film was thermally crosslinked and the porosity was induced only on the bottom half of both films. (b) The reflective dot pattern for the porosity can be seen in both films. (c) The adsorption spectra of MB in the films before and after thermal crosslinking.

Previous studies of low-water-solubility drug adsorption and release in (PAH 8.5/PAA 3.5) films found a significant difference between the level of uptake in porous versus nonporous films. With the present system, the difference can be visualized and directly compared with the changes in adsorption. To understand better what effects the pore wall charge has on the adsorption, we examined several fluorescent dyes with charges of different sign and value (Figure 6.2).

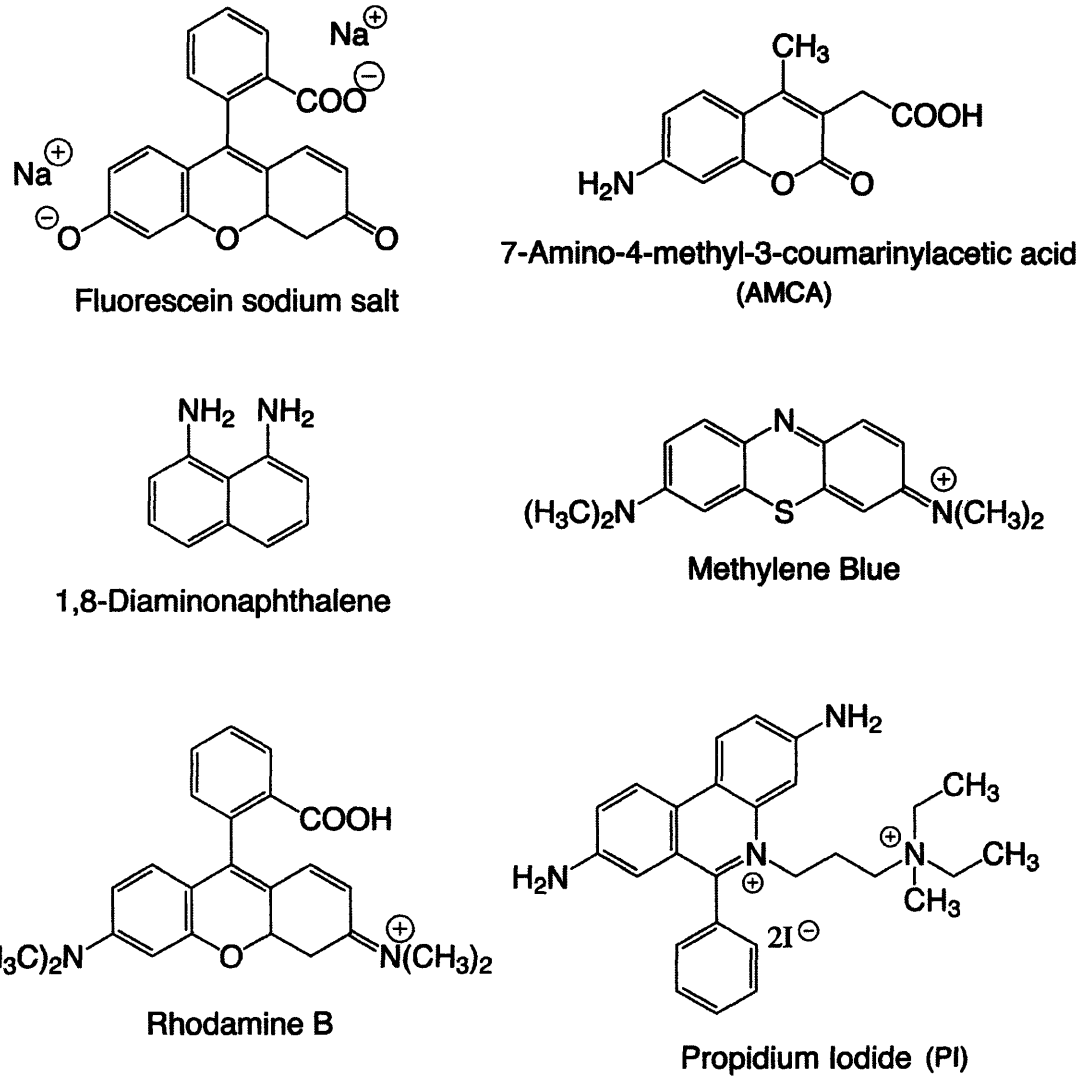

Figure 6.2. Chemical structures of dye molecules used in adsorption experiments.

Looking at UV patterned non-porous films after immersion into PBS solutions of fluorescein, rhodamine B, AMCA and PI for one hour reveals that the response depends strongly on the dye type. Figure 6.3 shows representative images of the patterned samples along with histograms of the image pixel intensities. The comparison between films adsorbing the same dye used the same exposure time for the images. Within the histograms, the lower curves denote the UV-patterned films and the upper, the patterned-porous films. Peaks denoted with a "b" are attributed to the background fluorescence,

which comes from the color channels not associated with the dye being observed. The crosslinked regions are denoted by a "1" and the uncrosslinked by a "2", except where there is no differentiation, in which case the single peak is denoted by a "1".

The dye that shows the highest selectivity between crosslinked and noncrosslinked regions of the film is (b) rhodamine B, which is zwitterionic at pH 7.4, while the sample that exhibits the least differentiation is fluorescein which has a double negative charge and the same general structure. As these films are topped with PAH, there should not be any surface barrier to fluorescein uptake and this is borne out by the higher overall adsorption to the nonporous film versus the porous film (a1 vs. a1'). Propidium iodide, which has a double positive charge, also exhibits a weak preference for the unexposed regions of the UV-crosslinked film, along with zwitterionic AMCA.

All of the dyes show higher differential in the uptake between crosslinked and noncrosslinked regions in the porous-patterned films, evidenced by the better separation between peaks in the histogram, except for AMCA, which shows reduced differential as compared to the nonporous case. The highest increase in selectivity comes from propidium iodide, which is also the most hydrophobic of the four dyes. AMCA is the least hydrophobic of all of the test dyes and this suggests that hydrophobicity plays a role in uptake into the pores. PI is the only dye that shows an overall increase in uptake for the porous vs. the non-porous case.

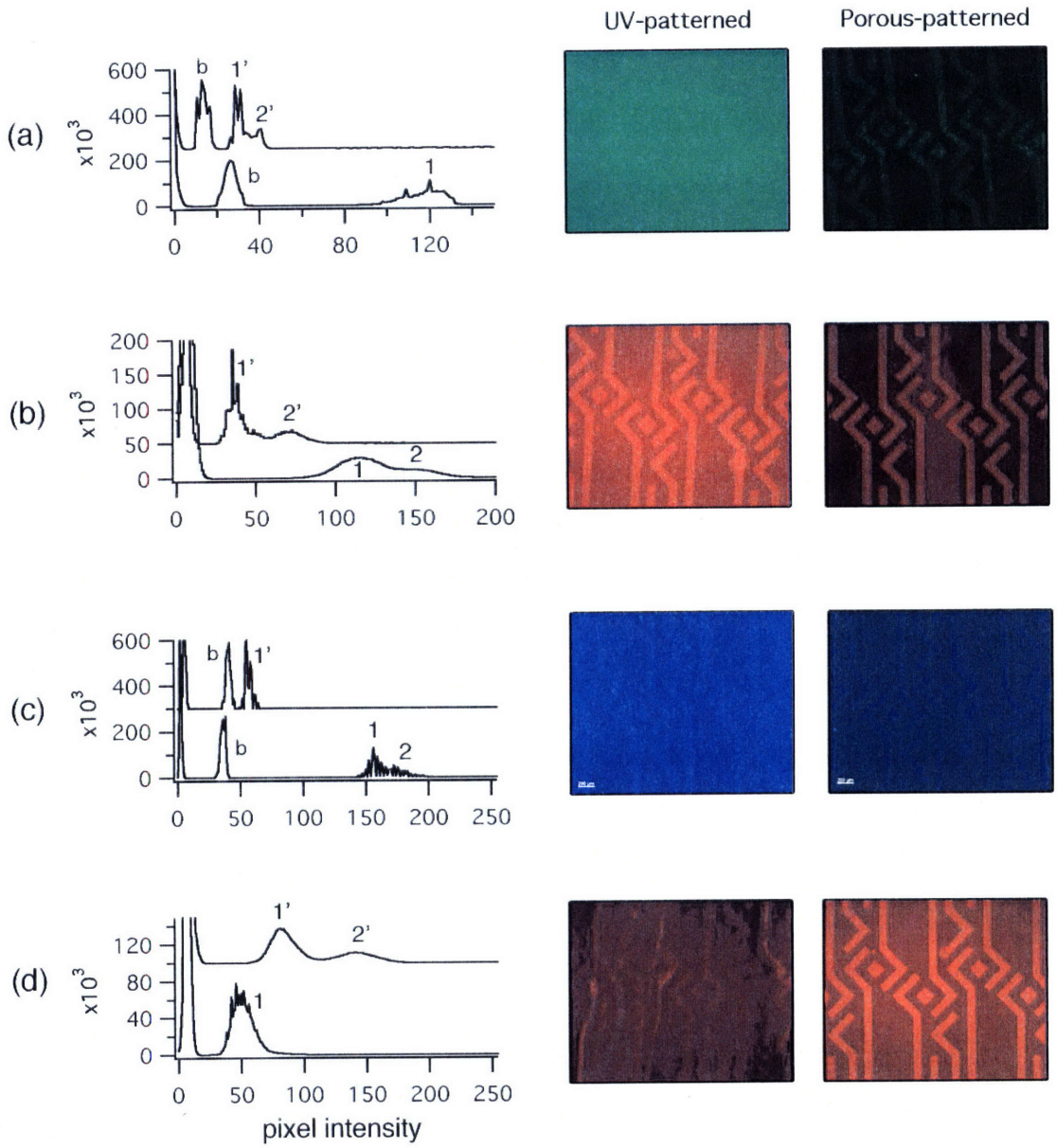

Figure 6.3. Optical images and pixel intensity histograms for UV-patterned (lower curve) and porous-patterned (upper curve) films after immersion in (a) fluorescein, (b) rhodamine B, (c) AMCA, and (d) propidium iodide. On the histograms, background fluorescence is denoted with "b" while the crosslinked and noncrosslinked region peaks are denoted with "1" and "2", respectively.

6.1.3 Capillary wicking into heterostack PEM films

As has been observed previously, (PAH 4.0/SPS 4.0)-(PAH 8.5/PAA 3.5)-(PAH 4.0/SPS 4.0) porous heterostack films have exhibited capillarity in the presence of DMSO, allowing loading of small molecules through wicking [80]. The wicking process

in that case was visualized by the change in refractive index of the one A-stack Bragg reflector when loaded with DMSO. In the nonporous state, the wicking could not be visualized, but measurement of dye content indicated poor or nonexistent loading. The question that is raised by that study is the mechanism of loading inhibition. There are two likely scenarios; if the DMSO were prevented from wicking into the nonporous film, then the dye would also not enter the film. However, it is also possible that the DMSO wicked into the film along with the dye, but there was not a strong interaction between the dye and the film so the dye was quickly removed upon rinsing. Using PAArVBA to pattern channels in the film should let us see if there is loading of dye into the nonporous film regions or not. If there is not, then we would be able to selectively load molecules within the film through different channels (Figure 6.4). In this way, incompatible molecules or molecules with a high reactivity to each other could be isolated on the same surface for later release and interaction.

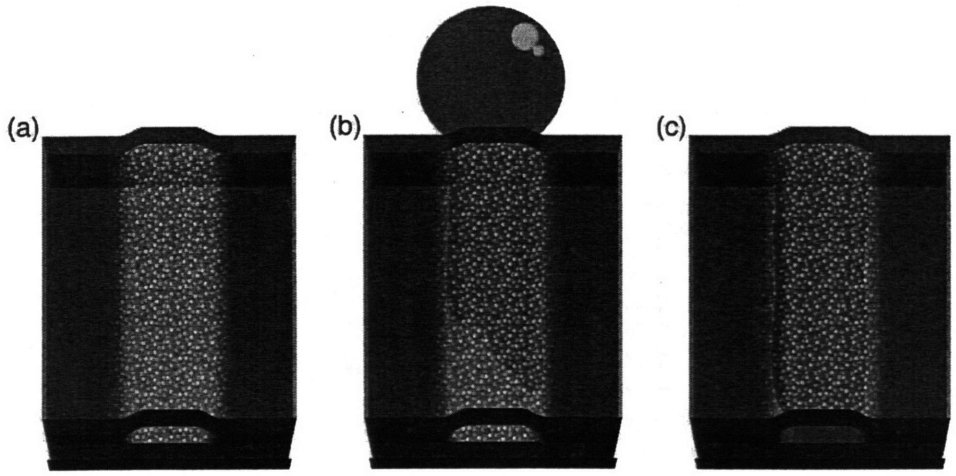

Figure 6.4. Loading of a dye into capillary channels using DMSO. (a) The unloaded patterned porous one A-stack film. (b) Placing dye solution at the edge of the substrate allows wicking into the channels leaving (c) a dye-loaded channel.

Using the (PAH 4.0/SPS 4.0)$_{50}$-(PAH 8.5/DPAArVBA 3.5)$_{5.5}$-(SPS 4.0/PAH 4.0)$_{50.5}$ system, porous channels were patterned onto samples with ends on the edges of the sample. In order to create a reservoir for wicking, the samples were placed channel-side down on their edges onto protruding glass slide edges (Figure 6.5). Droplets of dye loaded-DMSO were placed on the ends of samples to create a meniscus on the channel side of the film allowing wicking. For loading of two dyes, a second droplet was placed on the opposite side of the sample. In order to insure that loading occurred completely, it was necessary to lower the local humidity near the sample, as DMSO is hygroscopic and exhibits inconsistent wicking in the presence of too much water. To accomplish this, a drop of pure DMSO was placed below, but not in contact with, the samples to act as a water vapor trap. Performing the experiments at times of low environmental humidity also led to successful loading, but the droplet approach is more controllable.

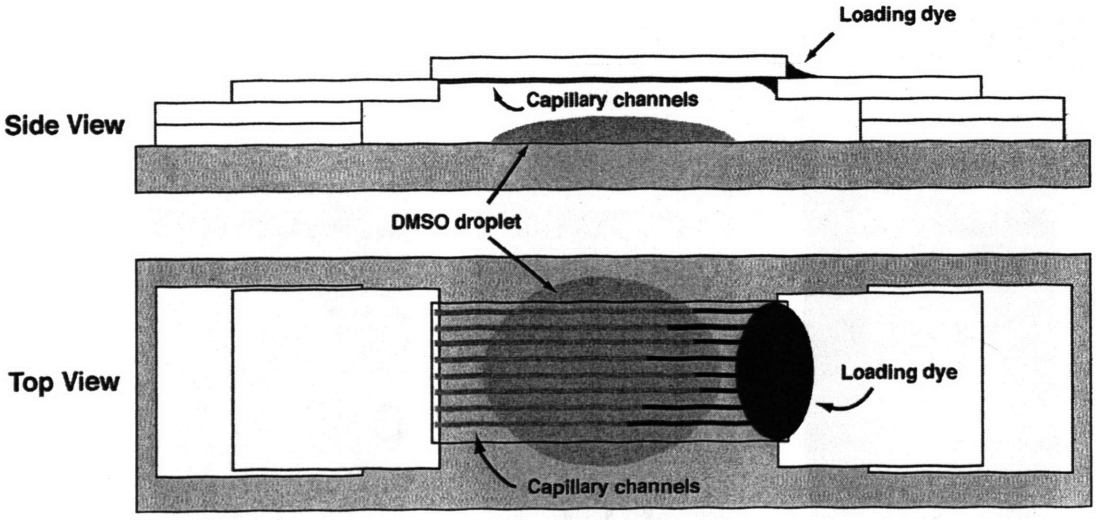

Figure 6.5. Experimental setup for dye loading. Samples were placed channel-side down suspended with glass supports over a droplet of dry DMSO. Dye-loaded DMSO solution was placed at the edge of one or both slides and allowed to wick down the channels.

Figure 6.6 shows fluorescence images of a representative film loaded with rhodamine B and fluorescein from opposite ends of the film. The pattern is designed such that the channels from the two sides of the film are not connected and there are porous diamond shapes in the center of the film isolated from both sides. Through this we can see that though the channels interdigitate, the dyes do not travel between channels and intermix. In addition, the central diamond remains free from dye, confirming the necessity for a connecting porous path for dye transport. Typical of all samples tested, there were inevitably one or two channels unfilled for every ten to fifteen filled channels. This is likely due to a lack of percolation of the porous network in the channel, preventing wicking of DMSO. When films with wicked rhodamine B were immersed in solution, adsorption took place in all porous regions similar to that in Figure 6.3, even for previously unfilled channels, showing that percolation was preventing channel filling. Of note is the visibly weaker adsorption of fluorescein as compared to rhodamine B. This is in agreement with the previous adsorption experiment that showed that the zwitterionic dye adsorbed overall better than the fully negatively charged one.

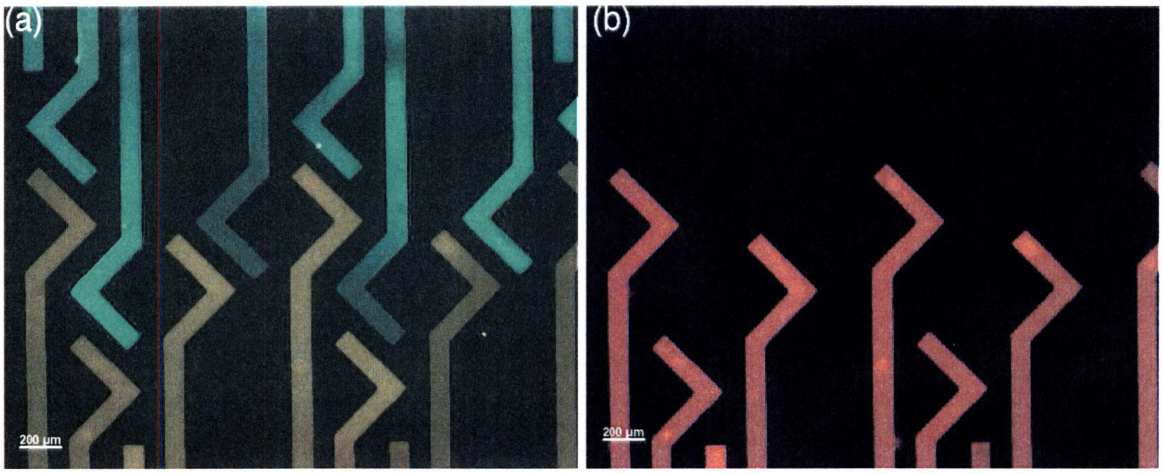

Figure 6.6. Fluorescence microscopy of simultaneous capillary wicking of fluorescein and rhodamine B into one A-stack HPEM films. (a) Imaged using green fluorescent filter that allows red fluorescence through. (b) Imaged using red fluorescent filter that cuts off all green fluorescence.

6.2 Albumin adsorption and release

6.2.1 Experimental methods

For radiolabeled protein adsorption and desorption experiments, iodine-125-coupled BSA (^{125}I-BSA) was synthesized [4] and dissolved at 1mg/ml and 0.2mg/ml in 1xPBS (PBS contains 137 mM/L NaCl, 2.7 mM/L KCl, and 10 mM/L phosphate buffer). In order to obtain quantitative measures of the surface adsorption density of protein, PEM samples were built onto 8 mm and 12 mm diameter coverslips by adhering them to glass slides with silicone on one side. This allowed for the assembly of films on a pristine surface of known area. Some experiments used films made from TEA-catalyzed PAArVBA and others used DBU-catalyzed PAArVBA (see section 2.3). Where each was used will be noted in the results and discussion section. For adsorption experiments the

---

[4] ^{125}I-BSA synthesized by William Kuhlman.

coverslips were placed film side down onto a 10 μL droplet of protein solution. The droplet covered the whole film surface but did not spill over the edges of the sample. Samples were left to adsorb protein and then removed at regular time intervals from the droplet and rinsed 3 times for 30 s each in PBS to remove loosely bound protein. Five samples for each data point were then placed into a scintillation vial for gamma counting using a Cobra II Auto-gamma counter (Perkin Elmer, Inc.) with 20 μL quantities of protein used as a comparison standard. For desorption measurements, samples with protein previously adsorbed were placed into 10 mL each of 1xPBS solution. Samples were removed at fixed times and measured using the gamma counter and then placed back into solution. All radiolabeled protein work was carried out in the laboratory of Professor Linda Griffith.

For patterned adsorption experiments, fluorescein isothiocyante-labeled bovine serum albumin was received from Sigma and dissolved in 1xPBS at a concentration of 1 mg/mL and 2 mg/mL. (PAH 8.5/PAArVBA 3.5) and (PAH 4.0/SPS 4.0)$_{50}$-(PAH 8.5/PAArVBA 3.5)$_{5.5}$-(SPS 4.0/PAH 4.0)$_{50.5}$ films were prepared as in section 4.2.1 and section 5.1.1 respectively. To test adsorption, samples were immersed in protein solution for varying lengths of time, then removed and rinsed briefly in PBS, and finally blown dry. Samples were then imaged using the fluorescence microscope.

6.2.2 Results and discussion

BSA adsorption vs. film thickness measurements for (PAH 8.5/TPAArVBA 3.5) films are shown for 24-hour immersion times (Figure 6.7) at 1mg/mL concentration. The BSA content can be seen to increase linearly with the bilayer number and this suggests that BSA is entering into the films rather than forming adsorbed layers only on the

surface, for which a flat slope would be expected. The strong polyelectrolyte system used for the outside stacks of the Bragg reflectors by contrast shows essentially monolayer adsorption and very little thickness change with layer number, though that is also partially because of the small change in film thickness per bilayer (~1.6 nm). When plotted against estimated dry film thickness, the low protein content in the (PAH 4.0/SPS 4.0) films matches well with that of the (PAH 8.5/TPAArVBA 3.5) films (Figure 6.7b).

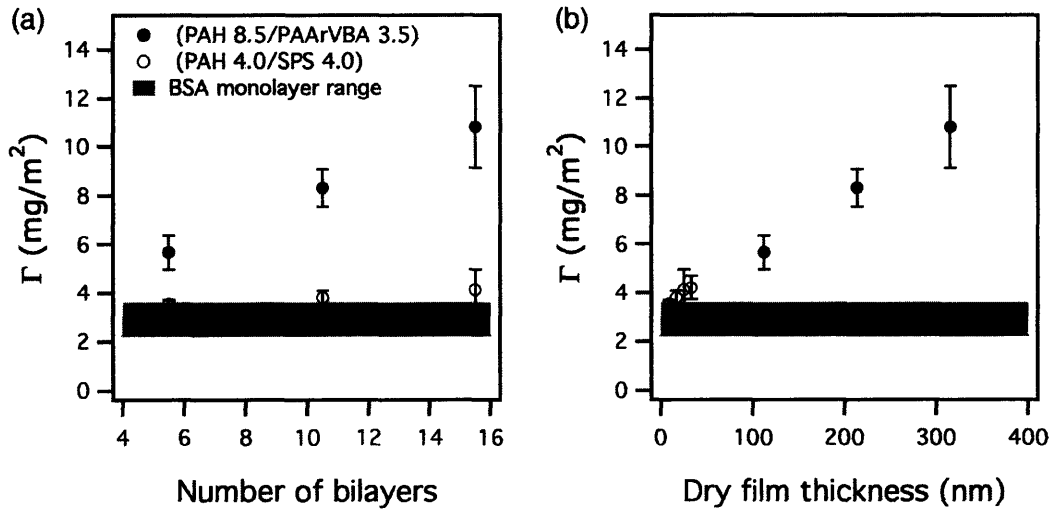

Figure 6.7. Protein content of PEM films as measured by gamma radiation from ^{125}I-labeled bovine albumin as a function of number of bilayers. (PAH 8.5/TPAArVBA 3.5) shows linear increase in adsorption with bilayer number consistent with bulk film uptake rather than surface adsorption. The grey bar indicates the upper and lower bounds for monolayer BSA adsorption based on close packing in end-on and side-on configurations.

We examined the adsorption behavior of (PAH 8.5/PAArVBA 3.5)$_{10.5}$ films, as a function of several processing conditions including porosity, thermal crosslinking and UV crosslinking, and combinations of the three. TPAArVBA was used. In this case, porosity was induced by 5 cycles of 15 s in pH 2.3 and 90 s in DI water, which was the procedure that gave porosity in the uncrosslinked films, while maintaining the dense state in crosslinked TPAArVBA-containing films. As shown (Figure 6.8), the highest BSA

content comes from the porous films after thermal crosslinking, while everything else besides the as-built films shows protein content at or close to monolayer adsorption (2-4 mg/m^2). We can compare this behavior to adsorption in the small molecule case. None of the dye adsorption trends fit that of albumin exactly. PI exhibits the same increase in uptake for the porous, thermally crosslinked vs. non-porous case, but unlike albumin has a higher uptake for the non-porous thermally crosslinked case than the as-built case (Figure 6.3d). None of the other dyes exhibit similar adsorption trends. Regardless, the high differential between thermally crosslinked porous and non-porous conditions provides an opportunity for patterning of adsorption as these two states can be achieved on the same film using our system.

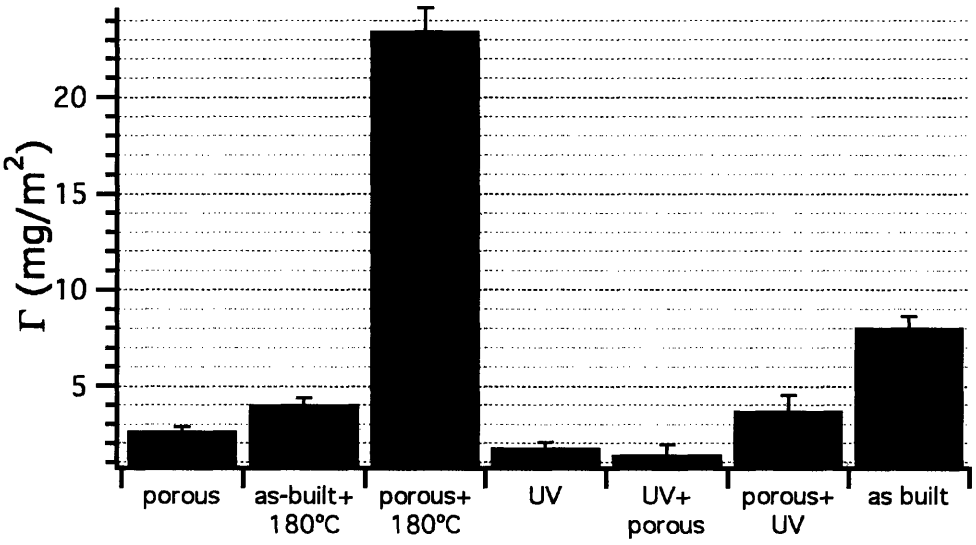

Figure 6.8. Albumin adsorption for (PAH 8.5/PAArVBA 3.5)$_{10.5}$ films after various treatments and 24 hr. protein solution immersion.

Using DPAArVBA-containing (PAH 8.5/PAArVBA 3.5)$_{10.5}$ films, we also examined the time dependent adsorption and desorption of BSA for four film types; as-built, UV exposed, porous and thermally crosslinked and UV-exposed, porous, and thermally crosslinked. Again the porous, thermally crosslinked films show greater adsorption than films made with other processing conditions, though not as much as for the TEA-catalyzed polymer. The difference may be linked to the porosity treatment. The same porosity treatment was used for the DPAArVBA-containing films as used previously for the TPAArVBA-containing films. As seen in the studies of porosity on (PAH 8.5/PAArVBA 3.5)$_{10.5}$ films (section 4.2.2), the DBU-catalyzed films take longer to react to the treatment and reach full porosity. Thus the porosity treatment for these measurements may not have been rigorous enough. The remainder of this section uses only DPAArVBA-containing films.

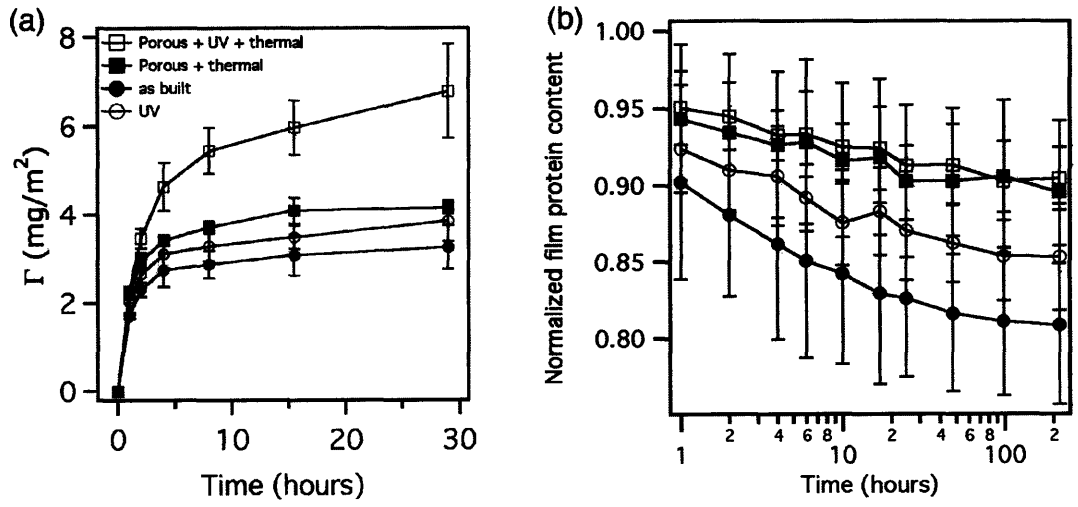

Figure 6.9. Time dependent (a) adsorption and (b) desorption of albumin from (PAH 8.5/DPAArVBA 3.5)$_{10.5}$ films after various treatments. Most of the protein stays immobilized within the multilayer films. Note that the x-axis in desorption is log scale.

The desorption measurements show that the protein stays essentially immobilized in the film for all conditions. The apparent decrease in protein content can be attributed to the effect of hydrolysis on the ^{125}I-BSA, cleaving the radioactive iodine from the protein and allowing the iodine to escape.

For all but the porous thermally crosslinked films, the amount of protein uptake corresponds to a monolayer of adsorbed albumin, which has been shown to resist desorption from (PAH/SPS) films [133] and (PAH 7.5/PAA 3.5) films [77]. The porous film uptake may also be a simple monolayer adsorbed to the inside of the pores and the higher adsorption amount a result of the much greater surface area. This is supported by the previously seen low uptake in thermally crosslinked films without porosity. Purely porous films without thermal crosslinking show little uptake as well, but this is likely due to the closing of the pores over the course of the immersion time in BSA solution. The pores are preserved only in the case of the thermal crosslinking.

To determine whether the lower comparative adsorption in the DPAArVBA-containing porous films versus the TPAArVBA-containing films was due to processing, FITC-BSA was used to visualize the difference in adsorption between the processing conditions for DPAArVBA-containing films. Figure 6.10 shows UV-patterned samples followed by porosity and thermal crosslinking for (a) less-aggressive porosity treatment (5 cycles at 15s pH 2.3, 90s DI water) and (b) more-aggressive porosity treatment (8 cycles at 90s pH 2.3, 90s DI water), both immersed in FITC-BSA solution for 18 hours.

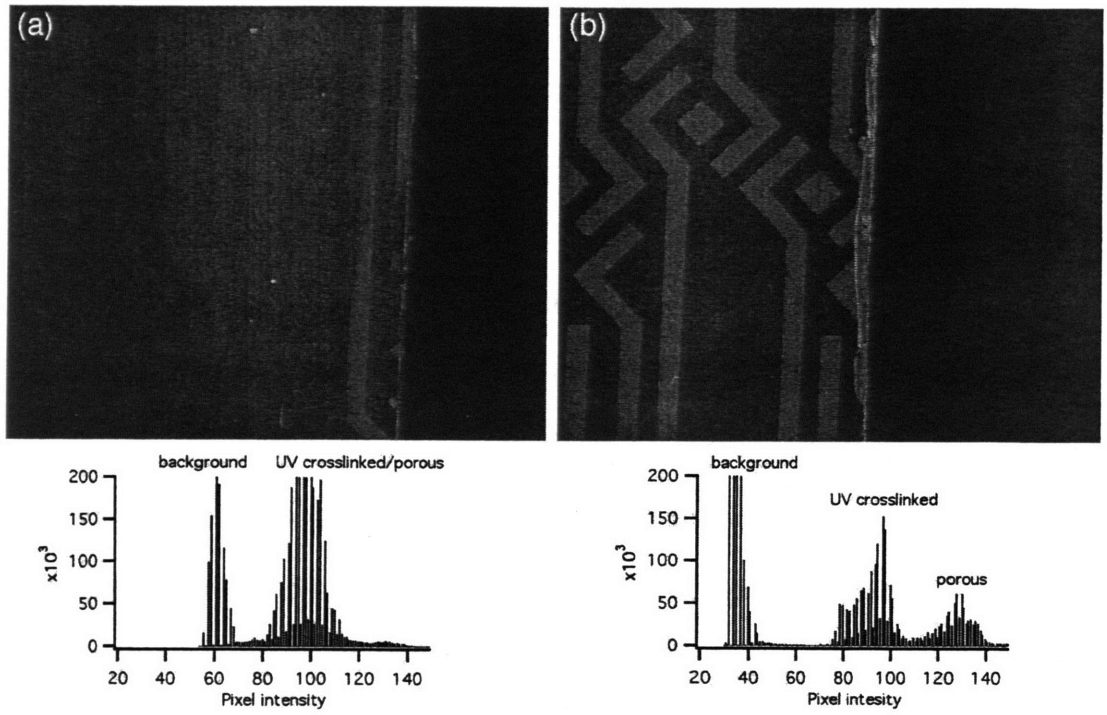

Figure 6.10. Fluorescence micrograph of fluorescein isothiocyanate-labeled albumin uptake in UV-patterned (PAH 8.5/DPAArVBA 3.5)$_{10.5}$ films after (a)less aggressive porosity treatment used for radiolabeled adsorption experiment and (b)more aggressive porosity treatment used for making Bragg reflector films in section 5.1. The pixel intensity histograms below the images show the clear differentiation of the porous regions in the more aggressively treated film.

The low differentiation between the porous and nonporous regions in the less-aggressive treatment qualitatively suggests that using the more-aggressive treatment should achieve more protein uptake than was demonstrated in the time-dependent adsorption study (Figure 6.9), closer to the level measured previously (Figure 6.8).

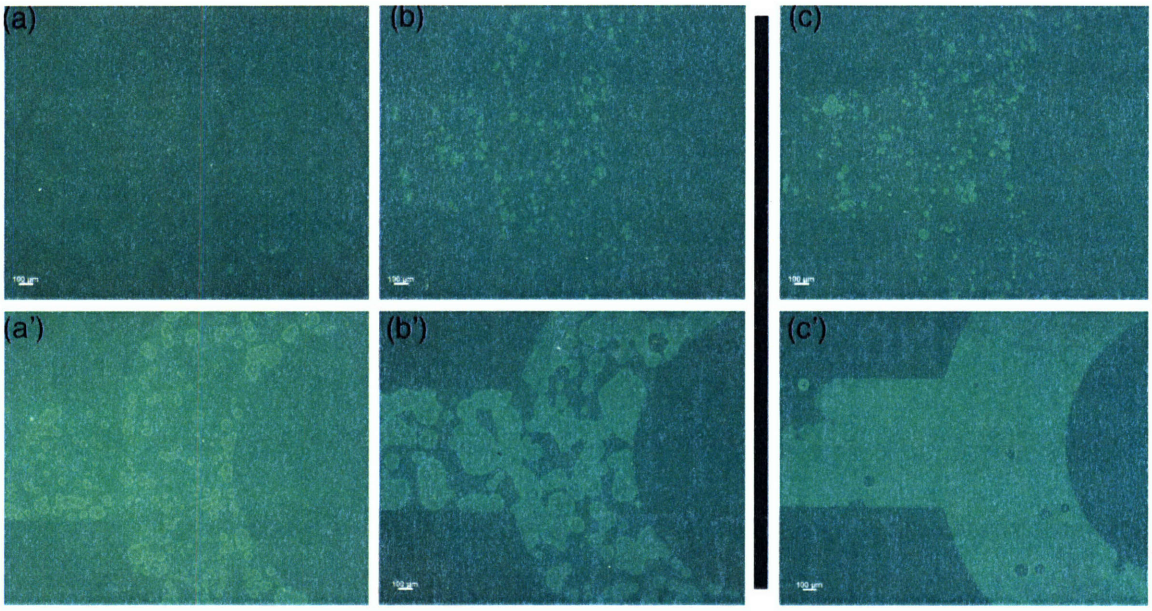

Figure 6.11. FITC-BSA adsorption into one one A-stack patterned porous (PAH 4.0/SPS 4.0)$_{50}$-(PAH 8.5/PAArVBA 3.5)$_{5.5}$-(SPS 4.0/PAH 4.0)$_{50.5}$ films for 2 hours and (') 24 hours. (a, a') 1xPBS solution and (b, b') 2xPBS solution. (c, c') 2xPBS solution adsorption for 2 hours and 48 hours showing near complete filling of the pattern.

Finally, the adsorption behavior of the patterned porous (PAH 4.0/SPS 4.0)$_{50}$-(PAH 8.5/DPAArVBA 3.5)$_{5.5}$-(SPS 4.0/PAH 4.0)$_{50.5}$ system was examined. Berg et al. reported that the PAH/SPS layers did not provide a barrier to the entry or exit of small molecules from the porous regions of their films (with PAA rather than PAArVBA) [80]. Schlenoff et al. demonstrated that PAH/SPS multilayer films prevent or allow albumin to reside in the films, depending on whether the top surface was negatively (prevent) or positively (allow) charged [160]. As porous (PAH 8.5/PAArVBA 3.5) films were found to strongly uptake BSA (Figure 6.8), these experiments allowed the determination of whether proteins can be confined to the porous film regions of patterned films.

Figure 6.11 shows fluorescence micrographs of protein uptake into patterned porous films. On the left is protein uptake from 1xPBS solution, in the middle is protein uptake from 2xPBS solution. The time-point at the top is 2 hours, while the bottom is 24 hours.

On the right is BSA uptake from 2xPBS at 2 hours (top) and 48 hours (bottom). The filling of the porous pattern occurs from individual points in the porous film region that expand, impinging on each other and mixing. Of note is that when the proteins reach the edge of the pattern they stop, confirming that protein uptake occurs only in the porous stack and not the PAH/SPS stack. Also of note is the slow lateral diffusion of the proteins in the film. BSA adsorbing to PAH 8.5/PAArVBA 3.5 multilayers without the PAH/SPS capping layers filled the full pattern in less than an hour, so one would expect that albumin, upon reaching the porous stack through the PAH/SPS layers would quickly spread out to a uniform distribution in the porous stack eliminating any difference in color. Increasing the ionic strength has the effect of increasing the adsorption rate, probably due to the screening of charges in the film, leading to swelling of the PAH/SPS stack in the film and easier penetration of BSA through to the porous stack. This enhancement of protein diffusion with increasing ionic strength has been seen for (PAH/SPS) films incorporating albumin [133].

Chapter 7. Conclusions and future work

7.1 Conclusions

This thesis has demonstrated the synthesis and use of a photo-crosslinkable weak polyelectrolyte for the purpose of controlling structural properties and transformations in polyelectrolyte multilayer assemblies (PEMs). The synthesis of poly(acrylic acid-*ran*-vinylbenzyl acrylate) (PAArVBA) was developed as a facile method of creating a photoactive polyanion. Weak polyelectrolyte multilayer films incorporating PAArVBA were characterized by several parameters commonly assessed for PEMs, including assembly thickness and degree of swelling in solution. The photo-crosslinking of low pH assembled (PAH/PAArVBA) films was shown through inhibition of swelling, increases in stability and changes in mechanical stiffness of films in aqueous solution. In addition, film swelling was patterned with masked UV exposure and unpatterned regions of masked films showed significant swelling at high pH, which is common for (PAH/PAA) films of this type.

PAArVBA was used to inhibit pore formation in (PAH 7.5/PAArVBA 3.5) and (PAH 8.5/PAArVBA 3.5) films and this morphological control was used to create patterned porosity, and to observe the effects of lateral constriction on pore morphology by AFM and optical microscopy.

The ability to locally inhibit porosity was used to make laterally patterned heterostack PEM Bragg reflectors with two different structure types. The first was a modification of the previously explored structure, with nonporous (PAH/SPS) stacks sandwiching porous (PAH/PAArVBA) stacks. The reflectivity is dependent on the

porosity to make stacks of alternating refractive index, so lateral patterns were made through the inhibition of that porosity. The second was a new structure with (PAH/PAArVBA) stacks sandwiching (PAH/PAA) stacks. When crosslinked, the outside stacks stayed nonporous giving the alternating refractive index structure, but when masked, the entirety of the film became porous, leading to light scattering rather than reflection. Both patterned structures were characterized with respect to film thickness, surface topography and reflectivity, and simulations of the structure were used to determine optical properties of the films.

Finally, the porous patterned structure and the heterostack (PAH/SPS)-(PAH/PAArVBA) structure were used to control model small molecule uptake as well as albumin uptake. UV-patterned and patterned porous (PAH 8.5/PAArVBA 3.5) films were shown to exhibit different affinities for different fluorescent dyes based on net charge and hydrophobicity. $(\text{PAH 4.0/SPS 4.0})_{50}$-$(\text{PAH 8.5/PAArVBA 3.5})_{5.5}$-$(\text{SPS 4.0/PAH 4.0})_{50.5}$ films were patterned to make porous channels, and these were used to simultaneously load separate dyes into films without mixing. Albumin adsorption into films processed for UV-crosslinking, porosity and thermal crosslinking was measured using radiolabeled protein, and adsorption within porous thermally crosslinked films was determined to be much greater than for films built and processed under other conditions. This difference was exploited to pattern protein adsorption as visualized by fluorescence microscopy of FITC-BSA.

Several of the structures created in the course of this thesis are interesting in terms of the ability to control topography and optical properties through the patterning of porosity. It is also interesting that the chemical affinity of various species can be controlled by the

application of porosity as well. Aside from porosity, the ability to pattern mechanical stiffness may prove to be useful. There are several immediate ways that the potential for PAArVBA-containing films can be explored, as well as more long-term applications.

7.2 Future work

Perhaps the most immediate use for PAArVBA-containing PEM films is for control of mechanical properties for use in studies on cell adhesion and motility. Fibroblasts have been shown to exhibit differences in cell adhesion for PEMs when the substrate modulus varies in the range of 10^5-10^8 Pa [90]. Other studies have seen similar effects [91, 113]. While the mechanical stiffness range measured in this thesis would be considered too low to achieve different behaviors from commonly examined cell lines, there are several factors to consider. Firstly, the pH-dependent properties of weak polyelectrolyte films, including the stiffness, can be varied significantly and we have examined only one system (PAH 3.5/PAArVBA 3.5). Thus an effect of the crosslinking might be felt for films built with a higher base stiffness, but still below that for cell adhesion. In that case, the crosslinking could increase the modulus enough to promote cell adhesion, allowing patterning of adhesive cells. Secondly, the studies in this thesis examined films constructed with TEA-catalyzed PAArVBA, which are influenced by the ionic nature of the TEA residue, making more swollen, less stable structures. The moduli of the films measured were extremely low compared to PAH/PAA films built at the same pH and this may be partially a result of the polymer used. Using DBU-catalyzed PAArVBA may put the base modulus of (PAH 3.5/PAArVBA 3.5) in the right range to control cell adhesion. If nothing else, the determination of the modulus variation for a wide swath of pH assembly conditions would be an interesting pursuit.

Outside of cell adhesion, patterned control over mechanical properties is useful for other applications. Recently Balazs and coworkers demonstrated through simulation the ability to sort microcapsules according to mechanical compliance by using a mechanically patterned substrate [161]. Such a substrate might be readily prepared using the PEM systems investigated herein.

Another way to change the mechanical stiffness is by loading a film with other materials such as stiffer polymers or nanoparticles. The high affinity of our porous films for small molecules of various types may make them amenable to loading with monomer and *in situ* polymerization within the porous regions. Exploring the extent of the patterned loading abilites could lead to radically different mechanical properties within a single film. It should be relatively straightforward for example to use the highly negatively charged pores in a non-thermally crosslinked (PAH 8.5/PAArVBA 3.5) to synthesize metal nanoparticles with the approach used by Cohen and coworkers [162-164] of adsorbing metal ions for reduction in the film to make nanoparticles, e.g., for catalysis for electroless plating.

There is further potential for these systems to be employed for biological applications. The porous forms of these multilayer systems have high surface area available for binding, which is always an advantage for applications such as bioassays and biosensors. And patterned arrays with small spot sizes can be made easily with this technique.

Optically patterned arrays for sensing can also be made easily using this technique. The assembly of patterned Bragg reflectors for a particular wavelength of light is simply a matter of choosing the appropriate number of layers. Since the build process can be

interrupted at any time, and restarted, one could easily pattern an optical structure in a one A-stack film, build another A-stack, pattern that layer, build another and pattern that layer to achieve more complex spatially patterned structures to, for example reflect different wavelengths of light to enhance the signal from a fluorescence response occurring on the top surface of the film.

Lastly, the ability of the porous layers to load molecules with capillarity may provide a way to potentially load incompatible materials onto the same surface. Again, an easy first application of this could be to selectively load two different metal salts in separate channels to make nanoparticles. Or to simply build channels atop one another.

As a last note, the author would like to state his personal opinion that a significant area of promise for PEM systems in general is in the area of microfluidics. The ability to conformally coat fluidic channels along with the continually expanding functionality to be found in PEMs should lead to novel methods of sensing and chemically modifying materials within lab-on-a-chip applications. Thus far, there has not been much research into building multilayers within fluidic channels, but it would seem inevitable.

Bibliography

1. Elbert, D. L.; Hubbell, J. A., Surface treatments of polymers for biocompatibility. In *Polymers*, Annual Reviews Inc, Palo Alto, CA, USA: 1996; Vol. 26, pp 365-394.
2. McPherson, T.; Kidane, A.; Szleifer, I.; Park, K., Prevention of protein adsorption by tethered poly(ethylene oxide) layers: experiments and single-chain mean-field analysis. *Langmuir* **1998,** 14, (1), 176-186.
3. Banerjee, P.; Irvine, D. J.; Mayes, A. M.; Griffith, L. G., Polymer latexes for cell-resistant and cell-interactive surfaces. *Journal of Biomedical Materials Research* **2000,** 50, (3), 331-339.
4. Hester, J. F.; Banerjee, P.; Mayes, A. M., Preparation of protein-resistant surfaces on poly(vinylidene fluoride) membranes via surface segregation. *Macromolecules* **1999,** 32, (5), 1643-1650.
5. Harder, P.; Grunze, M.; Dahint, R.; Whitesides, G. M.; Laibinis, P. E., Molecular conformation in oligo(ethylene glycol)-terminated self-assembled monolayers on gold and silver surfaces determines their ability to resist protein adsorption. *Journal of Physical Chemistry B* **1998,** 102, (2), 426-436.
6. Szleifer, I., Polymers and proteins: Interactions at interfaces. *Current Opinion in Solid State and Materials Science* **1997,** 2, (3), 337-344.
7. Ouchi, T.; Kontani, T.; Saito, T.; Ohya, Y., Suppression of cell attachment and protein adsorption onto amphiphilic polylactide-grafted dextran films. *Journal of Biomaterials Science, Polymer Edition* **2005,** 16, (8), 1035-1045.
8. Massia, S. P.; Stark, J.; Letbetter, D. S., Surface-immobilized dextran limits cell adhesion and spreading. *Biomaterials* **2000,** 21, (22), 2253-2261.
9. Irvine, D. J.; Mayes, A. M.; Griffith, L. G., Nanoscale clustering of RGD peptides at surfaces using comb polymers. 1. Synthesis and characterization of comb thin films. *Biomacromolecules* **2001,** 2, (1), 85-94.
10. Ji, J.; Zhu, H.; Shen, J., Surface tailoring of poly(DL-lactic acid) by ligand-tethered amphiphilic polymer for promoting chondrocyte attachment and growth. *Biomaterials* **2004,** 25, (10), 1859-1867.
11. Wang, D.-A.; Feng, L.-X.; Ji, J.; Sun, Y.-H.; Zheng, X.-X.; Elisseeff, J. H., Novel human endothelial cell-engineered polyurethane biomaterials for cardiovascular biomedical applications. *Journal of Biomedical Materials Research - Part A* **2003,** 65, (4), 498-510.
12. Decher, G.; Hong, J. D., Buildup of ultrathin multilayer films by a self-assembly process. II. Consecutive adsorption of anionic and cationic bipolar amphiphiles and polyelectrolytes on charged surfaces. *Berichte der Bunsengesellschaft fuer Physikalische Chemie* **1991,** 95, (11), 1430.
13. Decher, G.; Ebler, F.; Hong, J. D.; Lowack, K.; Schmitt, J.; Lvov, Y., Layer-by-layer adsorbed films of polyelectrolytes, proteins or DNA. *Polymer Preprints, Division of Polymer Chemistry, American Chemical Society* **1993,** 34, (1), 745.
14. Lvov, Y.; Decher, G.; Sukhorukov, G., Assembly of thin films by means of successive deposition alternate layers of DNA and poly(allylamine). *Macromolecules* **1993,** 26, (20), 5396-5399.
15. Dai, J.; Balachandra, A. M.; Lee Ii, J.; Bruening, M. L., Controlling ion transport through multilayer polyelectrolyte membranes by derivatization with photolabile functional groups. *Macromolecules* **2002,** 35, (8), 3164-3170.
16. Bruening, M. L.; Sullivan, D. M., Enhancing the ion-transport selectivity of multilayer polyelectrolyte membranes. *Chemistry - A European Journal* **2002,** 8, (17), 3832-3837.

17. Balachandra, A. M.; Dai, J.; Bruening, M. L., Enhancing the anion-transport selectivity of multilayer polyelectrolyte membranes by templating with Cu²⁺. *Macromolecules* **2002,** 35, (8), 3171-3178.
18. Graul, T. W.; Schlenoff, J. B., Capillaries modified by polyelectrolyte multilayers for electrophoretic separations. *Analytical Chemistry* **1999,** 71, (18), 4007-4013.
19. Pavoor, P. V.; Gearing, B. P.; Muratoglu, O.; Cohen, R. E.; Bellare, A., Wear reduction of orthopaedic bearing surfaces using polyelectrolyte multilayer nanocoatings. *Biomaterials* **2006,** 27, (8), 1527-1533.
20. Yap, H. P.; Quinn, J. F.; Ng, S. M.; Cho, J.; Caruso, F., Colloid surface engineering via deposition of multilayered thin films from polyelectrolyte blend solutions. *Langmuir* **2005,** 21, (10), 4328-4333.
21. Schuetz, P.; Caruso, F., Copper-Assisted Weak Polyelectrolyte Multilayer Formation on Microspheres and Subsequent Film Crosslinking. *Advanced Functional Materials* **2003,** 13, (12), 929-937.
22. Khopade, A. J.; Caruso, F., Surface-modification of polyelectrolyte multilayer-coated particles for biological applications. *Langmuir* **2003,** 19, (15), 6219-6225.
23. Gittins, D. I.; Caruso, F., Tailoring the polyelectrolyte coating of metal nanoparticles. *Journal of Physical Chemistry B* **2001,** 105, (29), 6846-6852.
24. Park, M.-K.; Xia, C.; Advincula, R. C.; Schutz, P.; Caruso, F., Cross-linked, luminescent spherical colloidal and hollow-shell particles. *Langmuir* **2001,** 17, (24), 7670-7674.
25. Pastoriza-Santos, I.; Scholer, B.; Caruso, F., Core-shell colloids and hollow polyelectrolyte capsules based on diazoresins. *Advanced Funtional Materials* **2001,** 11, (2), 122-128.
26. Caruso, F.; Schueler, C., Enzyme multilayers on colloid particles: Assembly, stability, and enzymatic activity. *Langmuir* **2000,** 16, (24), 9595-9603.
27. Susha, A. S.; Caruso, F.; Rogach, A. L.; Sukhorukov, G. B.; Kornowski, A.; Moehwald, H.; Giersig, M.; Eychmueller, A.; Weller, H., Formation of luminescent spherical core-shell particles by the consecutive adsorption of polyelectrolyte and CdTe(S) nanocrystals on latex colloids. *Colloids and Surfaces A: Physicochemical and Engineering Aspects* **2000,** 163, (1), 39-44.
28. Sukhorukov, G. B.; Donath, E.; Davis, S.; Lichtenfeld, H.; Caruso, F.; Popov, V. I.; Moehwald, H., Stepwise polyelectrolyte assembly on particle surfaces: a novel approach to colloid design. *Polymers for Advanced Technologies* **1998,** 9, (10-11), 759-767.
29. Smith, R. N.; McCormick, M.; Barrett, C. J.; Reven, L.; Spiess, H. W., NMR studies of PAH/PSS polyelectrolyte multilayers adsorbed onto silica. *Macromolecules* **2004,** 37, (13), 4830-4838.
30. Lvov, Y.; Decher, G.; Haas, H.; Mohwald, H.; Kalachev, A., X-ray analysis of ultrathin polymer films self-assembled onto substrates. *Physica B: Condensed Matter* **1994,** 198, (1-3), 89-91.
31. Lvov, Y.; Haas, H.; Decher, G.; Moehwald, H.; Kalachev, A., Assembly of polyelectrolyte molecular films onto plasma-treated glass. *Journal of Physical Chemistry* **1993,** 97, (49), 12835-12841.
32. Korneev, D.; Lvov, Y.; Decher, G.; Schmitt, J.; Yaradaikin, S., Neutron reflectivity analysis of self-assembled film superlattices with alternate layers of deuterated and hydrogenated polysterenesulfonate and polyallylamine. *Physica B: Condensed Matter* **1995,** 213-214, 954-956.
33. Lavalle, P.; Gergely, C.; Cuisinier, F. J. G.; Decher, G.; Schaaf, P.; Voegel, J. C.; Picart, C., Comparison of the structure of polyelectrolyte multilayer films exhibiting a linear and an exponential growth regime: An in situ atomic force microscopy study. *Macromolecules* **2002,** 35, (11), 4458-4465.
34. Picart, C.; Lavalle, P.; Hubert, P.; Cuisinier, F. J. G.; Decher, G.; Schaaf, P.; Voegel, J. C., Buildup mechanism for poly(L-lysine)/hyaluronic acid films onto a solid surface. *Langmuir* **2001,** 17, (23), 7414-7424.

35. Arys, X.; Jonas, A. M.; Laguitton, B.; Laschewsky, A.; Legras, R.; Wischerhoff, E., Ultrathin multilayers made by alternate deposition of ionenes and polyvinylsulfate: From unstable to stable growth. *Thin Solid Films* **1998,** 327-329, 734-738.
36. Arys, X.; Laschewsky, A.; Jonas, A. M., Ordered polyelectrolyte "multilayers" - 1. Mechanisms of growth and structure formation: A comparison with classical fuzzy "multilayers". *Macromolecules* **2001,** 34, (10), 3318-3330.
37. Clark, S. L.; Hammond, P. T., Role of secondary interactions in selective electrostatic multilayer deposition. *Langmuir* **2000,** 16, (26), 10206-10214.
38. Yang, S. Y.; Rubner, M. F., Micropatterning of polymer thin films with pH-sensitive and cross-linkable hydrogen-bonded polyelectrolyte multilayers. *Journal of the American Chemical Society* **2002,** 124, (10), 2100-2101.
39. Cho, J.; Caruso, F., Polymeric multilayer films comprising deconstructible hydrogen-bonded stacks confined between electrostatically assembled layers. *Macromolecules* **2003,** 36, (8), 2845-2851.
40. Kharlampieva, E.; Sukhishvili, S. A., Polyelectrolyte multilayers of weak polyacid and cationic copolymer: Competition of hydrogen-bonding and electrostatic interactions. *Macromolecules* **2003,** 36, (26), 9950-9956.
41. Yang, S. Y.; Mendelsohn, J. D.; Rubner, M. F., New class of ultrathin, highly cell-adhesion-resistant polyelectrolyte multilayers with micropatterning capabilities. *Biomacromolecules* **2003,** 4, (4), 987-994.
42. Yang, S. Y.; Lee, D.; Cohen, R. E.; Rubner, M. F., Bioinert solution-cross-linked hydrogen-bonded multilayers on colloidal particles. *Langmuir* **2004,** 20, (14), 5978-5981.
43. Vargo, T. G.; Calvert, J. M.; Wynne, K. J.; Avlyanov, J. K.; MacDiarmid, A. G.; Rubner, M. F., Patterned polymer multilayer fabrication by controlled adhesion of polyelectrolytes to plasma-modified fluoropolymer surfaces. *Supramolecular Science* **1995,** 2, (3-4), 169-174.
44. Sukhishvili, S. A.; Granick, S., Layered, erasable polymer multilayers formed by hydrogen-bonded sequential self-assembly. *Macromolecules* **2002,** 35, (1), 301-310.
45. Kozlovskaya, V.; Ok, S.; Sousa, A.; Libera, M.; Sukhishvili, S. A., Hydrogen-bonded polymer capsules formed by layer-by-layer self-assembly. *Macromolecules* **2003,** 36, (23), 8590-8592.
46. Wu, A.; Lee, J.; Rubner, M. F., Light emitting electrochemical devices from sequentially adsorbed multilayers of a polymeric ruthenium (II) complex and various polyanions. *Thin Solid Films* **1998,** 327-329, 663-667.
47. Caruso, F.; Kurth, D. G.; Volkmer, D.; Koop, M. J.; Mueller, A., Ultrathin molybdenum polyoxometalate-polyelectrolyte multilayer films. *Langmuir* **1998,** 14, (13), 3462-3465.
48. Wu, A.; Lee, J.-k.; Rubner, M. F., *Electrochemically based light emitting devices from sequentially adsorbed multilayers of a polymeric ruthenium (II) complex and poly(acrylic acid)*,MRS, Warrendale, PA, USA: Boston, MA, USA, 1997; pp 63-68.
49. Petrov, A. I.; Gavryushkin, A. V.; Sukhorukov, G. B., Effect of temperature, pH and shell thickness on the rate of Mg²⁺ and Ox²⁻ release from multilayered polyelectrolyte shells deposited onto microcrystals of magnesium oxalate. *Journal of Physical Chemistry B* **2003,** 107, (3), 868-875.
50. Jaber, J. A.; Schlenoff, J. B., Polyelectrolyte multilayers with reversible thermal responsivity. *Macromolecules* **2005,** 38, (4), 1300-1306.
51. Kohler, K.; Shchukin, D. G.; Mohwald, H.; Sukhorukov, G. B., Thermal behavior of polyelectrolyte multilayer microcapsules. 1. The effect of odd and even layer number. *Journal of Physical Chemistry B* **2005,** 109, (39), 18250-18259.
52. Baur, J. W.; Kim, S.; Balanda, P. B.; Reynolds, J. R.; Rubner, M. F., Thin-film light-emitting devices based on sequentially adsorbed multilayers of water-soluble poly(p-phenylene)s. *Advanced Materials* **1998,** 10, (17), 1452-1455.

53. Tan, Q.; Ji, J.; Fonseca, C.; Shen, J.; Barbosa, M. A., Constructing thromboresistant surface on biomedical stainless steel via layer-by-layer deposition anticoagulant. *Biomaterials* **2003,** 24, (25), 4699-4705.
54. Brynda, E.; Houska, M.; Jirouskova, M.; Dyr, J. E., Albumin and heparin multilayer coatings for blood-contacting medical devices. *Journal of Biomedical Materials Research* **2000,** 51, (2), 249-257.
55. Kim, H.; Urban, M. W., Reactions of thrombresistant multilayered thin films on poly(vinyl chloride) (PVC) surfaces: a spectroscopic study. *Langmuir* **1998,** 14, (25), 7235-7244.
56. Zhang, S.; Niu, Y.; Sun, C., Construction of covalently attached enzyme multilayer films based on the photoreaction of diazo-resins and glucose oxidase. *Electrochimica Acta* **2004,** 49, (26), 4777-4786.
57. Caruso, F.; Fiedler, H.; Haage, K., Assembly of β-glucosidase multilayers on spherical colloidal particles and their use as active catalysts. *Colloids and Surfaces A: Physicochemical and Engineering Aspects* **2000,** 169, (1), 287-293.
58. Lehr, B.; Seufert, M.; Wenz, G.; Decher, G., Fabrication of poly(p-phenylene vinylene) (PPV) nanoheterocomposite films via layer-by-layer adsorption. *Supramolecular Science* **1995,** 2, (3-4), 199-207.
59. Dubas, S. T.; Schlenoff, J. B., Factors controlling the growth of polyelectrolyte multilayers. *Macromolecules* **1999,** 32, (24), 8153-8160.
60. Dubas, S. T.; Schlenoff, J. B., Polyelectrolyte multilayers containing a weak polyacid: Construction and deconstruction. *Macromolecules* **2001,** 34, (11), 3736-3740.
61. Dubas, S. T.; Schlenoff, J. B., Swelling and smoothing of polyelectrolyte multilayers by salt. *Langmuir* **2001,** 17, (25), 7725-7727.
62. Fery, A.; Scholer, B.; Cassagneau, T.; Caruso, F., Nanoporous thin films formed by salt-induced structural changes in multilayers of poly(acrylic acid) and poly(allylamine). *Langmuir* **2001,** 17, (13), 3779-3783.
63. Ladam, G.; Schaad, P.; Voegel, J. C.; Schaaf, P.; Decher, G.; Cuisinier, F., In situ determination of the structural properties of initially deposited polyelectrolyte multilayers. *Langmuir* **2000,** 16, (3), 1249-1255.
64. Cohen Stuart, M. A.; Kovacevic, D.; Van der Burgh, S.; De Keizer, A., Kinetics of formation and dissolution of weak polyelectrolyte multilayers: Role of salt and free polyions. *Langmuir* **2002,** 18, (14), 5607-5612.
65. Durstock, M. F.; Rubner, M. F., *Light emitting devices based on sequentially adsorbed layers of poly(p-phenylene vinylene) (PPV) and poly(acrylic acid) (PAA)*,The International Society for Optical Engineering: San Diego, CA, United States, 1997; pp 126-131.
66. Yoo, D.; Shiratori, S. S.; Rubner, M. F., Controlling bilayer composition and surface wettability of sequentially adsorbed multilayers of weak polyelectrolytes. *Macromolecules* **1998,** 31, (13), 4309-4318.
67. Mendelsohn, J. D.; Barrett, C. J.; Chan, V. V.; Pal, A. J.; Mayes, A. M.; Rubner, M. F., Fabrication of microporous thin films from polyelectrolyte multilayers. *Langmuir* **2000,** 16, (11), 5017-5023.
68. Shiratori, S. S.; Rubner, M. F., pH-dependent thickness behavior of sequentially adsorbed layers of weak polyelectrolytes. *Macromolecules* **2000,** 33, (11), 4213-4219.
69. Park, S. Y.; Rubner, M. F.; Mayes, A. M., Free energy model for layer-by-layer processing of polyelectrolyte multilayer films. *Langmuir* **2002,** 18, (24), 9600-9604.
70. Park, S. Y.; Barrett, C. J.; Rubner, M. F.; Mayes, A. M., Anomalous adsorption of polyelectrolyte layers. *Macromolecules* **2001,** 34, (10), 3384-3388.
71. Burke, S. E.; Barrett, C. J., pH-dependent loading and release behavior of small hydrophilic molecules in weak polyelectrolyte multilayer films. *Macromolecules* **2004,** 37, (14), 5375-5384.
72. Tanchak, O. M.; Barrett, C. J., Swelling dynamics of multilayer films of weak polyelectrolytes. *Chemistry of Materials* **2004,** 16, (14), 2734-2739.

73. Mermut, O.; Barrett, C. J., Effects of charge density and counterions on the assembly of polyelectrolyte multilayers. *Journal of Physical Chemistry B* **2003,** 107, (11), 2525-2530.
74. Burke, S. E.; Barrett, C. J., Acid-base equilibria of weak polyelectrolytes in multilayer thin films. *Langmuir* **2003,** 19, (8), 3297-3303.
75. Sukhorukov, G. B.; Moehwald, H.; Decher, G.; Lvov, Y. M., Assembly of polyelectrolyte multilayer films by consecutively alternating adsorption of polynucleotides and polycations. *Thin Solid Films* **1996,** 284-285, 220-223.
76. Clark, S. L.; Handy, E. S.; Rubner, M. F.; Hammond, P. T., Creating microstructures of luminescent organic thin films using layer-by-layer assembly. *Advanced Materials* **1999,** 11, (12), 1031-1035.
77. Mendelsohn, J. D.; Yang, S. Y.; Hiller, J. A.; Hochbaum, A. I.; Rubner, M. F., Rational design of cytophilic and cytophobic polyelectrolyte multilayer thin films. *Biomacromolecules* **2003,** 4, (1), 96-106.
78. Hiller, J. a.; Mendelsohn, J. D.; Rubner, M. F., Reversibly erasable nanoporous anti-reflection coatings from polyelectrolyte multilayers. *Nature Materials* **2002,** 1, (1), 59-63.
79. Zhai, L.; Nolte, A. J.; Cohen, R. E.; Rubner, M. F., PH-Gated porosity transitions of polyelectrolyte multilayers in confined geometries and their application as tunable Bragg reflectors. *Macromolecules* **2004,** 37, (16), 6113-6123.
80. Berg, M. C.; Zhai, L.; Cohen, R. E.; Rubner, M. F., Controlled drug release from porous polyelectrolyte multilayers. *Biomacromolecules* **2006,** 7, (1), 357-364.
81. Thierry, B.; Winnik, F. M.; Merhi, Y.; Silver, J.; Tabrizian, M., Bioactive coatings of endovascular stents based on polyelectrolyte multilayers. *Biomacromolecules* **2003,** 4, (6), 1564-1571.
82. Schultz, P.; Vautier, D.; Richert, L.; Jessel, N.; Haikel, Y.; Schaaf, P.; Voegel, J.-C.; Ogier, J.; Debry, C., Polyelectrolyte multilayers functionalized by a synthetic analogue of an anti-inflammatory peptide, α-MSH, for coating a tracheal prosthesis. *Biomaterials* **2005,** 26, (15), 2621-2630.
83. Serizawa, T.; Yamaguchi, M.; Matsuyama, T.; Akashi, M., Alternating bioactivity of polymeric layer-by-layer assemblies: Anti-vs procoagulation of human blood on chitosan and dextran sulfate layers. *Biomacromolecules* **2000,** 1, (3), 306-309.
84. Picart, C.; Richert, L.; Elkaim, R.; Schaaf, P.; Voegel, J.-C.; Frisch, B., *Primary osteoblasts adhesion onto RGD-functionalized and cross-linked polyelectrolyte multilayer films,*Materials Research Society, Warrendale, PA 15086, United States: San Francisco, CA, United States, 2004; pp 225-230.
85. Tryoen-Toth, P.; Vautier, D.; Haikel, Y.; Voegel, J.-C.; Schaaf, P.; Chluba, J.; Ogier, J., Viability, adhesion, and bone phenotype of osteoblast-like cells on polyelectrolyte multilayer films. *Journal of Biomedical Materials Research* **2002,** 60, (4), 657-667.
86. Rowley, J.; Mooney, D., Controlling myoblast phenotype with material mechanics. *Annals of Biomedical Engineering* **2000,** 28, (SUPPL 1), -14.
87. Chun-Min, L.; Hong-Bei, W.; Dembo, M.; Yu-Li, W., Cell movement is guided by the rigidity of the substrate. *Biophysical Journal* **2000,** 79, (1), 144-52.
88. Wong, J. Y.; Velasco, A.; Rajagopalan, P.; Pham, Q., Directed movement of vascular smooth muscle cells on gradient-compliant hydrogels. *Langmuir* **2003,** 19, (5), 1908-1913.
89. Engler, A.; Bacakova, L.; Newman, C.; Sheehan, M.; Discher, D., *Mechanical role of cytoskeletal components in vascular smooth muscle cell adhesion in vitro,*Institute of Electrical and Electronics Engineers Inc.: Philadelphia, PA, 2002; pp 23-24.
90. Thompson, M. T.; Berg, M. C.; Tobias, I. S.; Rubner, M. F.; Van Vliet, K. J., Tuning compliance of nanoscale polyelectrolyte multilayers to modulate cell adhesion. *Biomaterials* **2005,** 26, (34), 6836-6845.
91. Richert, L.; Boulmedais, F.; Lavalle, P.; Mutterer, J.; Ferreux, E.; Decher, G.; Schaaf, P.; Voegel, J.-C.; Picart, C., Improvement of stability and cell adhesion properties of

polyelectrolyte multilayer films by chemical cross-linking. *Biomacromolecules* **2004,** 5, (2), 284-294.
92. Richert, L.; Engler, A. J.; Discher, D. E.; Picart, C., Elasticity of native and cross-linked polyelectrolyte multilayer films. *Biomacromolecules* **2004,** 5, (5), 1908-1916.
93. Kumar, A.; Whitesides, G. M., FEATURES OF GOLD HAVING MICROMETER TO CENTIMETER DIMENSIONS CAN BE FORMED THROUGH A COMBINATION OF STAMPING WITH AN ELASTOMERIC STAMP AND AN ALKANETHIOL INK FOLLOWED BY CHEMICAL ETCHING. *Applied Physics Letters* **1993,** 63, (14), 2002-2004.
94. Jiang, X.; Zheng, H.; Gourdin, S.; Hammond, P. T., Polymer-on-polymer stamping: Universal approaches to chemically patterned surfaces. *Langmuir* **2002,** 18, (7), 2607-2615.
95. Berg, M. C.; Choi, J.; Hammond, P. T.; Rubner, M. F., Tailored micropatterns through weak polyelectrolyte stamping. *Langmuir* **2003,** 19, (6), 2231-2237.
96. Zheng, H.; Lee, I.; Rubner, M. F.; Hammond, P. T., Two component particle arrays on patterned polyelectrolyte multilayer templates. *Advanced Materials* **2002,** 14, (8), 569-572.
97. Zheng, H.; Rubner, M. F.; Hammond, P. T., Particle assembly on patterned "plus/minus" polyelectrolyte surfaces via polymer-on-polymer stamping. *Langmuir* **2002,** 18, (11), 4505-4510.
98. Lyles, B. F.; Terrot, M. S.; Hammond, P. T.; Gast, A. P., Directed Patterned Adsorption of Magnetic Beads on Polyelectrolyte Multilayers on Glass. *Langmuir* **2004,** 20, (8), 3028-3031.
99. Kim, H.; Doh, J.; Irvine, D.; Cohen, R.; Hammond, P., *Fabrication of large area B cell array using a newly synthesized patternable poly(allylamine)-g-poly(ethylene oxide) graft copolymer,*Biomaterials 2004 Congress Managers, Sydney, NSW 2001, Australia: Sydney, Australia, 2004; p 728.
100. Berg, M. C.; Yang, S. Y.; Hammond, P. T.; Rubner, M. F., Controlling Mammalian Cell Interactions on Patterned Polyelectrolyte Multilayer Surfaces. *Langmuir* **2004,** 20, (4), 1362-1368.
101. Salloum, D. S.; Olenych, S. G.; Keller, T. C. S.; Schlenoff, J. B., Vascular smooth muscle cells on polyelectrolyte multilayers: Hydrophobicity-directed adhesion and growth. *Biomacromolecules* **2005,** 6, (1), 161-167.
102. Park, J.; Hammond, P. T., Multilayer Transfer Printing for Polyelectrolyte Multilayer Patterning: Direct Transfer of Layer-by-Layer Assembled Micropatterned Thin Films. *Advanced Materials* **2004,** 16, (6), 520-525.
103. Lee, N. Y.; Lim, J. R.; Lee, M. J.; Park, S.; Kim, Y. S., Multilayer transfer printing on microreservoir-patterned substrate employing hydrophilic composite mold for selective immobilization of biomolecules. *Langmuir* **2006,** 22, (18), 7689-7694.
104. Shchukin, D. G.; Kommireddy, D. S.; Zhao, Y.; Cui, T.; Sukhorukov, G. B.; Lvov, Y. M., Polyelectrolyte Micropatterning Using a Laminar-Flow Microfluidic Device. *Advanced Materials* **2004,** 16, (5), 389-393.
105. Reyes, D. R.; Perruccio, E. M.; Becerra, S. P.; Locascio, L. E.; Gaitan, M., Micropatterning neuronal cells on polyelectrolyte multilayers. *Langmuir* **2004,** 20, (20), 8805-8811.
106. Lu, Y.; Hu, W.; Ma, Y.; Zhang, L.; Sun, J.; Lu, N.; Shen, J., Patterning layered polymeric multilayer films by room-temperature nanoimprint lithography. *Macromolecular Rapid Communications* **2006,** 27, (7), 505-510.
107. Wang, B.; Feng, J.; Gao, C., Surface wettability of compressed polyelectrolyte multilayers. *Colloids and Surfaces A: Physicochemical and Engineering Aspects* **2005,** 259, (1-3), 1-5.

108. Lee, S. W.; Sanedrin, R. G.; Oh, B.-K.; Mirkin, C. A., Nanostructured polyelectrolyte multilayer organic thin films generated via parallel dip-pen nanolithography. *Advanced Materials* **2005,** 17, (22), 2749-2753.
109. Cho, J.; Jang, H.; Yeom, B.; Kim, H.; Kim, R.; Kim, S.; Char, K.; Caruso, F., Modulating the pattern quality of micropatterned multilayer films prepared by layer-by-layer self-assembly. *Langmuir* **2006,** 22, (3), 1356-1364.
110. Harris, J. J.; DeRose, P. M.; Bruening, M. L., Synthesis of passivating, nylon-like coatings through cross-linking of ultrathin polyelectrolyte films. *Journal of the American Chemical Society* **1999,** 121, (9), 1978.
111. Bruening, M. L.; Harris, J. J.; DeRose, P. M., *Controlling permeability and stability of ultrathin, layered polyelectrolyte films*,American Chemical Society, Washington, DC, USA: Anaheim, CA, USA, 1999; p 451.
112. Sullivan, D. M.; Bruening, M. L., Ultrathin, cross-linked polyimide pervaporation membranes prepared from polyelectrolyte multilayers. *Journal of Membrane Science* **2005,** 248, (1-2), 161-170.
113. Schneider, A.; Francius, G.; Obeid, R.; Schwinte, P.; Hemmerle, J.; Frisch, B.; Schaaf, P.; Voegel, J.-C.; Senger, B.; Picart, C., Polyelectrolyte multilayers with a tunable young's modulus: Influence of film stiffness on cell adhesion. *Langmuir* **2006,** 22, (3), 1193-1200.
114. Picart, C.; Schneider, A.; Etienne, O.; Mutterer, J.; Schaaf, P.; Egles, C.; Jessel, N.; Voegel, J.-C., Controlled degradability of polysaccharide multilayer films in vitro and in vivo. *Advanced Functional Materials* **2005,** 15, (11), 1771-1780.
115. Etienne, O.; Schneider, A.; Taddei, C.; Richert, L.; Schaaf, P.; Voegel, J.-C.; Egles, C.; Picart, C., Degradability of polysaccharides multilayer films in the oral environment: An in vitro and in vivo study. *Biomacromolecules* **2005,** 6, (2), 726-733.
116. Picart, C.; Richert, L.; Boulmedais, F.; Schaaf, P.; Voegel, J.-C., *Physico-chemical and cellular properties of crosslinked polyelectrolyte multilayer films*,Materials Research Society, Warrendale, PA 15086, United States: Boston, MA, United States, 2004; pp 29-31.
117. Tengvall, P.; Jansson, E.; Askendal, A.; Thomsen, P.; Gretzer, C., Preparation of multilayer plasma protein films on silicon by EDC/NHS coupling chemistry. *Colloids and Surfaces B: Biointerfaces* **2003,** 28, (4), 261-272.
118. Li, X.; Huang, Y.; Xiao, J.; Yan, C., Ph responsive PAIAm-g-PIPA microspheres: preparation and drug release. *Journal of Applied Polymer Science* **1995,** 55, (13), 1779-1785.
119. Cao, S.; Zhao, C.; Cao, W., Synthesis of diazoresin and its photocrosslinking reaction. *Polymer International* **1998,** 45, (2), 142-146.
120. Sun, J.; Cheng, L.; Liu, F.; Dong, S.; Wang, Z.; Zhang, X.; Shen, J., Covalently attached multilayer assemblies containing photoreactive diazo-resins and conducting polyaniline. *Colloids and Surfaces A: Physicochemical and Engineering Aspects* **2000,** 169, (1), 209-217.
121. Shi, F.; Dong, B.; Qiu, D.; Sun, J.; Wu, T.; Zhang, X., Layer-by-layer self-assembly of reactive polyelectrolytes for robust multilayer patterning. *Advanced Materials* **2002,** 14, (11), 805-809.
122. Shi, F.; Wang, Z.; Zhao, N.; Zhang, X., Patterned polyelectrolyte multilayer: Surface modification for enhancing selective adsorption. *Langmuir* **2005,** 21, (4), 1599-1602.
123. Sun, J.; Wu, T.; Liu, F.; Wang, Z.; Zhang, X.; Shen, J., Covalently attached multilayer assemblies by sequential adsorption of polycationic diazo-resins and polyanionic poly(acrylic acid). *Langmuir* **2000,** 16, (10), 4620-4624.
124. Cao, W.; Zhao, C.; Cao, J., Synthesis and characterization of 3-methoxydiphenylamine-4-diazonium salt and its diazoresin. *Journal of Applied Polymer Science* **1998,** 69, (10), 1975-1982.
125. Park, M.-K.; Deng, S.; Advincula, R. C., pH-sensitive bipolar ion-permselective ultrathin films. *Journal of the American Chemical Society* **2004,** 126, (42), 13723-13731.

126. Park, M.-K.; Deng, S.; Advincula, R. C., Sustained release control via photo-cross-linking of polyelectrolyte layer-by-layer hollow capsules. *Langmuir* **2005,** 21, (12), 5272-5277.
127. Chung, A. J.; Rubner, M. F., Methods of loading and releasing low molecular weight cationic molecules in weak polyelectrolyte multilayer films. *Langmuir* **2002,** 18, (4), 1176-1183.
128. Wang, X.; Venkatraman, S. S.; Boey, F. Y. C.; Loo, J. S. C.; Tan, L. P., Controlled release of sirolimus from a multilayered PLGA stent matrix. *Biomaterials* **2006,** 27, (32), 5588-5595.
129. Ren, K.; Ji, J.; Shen, J., Construction and enzymatic degradation of multilayered poly-L-lysine/DNA films. *Biomaterials* **2006,** 27, (7), 1152-1159.
130. Ren, K.; Ji, J.; Shen, J., Construction of polycation-based non-viral DNA nanoparticles and polyanion multilayers via layer-by-layer self-assembly. *Macromolecular Rapid Communications* **2005,** 26, (20), 1633-1638.
131. Wood, K. C.; Boedicker, J. Q.; Lynn, D. M.; Hammond, P. T., Tunable drug release from hydrolytically degradable layer-by-layer thin films. *Langmuir* **2005,** 21, (4), 1603-1609.
132. Caruso, F.; Furlong, D. N.; Ariga, K.; Ichinose, I.; Kunitake, T., Characterization of polyelectrolyte-protein multilayer films by atomic force microscopy, scanning electron microscopy, and Fourier transform infrared reflection-absorption spectroscopy. *Langmuir* **1998,** 14, (16), 4559-4565.
133. Ladam, G.; Gergely, C.; Senger, B.; Decher, G.; Voegel, J.-C.; Schaaf, P.; Cuisinier, F. J. G., Protein interactions with polyelectrolyte multilayers: Interactions between human serum albumin and polystyrene sulfonate/polyallylamine multilayers. *Biomacromolecules* **2000,** 1, (4), 674-687.
134. Gergely, C.; Bahi, S.; Szalontai, B.; Flores, H.; Schaaf, P.; Voegel, J.-C.; Cuisinier, F. J. G., Human serum albumin self-assembly on weak polyelectrolyte multilayer films structurally modified by pH changes. *Langmuir* **2004,** 20, (13), 5575-5582.
135. Caruso, F.; Niikura, K.; Furlong, D. N.; Okahata, Y., 2. Assembly of alternating polyelectrolyte and protein multilayer films for immunosensing. *Langmuir* **1997,** 13, (13), 3427-3433.
136. Jessel, N.; Atalar, F.; Lavalle, P.; Mutterer, J.; Decher, G.; Schaaf, P.; Voegel, J.-C.; Ogier, J., Bioactive coatings based on a polyelectrolyte multilayer architecture functionalized by embedded proteins. *Advanced Materials* **2003,** 15, (9), 692-695.
137. Szyk, L.; Schwinte, P.; Voegel, J. C.; Schaaf, P.; Tinland, B., Dynamical behavior of human serum albumin adsorbed on or embedded in polyelectrolyte multilayers. *Journal of Physical Chemistry B* **2002,** 106, (23), 6049-6055.
138. Szyk, L.; Schaaf, P.; Gergely, C.; Voegel, J. C.; Tinland, B., Lateral mobility of proteins adsorbed on or embedded in polyelectrolyte multilayers. *Langmuir* **2001,** 17, (20), 6248-6253.
139. Schwinte, P.; Voegel, J. C.; Picart, C.; Haikel, Y.; Schaaf, P.; Szalontai, B., Stabilizing effects of various polyelectrolyte multilayer films on the structure of adsorbed/embedded fibrinogen molecules: An ATR-FTIR study. *Journal of Physical Chemistry B* **2001,** 105, (47), 11906-11916.
140. Cohen, H. L., ESTERIFICATION OF POLYMERIC CARBOXYLIC ACIDS. *Journal of Polymer Science, Polymer Chemistry Edition* **1976,** 14, (1), 7-22.
141. Deng, J.; Yang, W.; Ranby, B., Surface photografting polymerization of styrene on LDPE film. *Journal of Macromolecular Science - Pure and Applied Chemistry* **2002,** 39 A, (8), 771-786.
142. Rahn, R. O., Potassium iodide as a chemical actinometer for 254 nm radiation: Use of iodate as an electron scavenger. *Photochemistry and Photobiology* **1997,** 66, (4), 450.
143. Tompkins, H. G.; Irene, E. A.; Knovel (Firm) Handbook of ellipsometry. http://www.knovel.com/knovel2/Toc.jsp?BookID=1175

144. Brunner, H.; Vallant, T.; Mayer, U.; Hoffmann, H., Formation of ultrathin films at the solid-liquid interface studied by in situ ellipsometry. *Journal of Colloid and Interface Science* **1999,** 212, (2), 545-552.
145. Domke, J.; Radmacher, M., Measuring the elastic properties of thin polymer films with the atomic force microscope. *Langmuir* **1998,** 14, (12), 3320-3325.
146. Pavoor, P. V.; Bellare, A.; Strom, A.; Yang, D.; Cohen, R. E., Mechanical characterization of polyelectrolyte multilayers using quasi-static nanoindentation. *Macromolecules* **2004,** 37, (13), 4865-4871.
147. Mahaffy, R. E.; Park, S.; Gerde, E.; Kas, J.; Shih, C. K., Quantitative analysis of the viscoelastic properties of thin regions of fibroblasts using atomic force microscopy. *Biophysical Journal* **2004,** 86, (3), 1777-93.
148. Dimitriadis, E. K.; Horkay, F.; Maresca, J.; Kachar, B.; Chadwick, R. S., Determination of elastic moduli of thin layers of soft material using the atomic force microscope. *Biophysical Journal* **2002,** 82, (5), 2798-810.
149. Oommen, B.; Van Vliet, K. J., Effects of nanoscale thickness and elastic nonlinearity on measured mechanical properties of polymeric films. *Thin Solid Films* **2006,** 513, (1-2), 235-242.
150. Hutter, J. L.; Bechhoefer, J., Calibration of atomic-force microscope tips. *Review of Scientific Instruments* **1993,** 64, (7), 1868.
151. Li, Q.; Quinn, J. F.; Caruso, F., Nanoporous polymer thin films via polyelectrolyte templating. *Advanced Materials* **2005,** 17, (17), 2058-2062.
152. Macleod, H. A., *Thin-film optical filters*. 3rd ed.; Institute of Physics Publishing: Philadelphia, 2001.
153. Wang, T. C.; Cohen, R. E.; Rubner, M. F., Metallodielectric photonic structures based on polyelectrolyte multilayers. *Advanced Materials* **2002,** 14, (21), 1534-1537.
154. Nolte, A. J.; Rubner, M. F.; Cohen, R. E., Creating Effective Refractive Index Gradients within Polyelectrolyte Multilayer Films: Molecularly Assembled Rugate Filters. *Langmuir* **2004,** 20, (8), 3304-3310.
155. Abeles, F., Investigations on the propagation of sinusoidal electromagnetic waves in stratified media. Application to thin films. *Annales de Physique* **1950,** 5, 596-640.
156. Alfrey Jr, T.; Gurnee, E. F.; Schrenk, W. J., Physical optics of iridescent multilayered plastic films. *Polymer Engineering and Science* **1969,** 9, (6), 400-4.
157. Romanov, S. G.; Maka, T.; Sotomayor Torres, C. M.; M¸ller, M.; Zentel, R.; Cassagne, D.; Manzanares-Martinez, J.; Jouanin, C., Diffraction of light from thin-film polymethylmethacrylate opaline photonic crystals. *Physical Review E* **2001,** 63, (5), 056603.
158. Pradhan, R. D.; Tarhan, *f*. *f*. n.; Watson, G. H., Impurity modes in the optical stop bands of doped colloidal crystals. *Physical Review B* **1996,** 54, (19), 13721.
159. Olugebefola, S. C.; Ryu, S.-W.; Nolte, A. J.; Rubner, M. F.; Mayes, A. M., Photo-cross-linkable polyelectrolyte multilayers for 2-D and 3-D patterning. *Langmuir* **2006,** 22, (13), 5958-5962.
160. Salloum, D. S.; Schlenoff, J. B., Protein adsorption modalities of polyelectrolyte multilayers. *Biomacromolecules* **2004,** 5, (3), 1089-1096.
161. Alexeev, A.; Verberg, R.; Balazs, A. C., Patterned surfaces segregate compliant microcapsules. *Langmuir* **2007,** 23, (3), 983-987.
162. Wang, T. C.; Rubner, M. F.; Cohen, R. E., Polyelectrolyte multilayer nanoreactors for preparing silver nanoparticle composites: Controlling metal concentration and nanoparticle size. *Langmuir* **2002,** 18, (8), 3370-3375.
163. Wang, T. C.; Chen, B.; Rubner, M. F.; Cohen, R. E., Selective electroless nickel plating on polyelectrolyte multilayer platforms. *Langmuir* **2001,** 17, (21), 6610-6615.
164. Joly, S.; Kane, R.; Radzilowski, L.; Wang, T.; Wu, A.; Cohen, R. E.; Thomas, E. L.; Rubner, M. F., Multilayer nanoreactors for metallic and semiconducting particles. *Langmuir* **2000,** 16, (3), 1354-1359.